A VLA STUDY OF 24 SHORT TERM RADIO VARIABLES

By

Bernard J. Pöller

B. Sc. (Physics) Dalhousie University, 1995

A THESIS SUBMITTED IN PARTIAL FULFILLMENT OF

THE REQUIREMENTS FOR THE DEGREE OF

MASTER OF SCIENCE

in

THE FACULTY OF GRADUATE STUDIES

DEPARTMENT OF PHYSICS AND ASTRONOMY

We accept this thesis as conforming

to the required standard

THE UNIVERSITY OF BRITISH COLUMBIA

1997

Department of Physics and Astronomy
The University of British Columbia
6224 Agricultural Road
Vancouver B.C. Canada
V6T 1Z1

Date: Oct 7/97

Abstract

Flux density variability information, on a time scale of days, has been extracted [2] for a number of radio sources, from the GB6 [1] catalog data. Twenty four sources, including some with *NVSS* counterparts, exhibiting significant short term variability, and with no current identification in either the *NED* or *SIMBAD* external databases, were selected for a Very Large Array B configuration study. VLA snapshots were taken at two epochs, separated by approximately a month, at two frequency bands, to elucidate variations in flux density, source structure and spectral index. The imaged sample of twenty four sources include well resolved sources with one-sided or two-sided structure, partially resolved sources, and some unresolved sources. Of the partially resolved and unresolved sources, a number are confirmed as being variable in flux density and spectral index. In particular, the partially resolved sources J1700+685, J2115+367, and J2145+187 exhibit short term structural variation, suggesting these sources are galactic. The unresolved sources J0251+562, J0502+346, and J0611+723 exhibit significant flux variability. *APS* results indicate that the unresolved source J0856+717 is stellar.

Table of Contents

List of Tables

List of Figures

Acknowledgements

First and foremost I would like to thank my supervisor, Dr. Philip C. Gregory (UBC) who graciously provided support, encouragement, and guidance throughout this project, yet allowed me freedom in pursuing my masters thesis research. His years of research and many discoveries in the fields of radio and X-ray astronomy have been an inspiration, and his work on radio variability, particularly in the GB6 catalog, is the foundation for my research. I am greatly indebted to Dr. Gregory and this thesis would not have been possible without his help.

I wish to thank Dr. Pat Murphy at NRAO for his invaluable assistance in installing the *AIPS* software package on our new LINUX system. Without his expertise, the research would have come to a screeching halt, and there would have been no end to my computer frustrations.

Finally, I would like to acknowledge all the faculty, staff, and students in the Physics and Astronomy Department at the University of British Columbia who supported me, and made my time at UBC memorable.

Chapter 1

Introduction to Radio Variability

The study of variability in observed phenomena is a common focus of research in many fields of science. As humans, we are often fascinated by change, and endeavouring to understand it has led to numerous interesting discoveries.

From a cosmological point of view, we know the universe and everything in it is continually evolving, yet on time scales of a lifetime the night sky appears, to first order, static. Significant astrophysical variability, on short time scales, is relatively rare as it usually implies, in the context of typical cosmic distances, violent, high energy processes with enormous power outputs, confined to small volumes of space. These dynamic events give us great astronomical insight, often eluding simplistic conventional wisdom and thereby challenging the formulation of new theories, in some of the most fundamental and interesting branches of physics.

There are many examples of optical variability such as pulsating Cepheids used as cosmological distance indicators, to punctuated, cataclysmic events like supernovae, during which a star may become billions of times more luminous [19]. Variability at radio wavelengths is a relatively new field of study, and in this thesis, after an introduction, we begin by discussing mechanisms of variability in chapter 2. Long term GB6 variability is looked at in chapter 3 and in chapter 4 a sample of short term GB6 variables is presented, the short term variable selection process is outlined, and a summary of GB6 and external database information for the selected sources is given. A brief overview of VLA imaging is included in chapter 5 and the results of the VLA study are presented and discussed in chapter 6.

1.1 The Green Bank 6 Centimeter Survey

Until recently, variability at radio wavelengths on a statistical, or survey basis had not been given the attention it deserved, the focus having been close monitoring of known radio variables. Little was known about the radio source population as a whole in terms of the fraction of sources variable at some level or on some time scale.

A group of researchers from the University of British Columbia (UBC) and the National Radio Astronomy Observatory (NRAO) undertook a project, in the late 1980's, to survey the sky of the northern hemisphere for radio sources, particularly for variable sources. This project was completed, using the former 91 meter radio telescope in Green Bank, West Virginia, by surveying the sky between declinations 0 and 75 degrees at a wavelength of 6 centimeters (4.85 GHz), during November 1986 and October 1987.

The radio source data available from this project fall into three main categories of astronomical interest. Radio images of the northern sky were constructed from the 1986 and 1987 epoch data. These images were combined and analyzed to yield position and average flux density information for 75,162 discrete sources with flux densities $F \geq 18$ mJy and angular diameters $\phi \leq 10.5$ arcminutes [1]. The published Green Bank 6 centimeter survey (GB6) includes source data, as well as specific catalog production information [1]. Based on the individual epoch maps, flux densities for both epochs were determined for sources stronger than ≈ 25 mJy [1], yielding long term variability information, on a time scale of a year.

To ensure sufficient sampling at lower declinations, the continuous scanning technique, as outlined in [2], over sampled higher declination sources. During each month long observing epoch, multiple flux density measurements, for all sources in the GB6 catalog, were taken (typically six measurements per epoch) and therefore allow derivation of short term variability information on time scales from days to weeks. Extraction of short term variability information from the GB6 data is still in progress, with only a fraction of this information currently available.

1.2 The Short Term Radio Variable VLA Study

With the available GB6 variability data, the next natural step was a more detailed follow up study of the more extreme short term variables at a higher resolution. The author undertook the project of selecting 24 suitable short term variables, and imaging these sources at two frequency bands and at two epochs with the Very Large Array (VLA). With the GB6 short term variability information available at the project inception, sources exhibiting significant flux density variation and with no known identifications, were chosen. The selection process and the database resources used are discussed in more detail in section 4.1 and section 4.2. The goal of the project was to gain more information about these short term variables from accurate flux density measurements and high resolution intensity maps, perhaps elucidating the type of object involved. It was hoped that due to the extreme variability, some of the short term variables may be galactic relativistically beamed jet sources or other galactic sources of interest. If the high resolution VLA images show evidence of significant structural change over the two epochs, this would strongly suggest a galactic object. By imaging at two frequencies we were able to obtain spectral index data to compliment the two epoch flux density measurements from which we derived month time scale variability information. Specific VLA imaging parameter information may be found in section 5.2.

1.3 Measures of Variability

Before studying variability one must first be able to quantify variation, and in the context of this thesis, we are primarily concerned with measuring variations in flux density. The flux density of a variable object may be considered to be continuously changing, with some amplitude, for a superposition of time scales. Both the amplitude and time scales of variation may be functions of time themselves. Intrinsically, measurements are limited by number, frequency, and duration of observation, and therefore the data are merely a statistical sample valid only for a specific range of time scales. Analysis of variability is complicated further by measurement uncertainties inherent in all experiments. There are a number of ways to quantify observed variability, each with it's own merit.

In the simplest case two measurements, F_1 and F_2, with associated uncertainties, σ_1 and σ_2, are taken a time, Δt, apart. If we define the flux density change ΔF as $|F_1 - F_2|$ then we can compute a variability index, V, given by

$$V = \frac{\Delta F}{F_1 + F_2} \tag{1.1}$$

or in terms of a weighted average value and expressed as a percentage

$$V_{\%} = \frac{\Delta F}{\bar{F}_w} \times 100 \tag{1.2}$$

where

$$\bar{F}_w = \left(\frac{F_1}{\sigma_1} + \frac{F_2}{\sigma_2}\right) / \left(\frac{1}{\sigma_1} + \frac{1}{\sigma_2}\right). \tag{1.3}$$

Both equation 1.1 and 1.2 are good measures of the level of variation, but do not directly incorporate error estimates. A sigma confidence level, V_σ, for a detected variation level may be defined,

$$V_\sigma = \frac{\Delta F}{\sigma} \tag{1.4}$$

where σ is the root of the quadrature sum of the individual measurement uncertainties. Ideally, a number of data pairs over the interval Δt are taken, and the computed variability measurements are averaged. Otherwise, one data pair must be assumed to be characteristic of the time scale Δt, which, strictly speaking, is only statistically true.

If there are N flux density measurements, F_i, and uncertainties, σ_i, taken at intervals Δt_i, with Δt being characteristic, then we can define a Q value to the data set, quantifying both degree of variability and confidence level, that is more statistically valid. An observed goodness of fit, χ^2_{obs}, of the data set to a default constant model is given by the expression

$$\chi^2_{obs} = \sum_{i=1}^{N} \left[\frac{F_i - \bar{F}_w}{\sigma_i} \right]^2 \tag{1.5}$$

where $\bar{F}_w$ is an obvious extension of equation 1.3 to N measurements. The data set Q value is then the probability of a χ^2 larger than χ^2_{obs} occurring by chance if the constant model assumed is correct, and is given by an incomplete gamma function with $\nu = N-1$ degrees of freedom. For convenience, the negative logarithm of the Q value is usually quoted, with a greater $-\log Q$ value corresponding to increased variability confidence. The $-\log Q$ cutoff for considering a source to be significantly variable is somewhat arbitrary, but is typically 2 or 3. The Q value is dependent on number and uncertainties of the parameter measurements and statistically valid for a range of Δt, determined by the Δt_i population. For brevity $-\log Q$ is defined as $\hat{Q}$, and hereafter used interchangeably.

Chapter 2

Radio Variability Mechanisms

To design the VLA study, and later interpret the results, it is important to understand short term variability mechanisms to which the project is sensitive. The vast majority of GB6 sources is undoubtedly extragalactic, and the most likely mechanisms for short term variability include highly beamed AGN, or extragalactic sources made to appear variable by interstellar scintillation. By selecting only short term highly variable sources we hoped to increase the chance of detecting galactic objects, perhaps galactic jet sources or radio stars. High resolution images of a wide variety of radio sources, both galactic and extragalactic, can be found in reference [16].

2.1 Active Galactic Nuclei

Active galactic nuclei (AGN) are, as their name suggests, associated with the central region of distant galaxies, characterized by relatively high luminosities emanating from a tiny galactic volume. The primary feature of current models for these powerful objects is a supermassive black hole at the center of a galaxy, with the gravitational potential of the black hole being the main power source. Interstellar material is drawn towards the black hole and emits UV-rays, soft X-rays, and eventually hard X-rays as the plasma forms a rapidly rotating accretion disk around the black hole. The large scale motion of plasma induces powerful magnetic fields which facilitate the ejection of synchrotron emitting plasma, in highly collimated jets, at relativistic speeds, along the poles of the rotation axis. The high energy and relativistic physics involved make AGN of broad scientific interest and detailed theoretical models of extragalactic beams and jets, as presented in [13], have been formulated. Since the AGN model is axisymmetric, the appearance, and current classification of these objects is dominated by orientation [17].

2.1.1 Unification Schemes

Attempts are currently being made to classify and understand AGN based on more appropriate physical characteristics instead of parameters dependent on aspect angle [17]. Previously, radio loud AGN, those with a radio to optical flux ratio greater than ten, were classified based on radio and optical luminosity, width of emission lines, radio spectral indices, and polarization level.

It has now been accepted that most radio loud AGN belong to two main classes, based on Fanaroff-Riley luminosity levels and differences in appearance are due primarily to beam orientation with respect to the observer [17]. In particular, it is believed that FR II galaxies, steep spectrum radio quasars, and flat spectrum radio quasars constitute one morphological type while FR I galaxies and BL Lacertae objects form another.

In this combined scheme, AGN may be interpreted as a continuum with radio galaxies having beam axes nearly perpendicular to the line of sight and blazars being viewed almost directly down the beam axes. Clearly there is merit in this unification scheme, however it is undoubtedly an oversimplification since some AGN characteristics can not be adequately incorporated. Furthermore, AGN classification is complicated by different levels of circumnuclear obscuration due to material near the galactic core and observed redshifts.

2.1.2 Relativistic Effects

The rapid flux variations, high polarization and luminosity levels observed in some radio loud AGN are believed to be due to relativistic beaming [17]. Special relativity

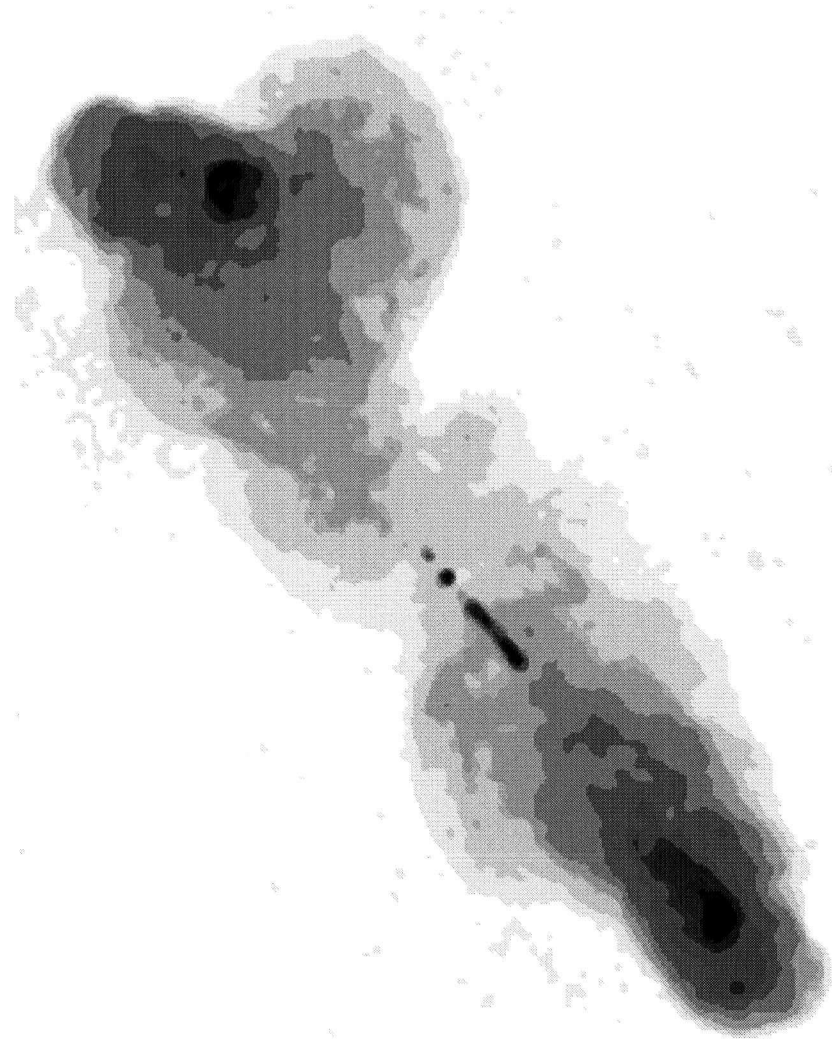

Figure 2.1: VLA 20 centimeter image of FR II radio galaxy 3C219. The radio galaxy is at a red shift of $z = 0.1745$, shown here with a resolution of 1.4 arcseconds. Large radio lobes extending hundreds of kiloparsecs, with hot spots, are seen in this image, as well as a two-sided jet and a bright core. Adapted from [18]

transformations of time and frequency from the rest to observers frame are given by

$$\Delta t = \frac{\Delta t'}{\delta} \tag{2.1}$$

$$\nu = \delta \nu' \tag{2.2}$$

where the primed variable is in the rest frame of the jet, and the Doppler factor, δ, is

$$\delta = [\gamma(1 - \beta \cos\theta)]^{-1} \tag{2.3}$$

with β the bulk velocity normalized by the speed of light, θ the angle between the velocity vector and the line of sight, and γ being the Lorentz factor

$$\gamma = (1 - \beta^2)^{-1/2}. \tag{2.4}$$

A direct result of equations 2.1 and 2.2 is a decrease in the variability time scale and a blue shift of the flux as seen in the observers frame. In extreme cases the transverse velocity of the relativistic motion may appear to be superluminal. An in depth discussion of observations and theory of superluminal sources may be found in reference [14]. The relativistic transformation of angles implies forward beaming of an intrinsically isotropic radiator. The combined effect of relativistic beaming and the doppler frequency band compression is amplification of the intrinsic broad band rest flux density

$$F = \delta^4 F' \tag{2.5}$$

and flux variation

$$\frac{\Delta F}{\Delta t} = \delta^5 \frac{\Delta F'}{\Delta t}. \tag{2.6}$$

Both equation 2.5 and 2.6 are strongly dependent on the Doppler factor (equation 2.3), plotted in figure 2.2 for various velocities and observation angles. This strong dependence of equation 2.6 means that AGN may appear to be significantly variable, in the core, on short time scales. Equation 2.5 can dramatically increase the core to extended emission flux ratio as well as enhancing the flux from the approaching jet while quenching the receding jet. Clearly some AGN may appear as either one-sided or with no extended structure at all.

2.2 Galactic Jet Sources

In our galaxy there exists smaller scale counterparts of the active galactic nuclei. These recently discovered galactic relativistic jet sources exhibit a wide range of characteristics, as do their extragalactic analogs: from superluminal jet sources like GRS 1915+105 and GRO J1655-40, and relativistic jet sources SS433, GRS 1758-258, Cyg X-3 and 1E1740-2942, to the flat spectrum X-ray binaries: Cyg X-1, Cyg X-2, Sco X-1, and Cir X-1, also proposed as jet sources.

Galactic jet sources are associated with binary systems containing a black hole, or neutron star, often with a transient hard X-ray and γ-ray signature. Surrounding the compact object is an accretion disk with characteristics temperatures of approximately 10 keV [3], and a pair of highly collimated, relativistic particle jets, extending light years from the central objects, emitting synchrotron radiation. The particle jet usually takes the form of episodic ejections of large clouds of plasma (plasmons). A schematic diagram of the relativistic jet source SS433 is shown in figure 2.3.

GRS 1915+105, almost certainly a black hole [3], and discovered in 1992 with the GRANAT satellite, exemplifies the physical behaviour of relativistic jet sources. Located towards the center of the galaxy, with galactic coordinates $l = 45.4°$ and $b = -0.3°$, it is estimated to be approximately 12.5 ± 1.5 *kpc* away, and has been identified with an infrared counterpart, although no optical counterpart has yet been observed. GRS 1915+105 has been extensively monitored with the VLA at various frequencies, and studies have yielded parameter measurements for a kinematic model.

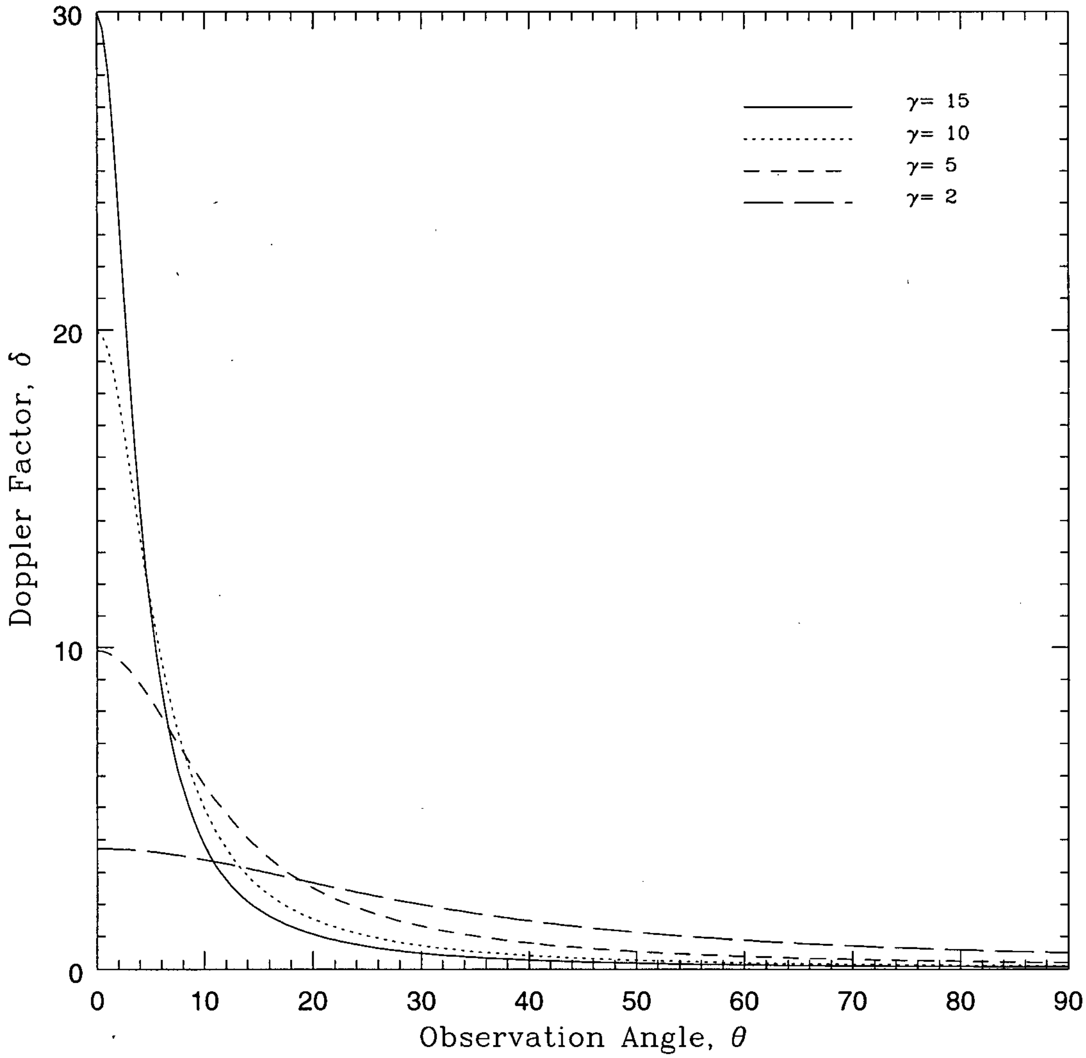

Figure 2.2: Doppler factor for different β and θ

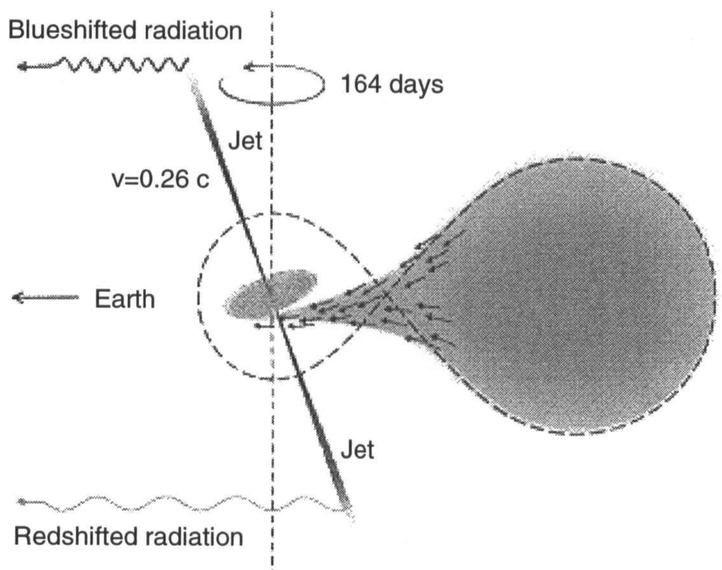

Figure 2.3: Schematic representation of galactic relativistic jet source SS433. Adapted from [20].

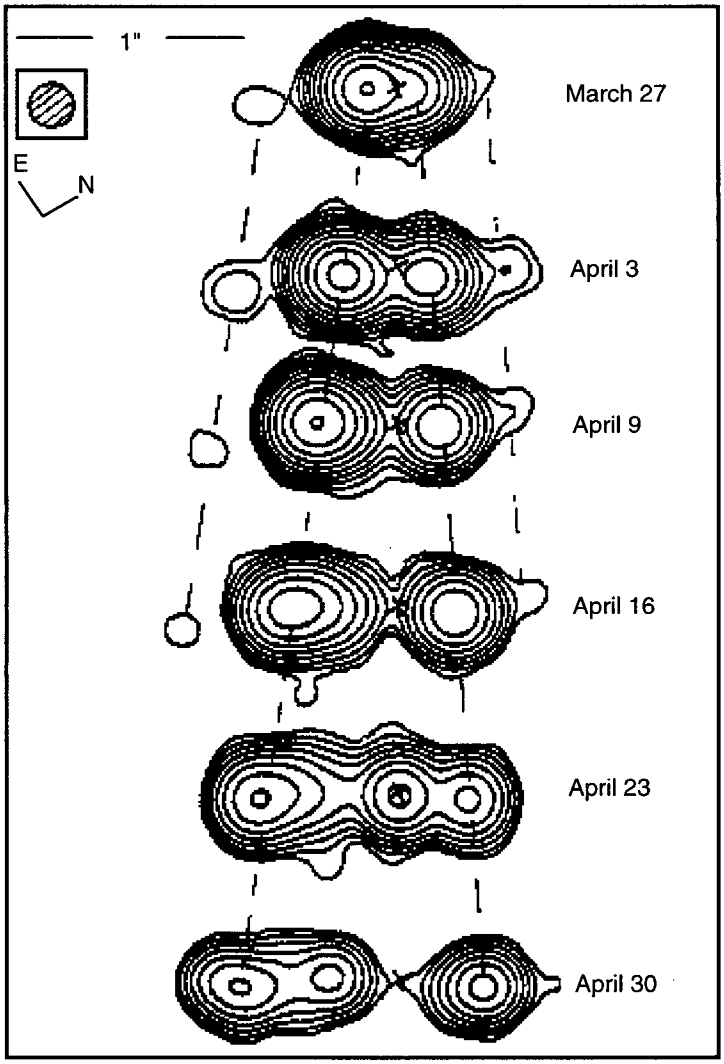

Figure 2.4: Radio maps of microquasar GRS1915+105 imaged with the VLA at 3.5 centimeters (from [3]). Contours are 1, 2, 4, 8, 32, 64, 128, 256,and 512 times 0.2 mJy/beam for all epochs except for March 27 for which the contour unit is 0.6 mJy/beam. A pair of plasmons can be seen moving away from the stationary core, marked by a cross.

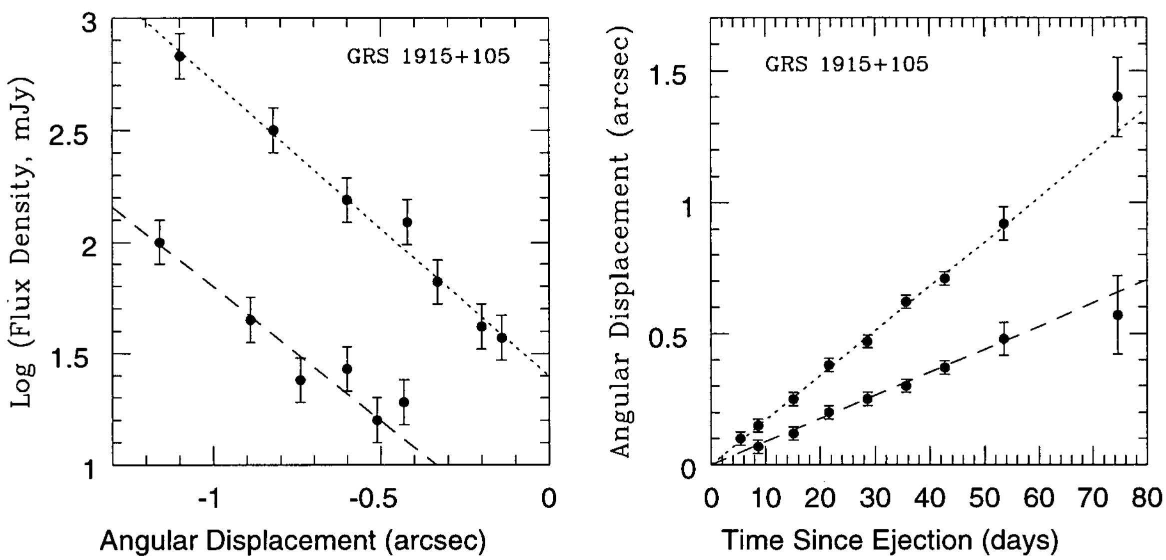

Figure 2.5: Angular displacement as a function of time after ejection, and 3.5 centimeter flux density as a function of angular displacement, for observed plasmons of microquasar GRS 1915+105. Top and bottom lines in both graphs are regression fits for approaching and receding jets respectively. Adapted from [3].

VLA images (figure 2.4) clearly show bright radio condensations, or plasmons, emerging from the central compact object. The shown plasmons are believed to have been ejected on March 19, 1994 at 20±5 universal time. From the observed motion of 17.6±0.4 mas/day and 9.0 ± 0.1 mas/day, corresponding to $1.25c$ and $0.65c$, for the approaching and receding jet respectively, true ejection velocity has been determined as $0.92c$, with the jet axis at 70° to the line of sight [3]. This relativistic plasma velocity yields a doppler factor of $\delta = 0.56$ for the approaching jet (eqn 2.3). As the condensations move away from the core, they are observed to fade, but the approaching and receding flux ratio remains constant at 8 ± 1, consistent with relativistic beaming [3].

2.3 Radio Stars

All radio stars are intrinsically variable, typically on a time scale of hours, and may be loosely classified as a flare star, radio nova, pulsar, X-ray star, or belonging to a close binary system. Although pulsars can be extremely variable with clocklike periodicity, the pulse time scales are usually less than a second and therefore too short for consideration here. X-ray stars, correlated with galactic jet sources, are discussed in section 2.2.

Stellar flares are associated with plasma being ejected from active starspot regions. These flares usually produce coincident optical and radio outbursts, but to be detectable, the radio emissions must be orders of magnitude greater than those associated with solar flaring. For this reason, flare stars commonly belong to binary systems, where the companion may act as a catalyst for more frequent and powerful flaring activity. The mechanism of the radio emission is not well understood, but typically the radiation occurs at meter wavelengths, varying on a time scale of hours, with a non-thermal spectrum, or at shorter centimeter wavelengths, with slightly longer time scales, and being partially circularly polarized [12a].

Radio novae, as their optical counterparts, are quasi-periodic explosions on the surface of a star which rapidly accelerates an ionized plasma shockwave. This exploding shell of gas typically produces thermal radiation with a changing spectral index. Prototypical examples of a radio novae include Nova Delphini and Nova Serpentis [12a]. It is worthy of note that although most radio stars have angular diameters a lot less than an arcsecond, this is not necessarily the case for radio novae.

Radio stars belong predominantly to binary systems [15], since the interaction of a stellar pair can induce both flaring and nova activity. A particularly interesting class of binary systems, known as a symbiotic pair, consist of a red giant and a small companion, such as a white dwarf, in proximity to each other. The gravitational interaction of the pair may cause mass transfer from the giant. This spillover of gas results in the accretion of plasma on the surface of the compact companion and the formation of complex shockwave patterns. The emitted radio radiation is often thermal, with extreme variability. The radio emission may be quasi-periodic, and may increase quiescent flux density by an order of magnitude on a time scale of hours.

2.4 Interstellar Scintillation

An extrinsic mechanism for flux density variations in radio sources [6] is interstellar scintillation (ISS). Intrinsic mechanisms of variability in compact sources require extreme brightness temperatures or doppler factors. ISS is a result of both large and small scale irregularities or turbulence in the interstellar plasma, and effects all extragalactic sources at some level. Two phenomenological types of ISS occur: refractive (RISS) and defractive (DISS); however for typical compact extragalactic radio sources at centimeter wavelengths, RISS predominates [6]. Except in a strong scintillation regime, RISS is well modeled by the Born approximation of scattering theory.

Two important parameters characterizing RISS are scintillation index (m), the mean normalized rms flux amplitude, and a scattering time scale (τ), both of which are strong functions of source angular diameter (θ). Significant RISS occurs only if the source diameter is of the order, or smaller than the scattering diameter (θ_{ds}). Apparent source position shifts, on the order of the scattering diameter, may be a manifestation of RISS. The effect of RISS can be simply modeled [6] by an instantaneous phase shift, equal to the extended medium path length, occurring at a distance, L, from the observer. The extended medium consists primarily of two components, a wide galactic disk, and an enhancement galactic plane component. The galactic plane component varies spatially with galactic latitude and with proximity to the galactic center. For absolute galactic latitudes greater than five degrees, this component can be ignored.

For an extragalactic point source, at absolute galactic latitude b, the scintillation index and time scale can be approximated by:

$$m_R \approx 0.5$$

$$\tau_R(\text{days}) \approx \frac{L\theta_{ds}}{1.7v} \tag{2.7}$$

where:

$$L(\text{pc}) \approx 500 \csc b$$

$$\theta \approx 8\lambda^2(\csc b)^{1/2}.$$

Extended extragalactic source RISS is modeled by:

$$m_E \approx m_R \frac{\theta_{ds}}{(\theta_{ds}^2 + \theta^2)^{1/2}}$$

$$\tau_E(\text{days}) \approx \frac{L(\theta_{ds}^2 + \theta^2)^{1/2}}{1.7v} \tag{2.8}$$

with all angles measured in milliarcseconds, λ in meters, and v, the velocity of the observer relative to the extended medium, in kilometers per second. The scintillation index and time scale are plotted in figure 2.6 for characteristic parameter values.

The amplitude of flux variation increases with wavelength, but for most flat-spectrum, compact source models, the effective source diameter also increases with wavelength, and the scintillation index will eventually flatten out. As extended source diameters increase, spatially smoothed scintillation patterns yield smaller indices.

The scintillation time scale for small wavelengths is effectively constant, but asymptotically approach the point source limit at longer wavelengths, as source diameters increase. In general, RISS is a more successful explanation of small amplitude, short time scale variations, as high amplitude, long time scale variations are more likely intrinsic

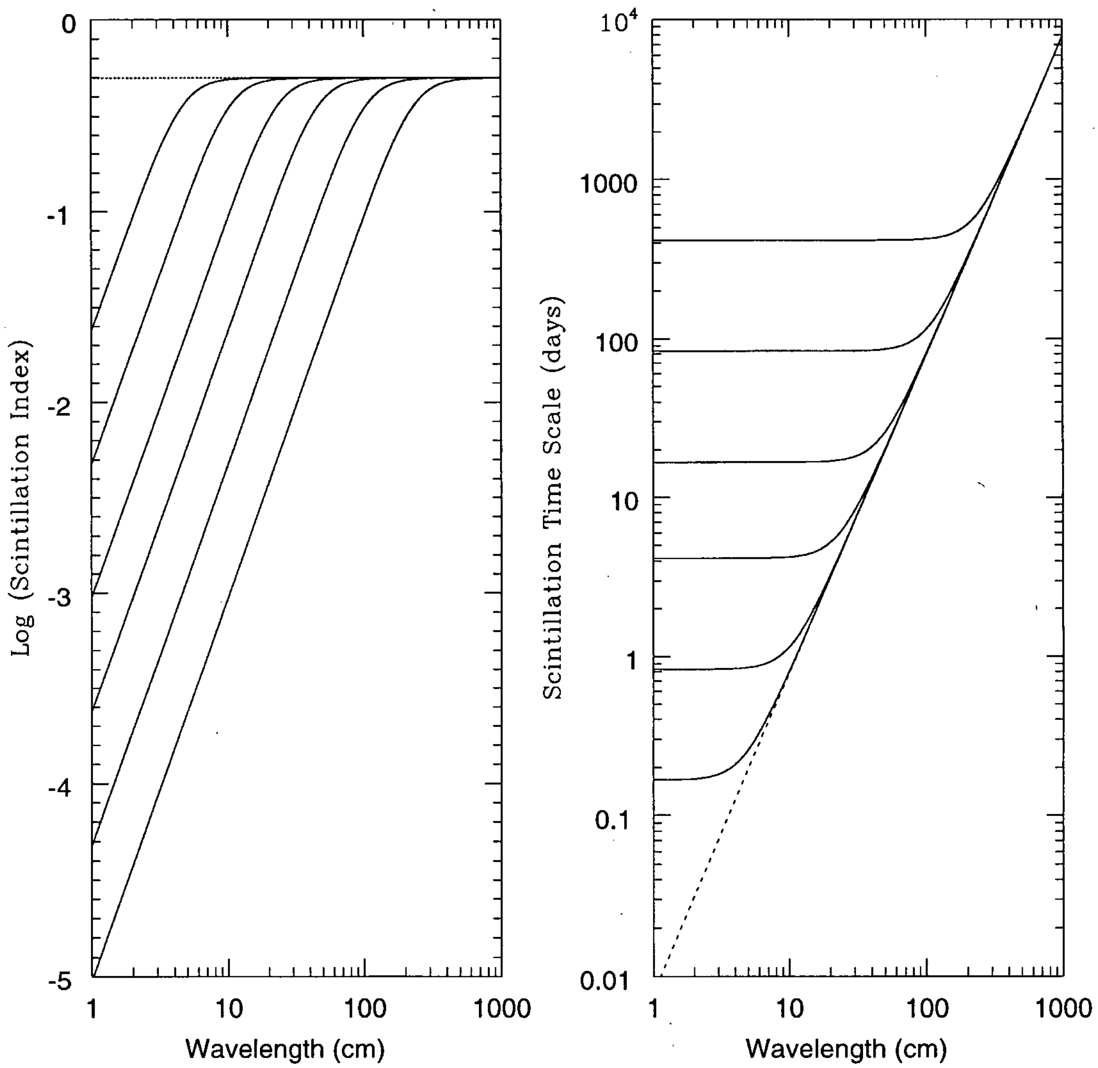

Figure 2.6: Scintillation index and time scale plotted versus wavelength and source diameter. Characteristic values of galactic latitude ($|b| = 45°$) and velocity ($v = 50$ km/s), representing the earths orbital motion and peculiar velocity of the sun. Source diameters are 50,10,2,0.5,0.1,and 0.02 mas from right to left and from top to bottom on index and time scale plot respectively.

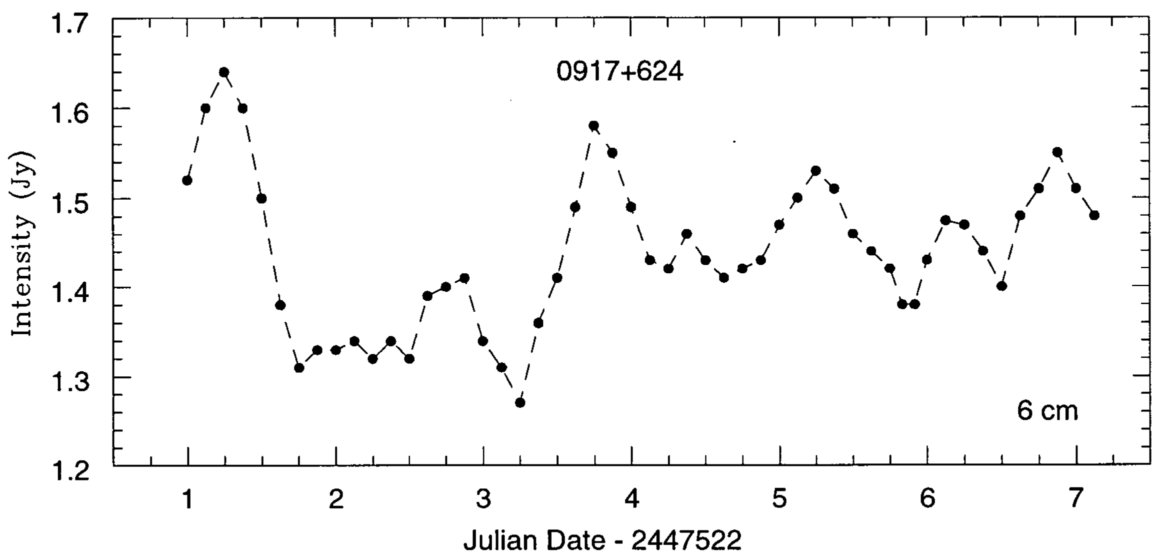

Figure 2.7: Flux density of source 0917+624 at 6 centimeter wavelength as a function of observation date. RISS is well established as the cause of the intensity variations. Modified from [6].

to the source [6]. In any compact extragalactic radio source, however, RISS is always a component and must be considered as an explanation for observed flux density variations.

The intra-day radio variable 0917+624 has been studied over the last eight years at multiple wavelengths. This source exhibits rapid flux variations on a time scale of hours, with significant amplitudes (see figure 2.7). These flux variations are wavelength correlated, with no time delay [7], contrary to the wavelength dependent time delay predicted by intrinsic variation models. 0917+624 also exhibits random position variations on time scales comparable to the flux variations at centimeter wavelengths [7].

RISS is believed to be the mechanism of a variety of radio source variability [6], including the long term variations seen in pulsars. At centimeter wavelengths, RISS is the likely cause of flat-spectrum flux variations of a few percent [6].

Chapter 3

GB6 Long Term Variability

As an aside to the author's main research, aspects of population statistics for a recently generated GB6, greater than 2.5 sigma confidence, long term variability list, were studied. Here, long term variability is defined by a time scale of approximately a year. The variability confidence cutoff level, for scientific usefulness, is somewhat arbitrary, but achieving large number statistics must be balanced with introducing an increasing fraction of spurious variables. The long term variability list used is believed to represent a reasonable confidence limit, with the implicit understanding that inclusion of sources with confidence level of 2.5 sigma or greater implies that the variability of approximately 13.5% of the 6918 sources is the statistical artifact of parameter noise, with the probability of false variability increasing for smaller confidence levels.

3.1 Galactic Projection and Variability Index Dependence

The long term variable source positions have been plotted, in figure 3.1, in an Aitoff galactic projection, with GB6 survey boundaries as shown. With the exception of a noticeable cluster of sources, towards the local Cygnus arm in the galactic plane, the spatial distribution appears to be both isotropic and homogeneous, consistent with the extragalactic object hypothesis for the vast majority of GB6 sources.

The galactic latitude dependence of the observed long term variability index is graphed, in figure 3.2, along with a linear regression fit. The overall trend is a decrease in variability index at smaller absolute galactic latitudes, contrary to expected interstellar scintillation

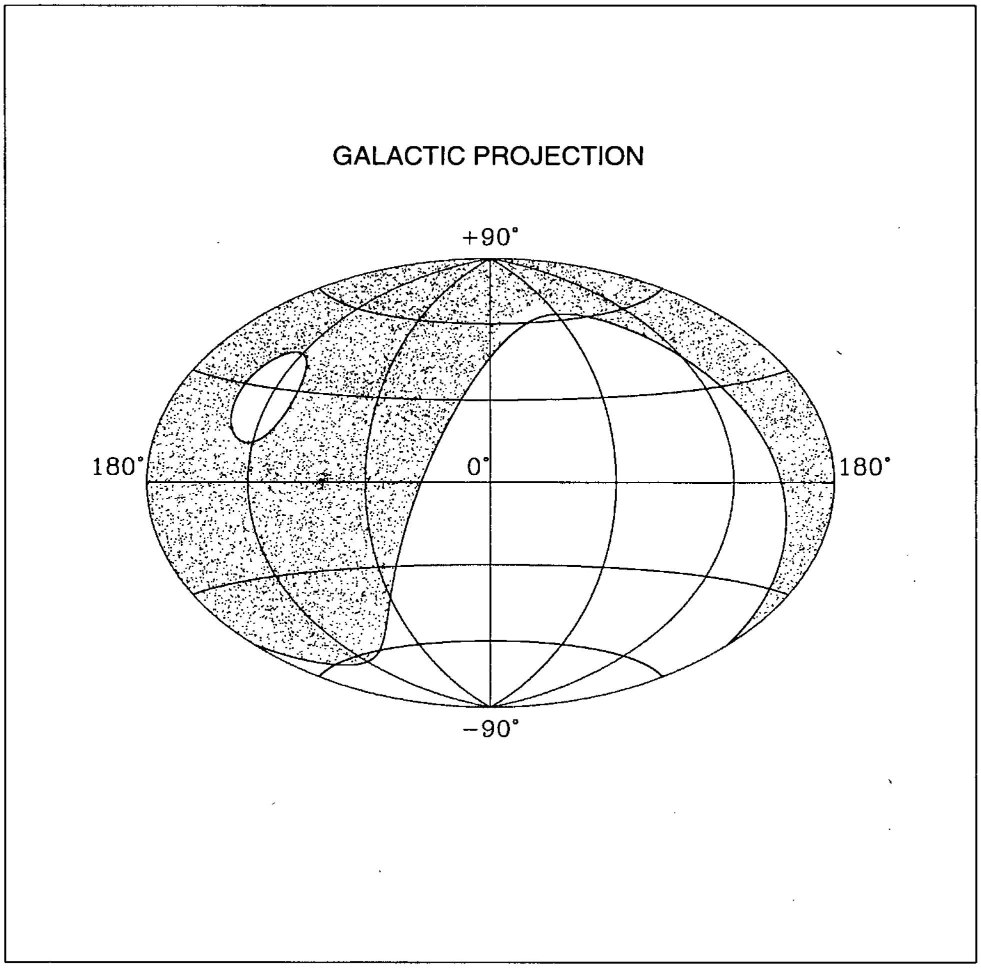

Figure 3.1: Aitoff galactic coordinate projection for sources (6918) on ≥ 2.5 sigma confidence GB6 long term variability list studied. GB6 survey boundaries are as shown.

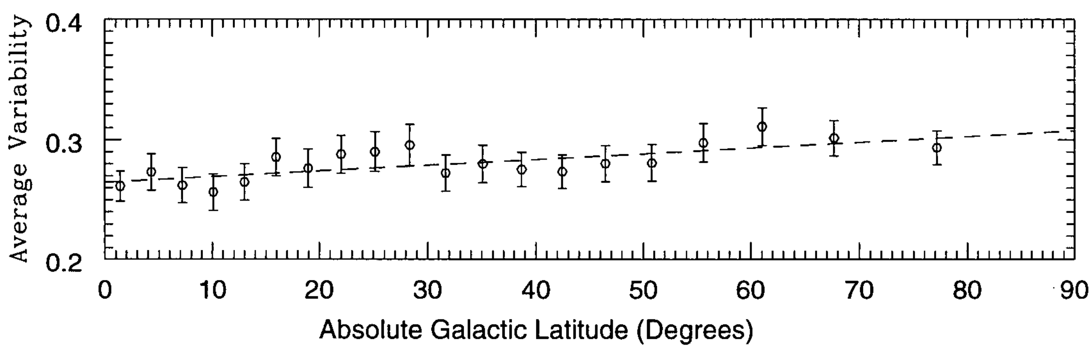

Figure 3.2: Variability index as a function of absolute galactic latitude, for sources on the ≥ 2.5 sigma confidence GB6 long term variable list. Linear regression is included.

(ISS) effects, most likely the result of a GB6 selection effect due to stricter detection thresholds for low galactic latitude sources. The exact dependence of ISS on galactic latitude is a complicated function, dependent primarily on interstellar material column densities, and observed variabilities are further complicated by limited sampling. The ripple, or oscillation apparent in figure 3.2, if interpreted as due to ISS, suggests approximate characteristic object angular sizes of 0.5 milliarcseconds, varying on time scales of several days, based on a scintillation index on the order of 10^{-2}, for GB6 observations.

3.2 Spectral Index Fraction Density

To extract spectral index information the NRAO VLA Sky Survey (NVSS) database was searched for positional matches, for all the GB6 long term variables and all sources in the GB6 catalog, within thirty arcseconds of the GB6 positions. The NVSS database, discussed in section 4.2.1, contains 20 centimeter flux density measurements, and matches were found for approximately 40% of the long term variables, with 2% being unmatched, and the remaining 58% lying in regions not currently covered by NVSS. The computed spectral indices (defined here by $F \propto \lambda^{\alpha}$) were binned and the discrete approximation to

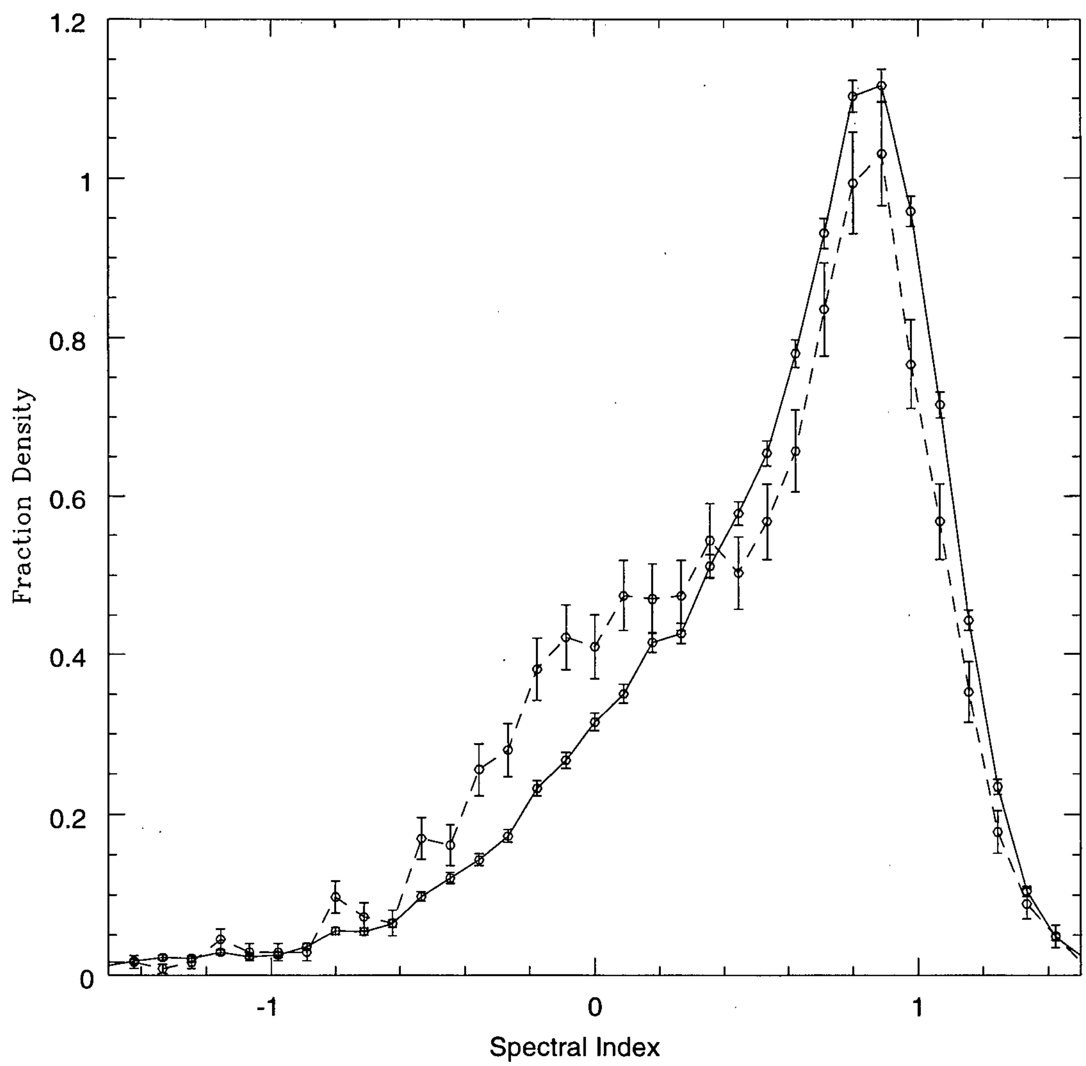

Figure 3.3: Fraction density distribution as a function of spectral index for GB6 long term variables (dotted line), and entire GB6 catalog (solid line), matched with NVSS database.

the fraction density, $\tilde{f}(\alpha)$, given by

$$\tilde{f}(\alpha_i) = \frac{n_i}{N\,\Delta\alpha} \tag{3.1}$$

where n_i is the number of sources in the i^{th} bin of width $\Delta\alpha$, and α_i being the central bin value, is plotted in figure 3.3 for NVSS matches of both the long term variables and the entire GB6 catalog. The total number of sources in each sample, N, normalizes the function so that the definite integral $\int_{-\infty}^{\infty} \tilde{f}(\alpha)\, d\alpha$ is unity.

Both fraction density distributions have a well defined steep spectrum peak near 0.8, consistent with that expected for an extragalactic population of normal radio-loud galaxies [12b]. However, the fraction density distribution of the long term variables has a distinct flat spectrum component which is significantly more pronounced than in the smoother distribution for the entire catalog.

To elucidate the origin of the long term variable flat spectrum shoulder, the centroid of the fraction density distribution is graphed in figure 3.4, as a function of GB6 flux, V_σ sigma confidence level (eqn. 1.4), and variability index, along with linear regression fits. Based on the dependence of the spectral index centroid in the graphs it is concluded that these flat spectrum objects have relatively high flux densities. Variability confidence levels are a function of flux density, and therefore confidence levels associated with these objects are also high. Since the long term variability list is confidence level limited, the sample of sources is biased towards these flat spectrum objects. There is no clear trend in spectral index as a function of variability index, with only slightly lower spectral indices for low variability index objects, that very likely the result of GB6 variability selection effects. The relatively high flux densities of these flat spectrum objects implies either relative proximity of these extragalactic sources, or more likely, that they are intrinsically brighter, perhaps due to extreme relativistic Doppler enhancement of the flux density. One may tentatively hypothesize that these objects are blazars, with only the extremely beamed flat spectrum cores visible.

It must be cautioned in the interpretation of the spectral index fraction density that there has been no attempt to remove unknown cosmological redshift, or forward beaming blueshift effects. As well, it is expected that there is a slight spectral index distribution skewing due to the fact that 6 centimeter flux density measurements were taken on a single dish, whereas the 20 centimeter data were taken on a spatially filtering interferometer, which is less sensitive to extended emission.

3.3 Variability Fraction Density

A variability fraction density can also be defined for either a sigma confidence level, V_σ, or a variability index, V, similar to the definition of spectral index fraction density given in equation 3.1. The fraction density of GB6 sources, as a function of sigma confidence level (eqn. 1.4), for $V_\sigma > 2.5$, can be determined directly from the long term variability list. The computed GB6 fraction density of the V_σ is plotted in figure 3.5 with a linear regression fit. For confidence levels between 7.5 and 2.5, the linear fit is reasonable and can be believably extended to lower sigma values, but for sigma values greater 7.5 the computed GB6 fraction density deviates from the linear fit and flattens out. The sigma confidence level is survey dependent, being directly related to characteristic flux density uncertainties, and the number of sources at a particular confidence level also depends on gaussian statistic probabilities. However the V_σ fraction density also reflects the intrinsic population variability. From graph 3.5 one can determine the number of GB6 sources having a particular long term variability confidence level.

As mentioned in the previous section, the GB6 survey sensitivity in detecting variability diminishes for lower variability indices. The GB6 selection factor, shown in figure 3.6, is a function of variability index and the sigma confidence level cutoff. The GB6

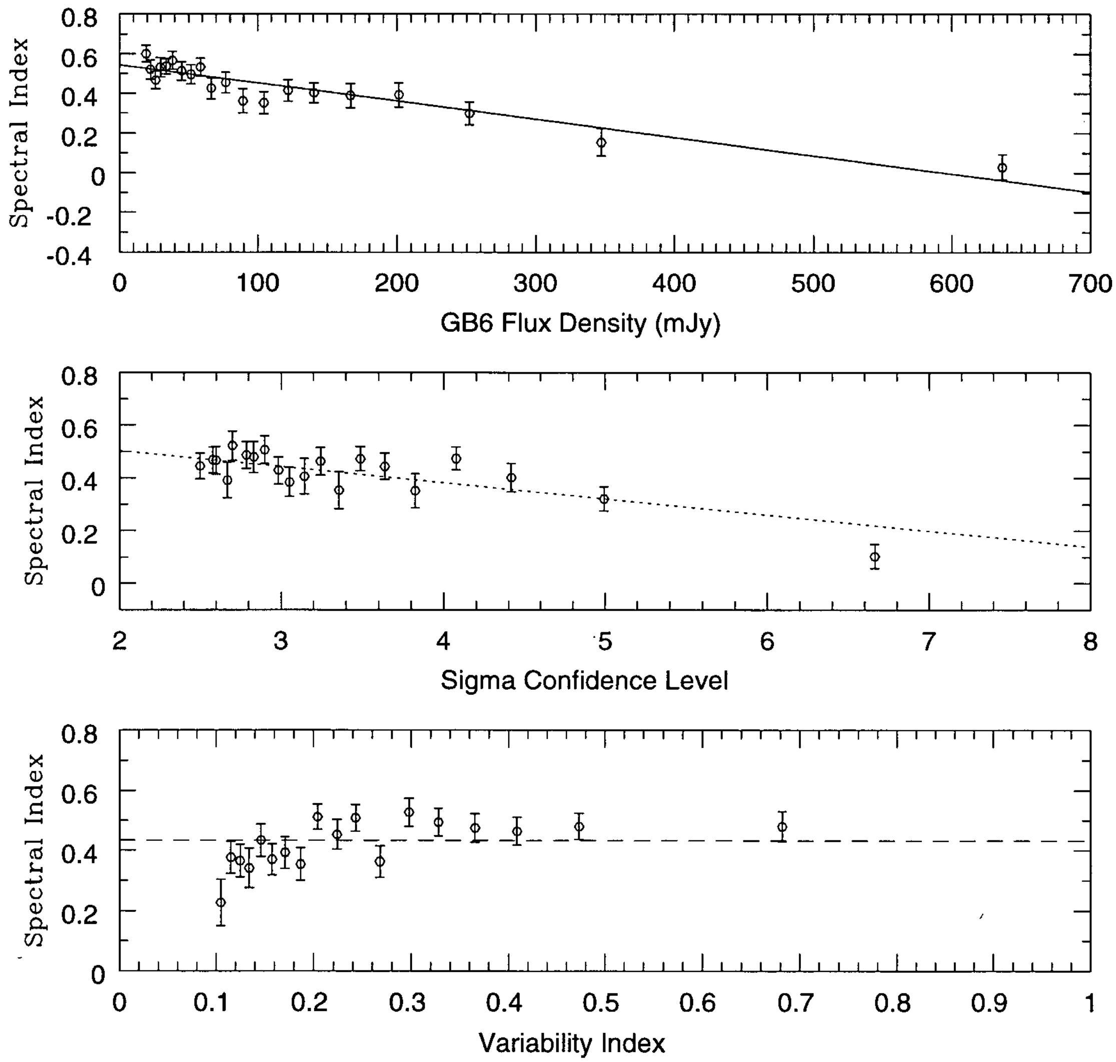

Figure 3.4: Spectral index centroid plotted versus GB6 flux density, sigma confidence level, and variability index, with associated linear regression fits.

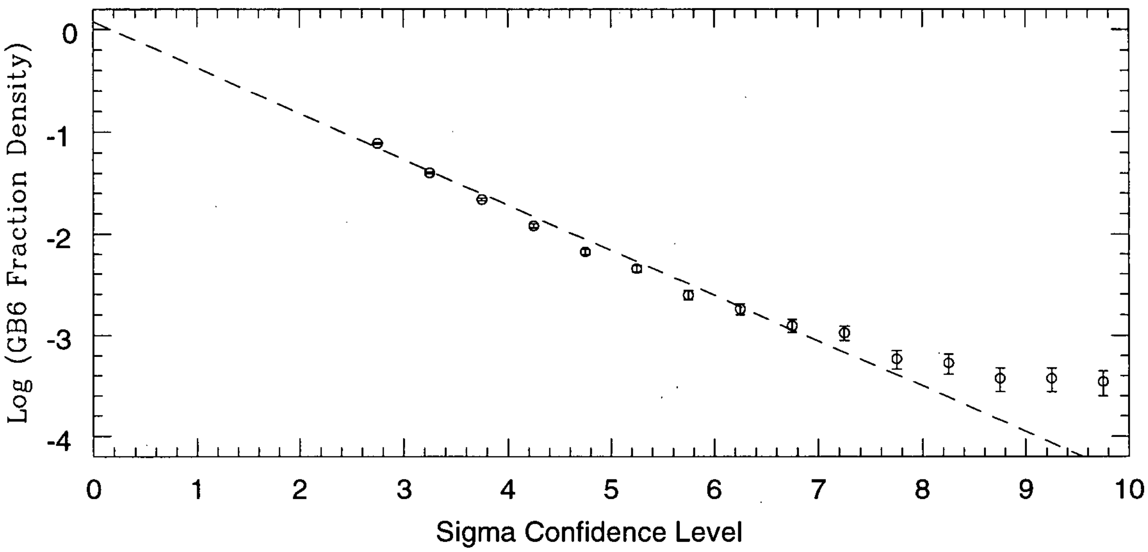

Figure 3.5: Logarithm of GB6 fraction density as a function of sigma confidence level, with linear regression fit.

selection factor may be interpreted as the fraction of GB6 sources that could in principle have been detected at a variability index, V, at a $\geq N\sigma$ confidence level. This was computed directly from the entire GB6 list of sources. The selection factor plotted in figure 3.6 is for a 2.5 sigma confidence level cutoff, but as sigma cutoff levels decrease, the selection factor approaches unity for lower variability indices.

The directly determined GB6 fraction density, as a function of variability index, V (eqn. 1.1), can be corrected for the GB6 variability index selection effect, by normalizing with the GB6 selection factor. The resultant corrected GB6 fraction density of variability index data (figure 3.7) becomes significantly uncertain at lower variability indices since, even at the 2.5 sigma confidence level cutoff, the GB6 selection factor approaches zero. A more accurate estimate of the GB6 fraction density at low variability indices was obtained by fitting a polynomial to the integrated cumulative GB6 fraction of sources with a variability index greater than a particular variability index. Since all GB6 sources

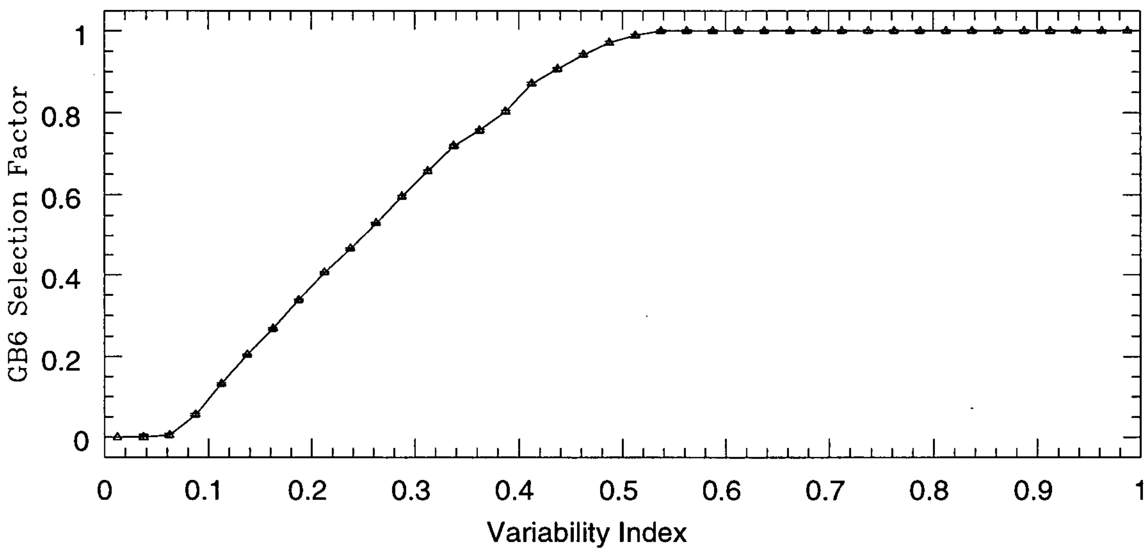

Figure 3.6: GB6 variability selection factor as a function of variability index for a 2.5 sigma confidence level cutoff.

must have a $V \geq 0$, the boundary condition that the cumulative GB6 fraction be unity at $V = 0$ is applied to the polynomial fit. A plot of the cumulative GB6 fraction data, with derived low variability index fit is given in figure 3.7 and the estimated low variability GB6 fraction density is included in figure 3.7.

The determined GB6 fraction density versus variability index, with the exception of flux density detection thresholds, is reasonably survey independent, and places constraints on any models of extragalactic radio source variability, in particular the unified beam model.

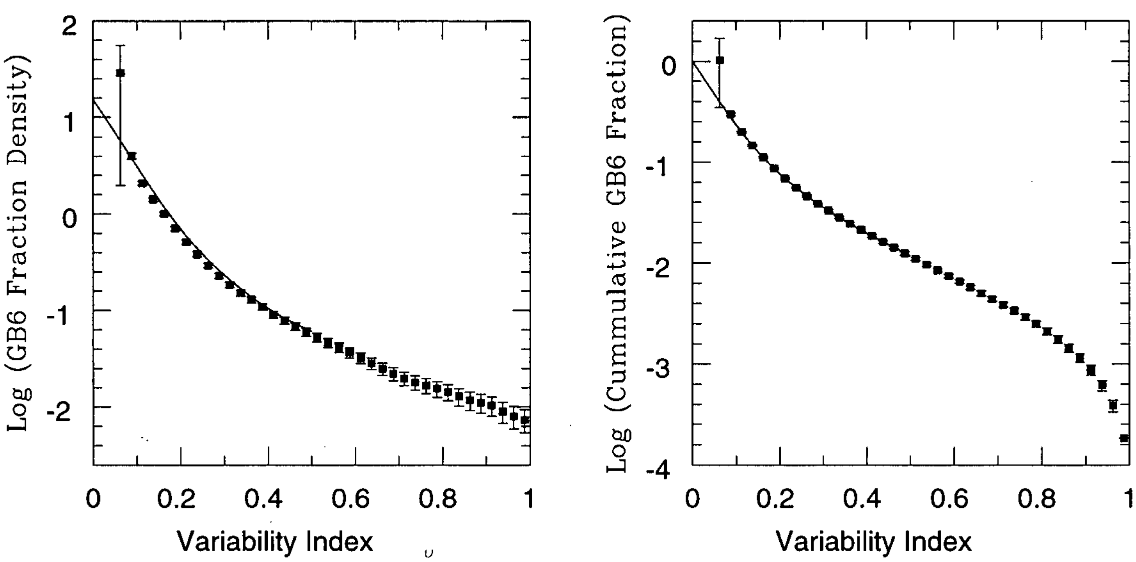

Figure 3.7: Logarithm plot of directly computed, and corrected model of, GB6 variability fraction density and cumulative GB6 variability fraction as a function of variability index.

Chapter 4

GB6 Short Term Variability

The selection process for the radio sources suitable for a short term variability VLA study began with a list of 499 GB6 sources for which daily flux density measurements had been previously extracted (short term variability list [STVL]), from the raw GB6 scan data, for another variability study [2]. Originally, the referenced researcher intended for the above list to include sources with long term variability at the 5 sigma level of confidence, or greater. Due to small flux density corrections, this is not strictly true, with the list now containing a number of sources down to the 4.5 sigma level, and can no longer be considered complete for the 5 sigma level.

4.1 $\hat{Q}$ Value Statistics and Selection

The negative logarithm of the Q value, discussed in section 1.3, and here after referred to as $\hat{Q}$, was computed from the daily flux density measurements. A galactic Aitoff projection plot of the positions for all sources on the short term variability list is shown in figure 4.1, and sources with a $\hat{Q}$ value greater than either 2 or 3, during both 1986 and 1987 epochs are highlighted. From the galactic projection there is no evidence for galactic concentration in the short term variability list as a whole, and only slight evidence for sources exhibiting strong short term variability.

The normalized density $\tilde{\rho}(\hat{Q})$, defined as $\frac{\rho(\hat{Q})}{\rho_o}$, where $\rho(\hat{Q})$ is the number of sources per unit $\hat{Q}$ at a particular $\hat{Q}$ value, and ρ_o is the expected value of $\rho(\hat{Q})$ assuming a uniform number distribution, is plotted in figure 4.2 for both epochs. The overall trend

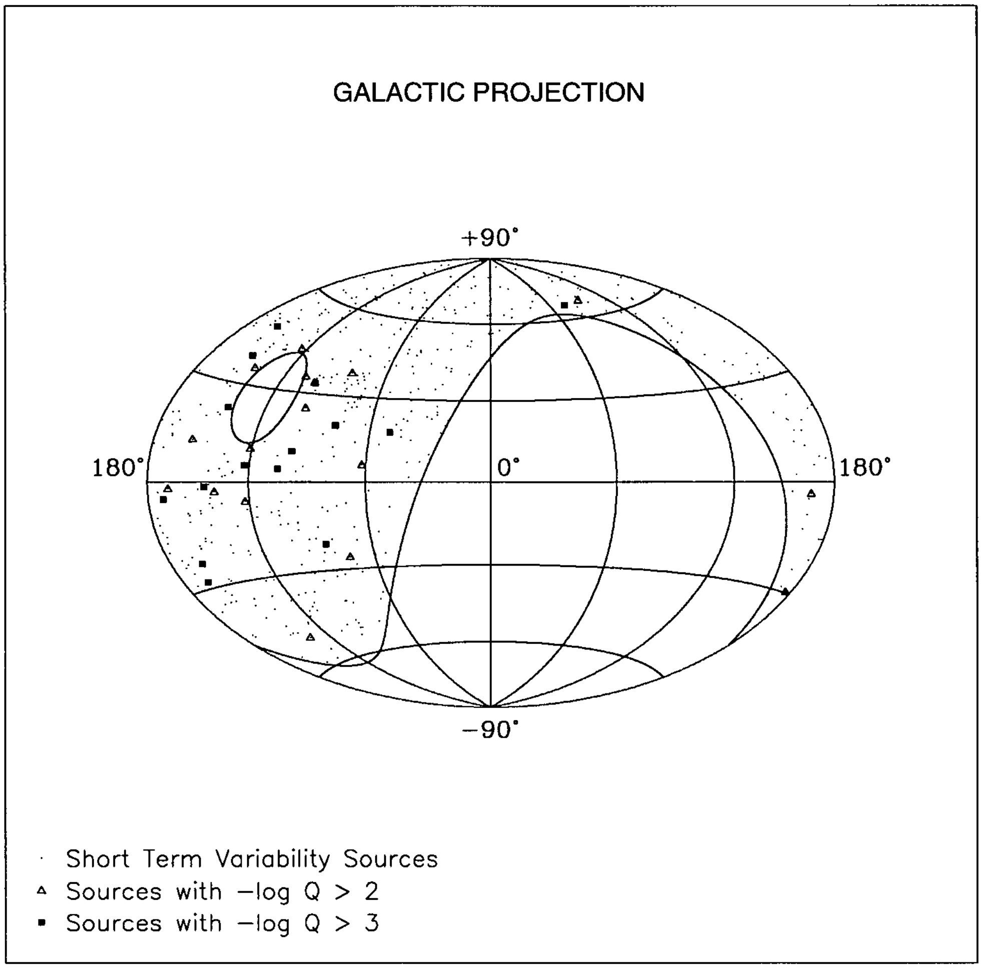

Figure 4.1: Galactic coordinate Aitoff projection of sources on short term variability list. Sources with either $-\log Q$ epoch values greater than 2 or 3 are highlighted.

is the same for both the 1986 and 1987 epochs, and most sources are not significantly variable ($\hat{Q} > 2$) on short time scales, at the achieved survey confidence levels.

Two scatter plots are included in figure 4.3, for $\hat{Q}$ at both epochs versus V_σ, the long term variability confidence level, and for 1986 $\hat{Q}$ values versus 1987 values. There is no obvious connection between $\hat{Q}$ and V_σ values, which is reasonable considering the large difference in time scales involved and statistical sampling effects. Since the long term and short term variability information is effectively uncoupled, the original restriction of the short term variability list to long term variables at approximately the 5 sigma level, or higher, is of little consequence, and the short term variability list can be considered a pseudo-random sample of GB6 short term variability. Unfortunately, there is also no obvious correlation between 1986 and 1987 $\hat{Q}$ values, suggesting that a fraction of the sources is only occasionally variable on short term time scales. However even consistently periodic short term variables may generate different $\hat{Q}$ values due to sampling effects.

To maximize short term variability, and the probability of observing variability during the VLA short term variability study, the sources in the short term variability list (STVL) were sorted by the multiplied 1986 and 1987 epoch $\hat{Q}$ values. The sorting function, used to prioritize the variables for further selection, is overlaid on the $\hat{Q}$ scatter plot in figure 4.3, for values of 1, 4, 9, and 16.

4.2 External Database Search

To gain further insight into the sources on the short term variability list, and to select sources without known identifications for further study, various databases were searched, with the results summarized in tables, only for the 178 sources (short term variables [STV]) with either $\hat{Q}$ epoch value ≥ 2, included in appendix A.

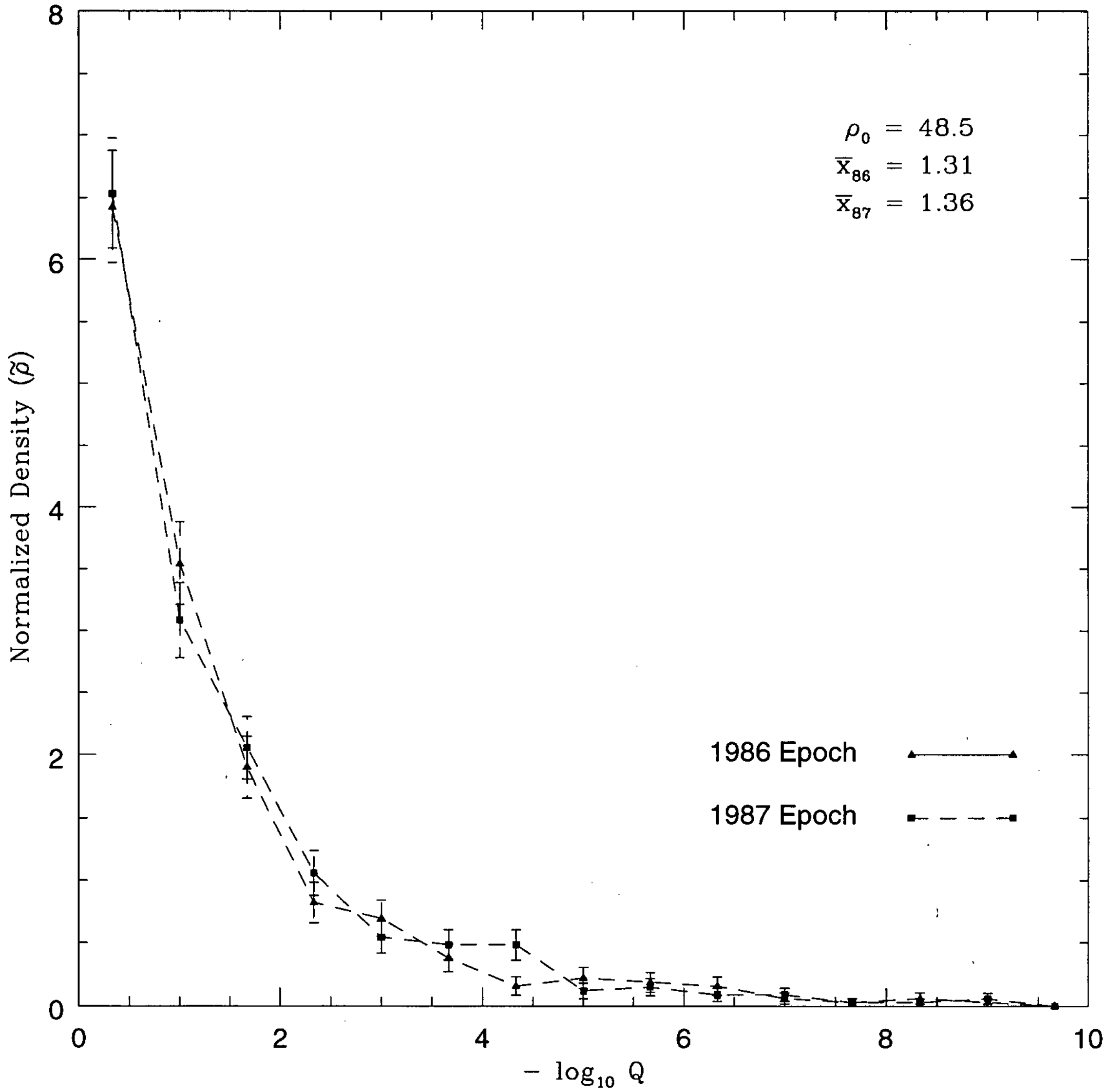

Figure 4.2: Normalized density of sources as a function of short term variability ($-\log Q$) for both 1986 and 1987 epochs.

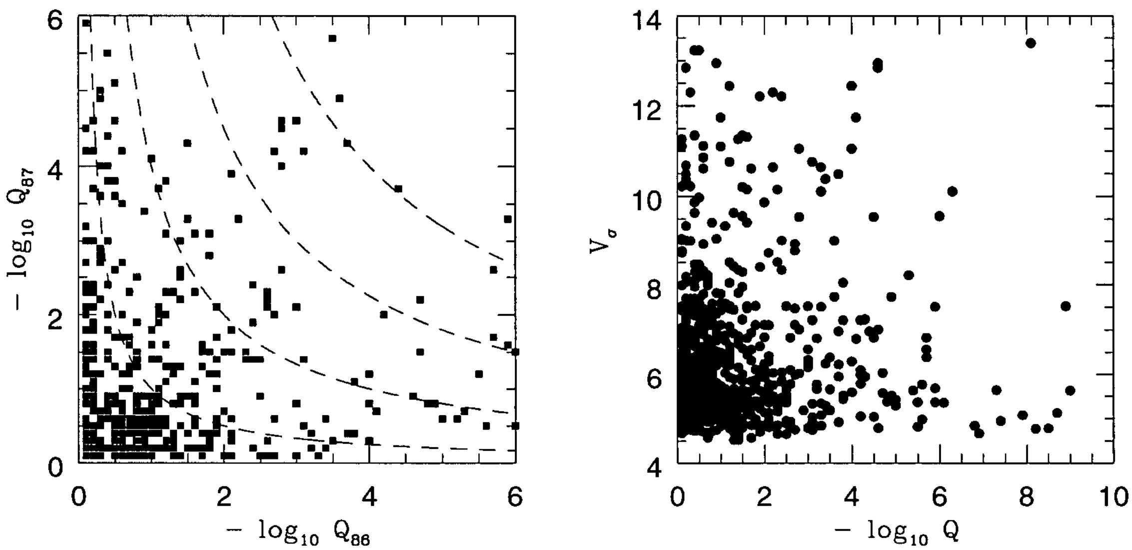

Figure 4.3: Scatter plot of 1986 versus 1987 epoch short term variability ($\hat{Q} \equiv -\log Q$), with the sorting function $\hat{Q}_{86} \times \hat{Q}_{87}$ overlayed for values of 1, 4, 9, and 16 at left. Scatter plot of short term variability versus long term variability confidence level V_σ at right.

4.2.1 NRAO VLA Sky Survey

To get high resolution images of any of the short term variables, it is desirable to have more precise pointing positions than those determined by the GB6 survey, with a characteristic uncertainty of 13″. The NRAO VLA Sky Survey (NVSS) is a project undertaken by NRAO to image the sky, at a resolution of 45″, between declinations of -40 and +90 degrees at 20 centimeters (1.4 Ghz). Products of the NVSS include intensity and polarization maps as well as a catalog of discrete sources with accurate positions, with minimum uncertainty of 0.3″ for strong sources, and flux density measurements, for all sources above the 2.5 mJy detection threshold. Currently, the NVSS catalog source information is available for approximately 50% of the overlap regions between the NVSS and GB6 surveys. The NVSS catalog was searched in January 1997 for positional matches within 30″ of the GB6 positions, to allow primarily for GB6 positional uncertainties. According to NVSS documentation, there is a 1% probability of a NVSS source occurring randomly at a distance of 30″ from any arbitrary position. NVSS matches were found for 93 of the short term variables (STV), within the 30″ boundary.

The best positions for all short term variables, with uncertainty in arcseconds are listed in appendix A.1. The positional catalog of origin, either NVSS or GB6, is also given along with positions in galactic coordinates. In appendix A.2, 1986 and 1987 epoch flux density measurements, F_{86} and F_{87}, as well as the combined flux density, F_6, from the GB6 catalog, and the NVSS flux density, F_{20}, are listed, along with the spectral indices derived from the 6 and 20 centimeter flux data. The GB6 short term variability 1986 and 1987 epoch $\hat{Q}$ values and the GB6 long term variability confidence level is also included in the table.

4.2.2 *SIMBAD* and *NED* Databases

Two comprehensive astrophysical databases, compiled from numerous catalogs at a wide range of wavelengths, were searched to determine which of the short term variables (STV) are previously identified sources. *SIMBAD*[1] is a database, primarily of galactic objects, with access provided by the Canadian Astronomy Data Center (CADC[2]). *SIMBAD* was searched for matches within 5″ of NVSS positions and 30″ of GB6 positions to allow for GB6 and NVSS position uncertainties as well as *SIMBAD* source position uncertainties. Of the short term variables, 42 matches were found, with the summarized results given in appendix A.3. The table includes the *SIMBAD* object classification, *SIMBAD* position

[1]SIMBAD is maintained by CDS (Centre de Donneés astronomiques de Strasbourg) at the Strasbourg Astronomical Observatory, an institute of Université Louis Pasteur in Strasbourg, France. SIMBAD documentation is found at http://cdsweb.u-strasbg.fr/Simbad.html .

[2]The CADC is operated by the Dominion Astrophysical Observatory for the National Research Council of Canada's Herzberg Institute of Astrophysics. The CADC homepage is accessed at http://cadcwww.dao.nrc.ca/.

and angular distance between GB6/NVSS and *SIMBAD* positions in arcseconds. Eighteen of the matches are identified as having appeared on a previous radio survey, with no other classification, and therefore does not disqualify a source from further study. The remaining classifications are dominated by 19 AGN, including radio galaxies, BL Lacertae objects, and a notable 11 QSOs, suggesting a $\hat{Q}$ dependent bias for highly relativistic beamed objects.

The NASA/IPAC Extragalactic Database (*NED*[3]) was searched, in a similar manner, for short term variable identifications. The *NED* includes known source names and aliases, photometry and redshift data when available, publication references, and multiple classifications based primarily on wavelengths at which the object has been detected. The *NED* search results are summarized in appendix A.4, for the 115 short term variables matched. Most of the matches correspond to previous detection by radio wavelength surveys, excluding the GB6 and NVSS surveys, with the number, if > 1, of independent detections, listed in the radio column of the table. The most common classifications, other than as a radio source, is as a QSO (21), an X-ray source (11), or a galaxy (7), and corresponding sources are identified in the table. Any other identification is given in the last column of the table, including most notably γ-ray sources (GammaS), infrared sources (IrS), visual sources (VisS), and either absorption (AbLS) or emission (EmLS) line sources. Again, QSOs dominate galaxies as specific classifications, with all but one of the X-ray detections associated with QSOs.

4.2.3 *APS* Optical Counterparts

Sources with positional accuracy on the order of an arcsecond, as obtained by NVSS, can be reliably correlated with optical counterparts. The Digitized Sky Survey (DSS) is a

[3]The NED is operated by the Jet Propulsion Laboratory, California Institute of Technology, under contract with the National Aeronautics and Space Administration. The NED is accessed via http://nedwww.ipac.caltech.edu/.

project by the Space Telescope Science Institute (STScI) to digitize the Palomar Observatory Sky Survey (POSS I) blue (O) and red (E) plates, and make the images available via the NASA/HEASARC virtual internet observatory "SkyView[4]". The University of Minnesota, in association with NASA and NSF, have undertaken the task of using an Automated Plate Scanner (*APS*[5]) to identify every source on the DSS images as either a star or a galaxy, and to derive source positions, magnitudes, and colour. Object classification is determined by a neural network algorithm, by computing probabilities based on source intensity profile, and it is implicitly assumed, for convenience, that objects can only be stars or galaxies. Currently, the *APS* research group claims a 90% classification success rate. Photometry for stars is calculated using a calibrated magnitude-diameter relationship, and photometry for galaxies is based on derived and calibrated density to intensity transformations. With precise plate scanning measurements and plate distortion corrections, the calibrated position total errors are approximately $0.6''$. When completed, the *APS* catalog should include millions of sources, with absolute galactic latitude > 20 degrees. Currently only a fraction of the project data is available.

In January 1997, all short term variability sources (STVL) with NVSS positions were checked, within $3''$, in the *APS* catalog. The *APS* correlation results for the short term variables (STV) are listed in appendix A.5. The table includes *APS* classification, *APS* position, angular distance between *APS* and *NVSS* position in arcseconds, and the *APS* derived blue (O) magnitude and colour (O-E). Among the short term variables (STV) there were 16 *APS* matches, with 12 being identified as stars and 4 as galaxies. It is clear from the *NED* and *SIMBAD* identifications that *APS* will characteristically misclassify

[4]*SkyView was developed and is maintained by NASA under the auspices of the High Energy Astrophysics Science Archive Research Center (HEASARC) at the GSFC Laboratory for High Energy Astrophysics. The SkyView homepage URL is http://skview.gsfc.nasa.gov/skyview.html .*

[5]The APS Catalog of the POSS I is supported by the National Science Foundation, the National Aeronautics and Space Administration, and the University of Minnesota. The APS databases can be accessed at http://isis.spa.umn.edu/.

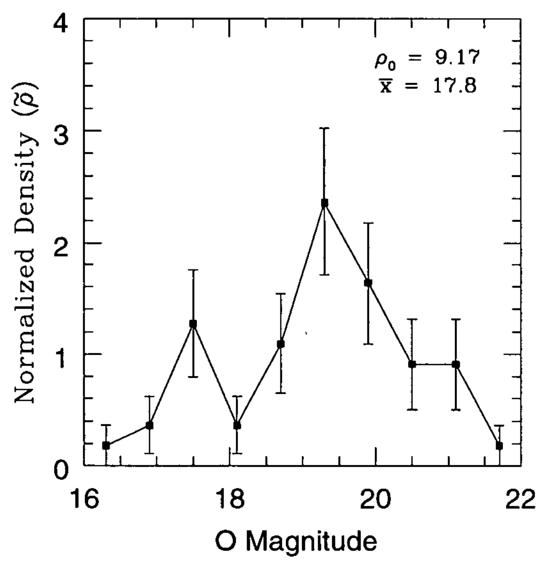

Figure 4.4: Normalized density of *APS* matched short term variability sources as a function of magnitude (left) and colour (right).

an AGN as a star, since a third of the short term variables (STV) identified by *APS* as stars is identified by *NED* as a QSO or by *SIMBAD* as some type of AGN.

For completeness, the normalized density of magnitude and colour of the short term variability (STVL) sources is shown in figure 4.4. Although the distributions are intriguing, it must be cautioned that any direct interpretation is difficult since neither galactic extinction, interstellar reddening, nor *APS*/DSS selection effects have been corrected, and small number statistics may further distort the underlying distribution.

4.3 Selected Variable Sources for VLA Study

From the list of short term variables (STV), prioritized by multiplied epoch $\hat{Q}$ values, and with all previously identified sources removed, the top 24 sources were chosen for Very Large Array (VLA) imaging. The number of sources chosen for study was based on initial expectations for VLA time allotted and estimates of observation time required per source to achieve sufficient sensitivity at two wavelengths.

A separate summary of source positions in J2000 coordinates, with uncertainty in arcseconds, positional catalog of origin, and position in galactic coordinates is given in table 4.1. A plot of position in an Aitoff galactic projection, for the 24 sources selected for VLA study, are highlighted in figure 4.5 along with galactic positions for all sources on the parent short term variability list (STVL). It is worthy of note that, even though galactic position was not a selection criterion, of the 24 sources, 11 lie within 15 degrees of the galactic plane, which is at least encouraging since it is hoped that some of the studied objects are galactic. Flux density measurements from the 1986 epoch, 1987 epoch, and combined GB6 data, the NVSS flux measurements and derived spectral indices, α, as well as the 1986 epoch and 1987 epoch $\hat{Q}$ values, and long term variability sigma confidence level are summarized in table 4.2. The GB6 flux density measurements range from a relatively weak 25 mJy to a strong 626 mJy, averaging about 170 mJy, and of the spectral indices derived for NVSS matches, the majority is flat as expected. NVSS flux density measurements, and in particular, positional information, were available for only half of the sources just prior to the VLA observations. All the sources were also checked in a catalog of sources detected by the Faint Images of the Radio Sky at Twenty-cm (FIRST[6]) survey. The available catalog of the FIRST survey, with a detection threshold of 1 mJy, a resolution of $5''$, and with positional accuracy $< 0.5''$, is currently sparse, and only one source, J1106+282, which already is NVSS matched, was found. The FIRST measured flux density, of 215 mJy, is consistent, especially considering GB6 levels of variability, with the NVSS measurement.

By definition of the selection process, none of the 24 sources has specific previous identifications; however a number have appeared in other radio surveys. The *SIMBAD*

[6]The FIRST homepage is available at http://sundog.stsci.edu/ .

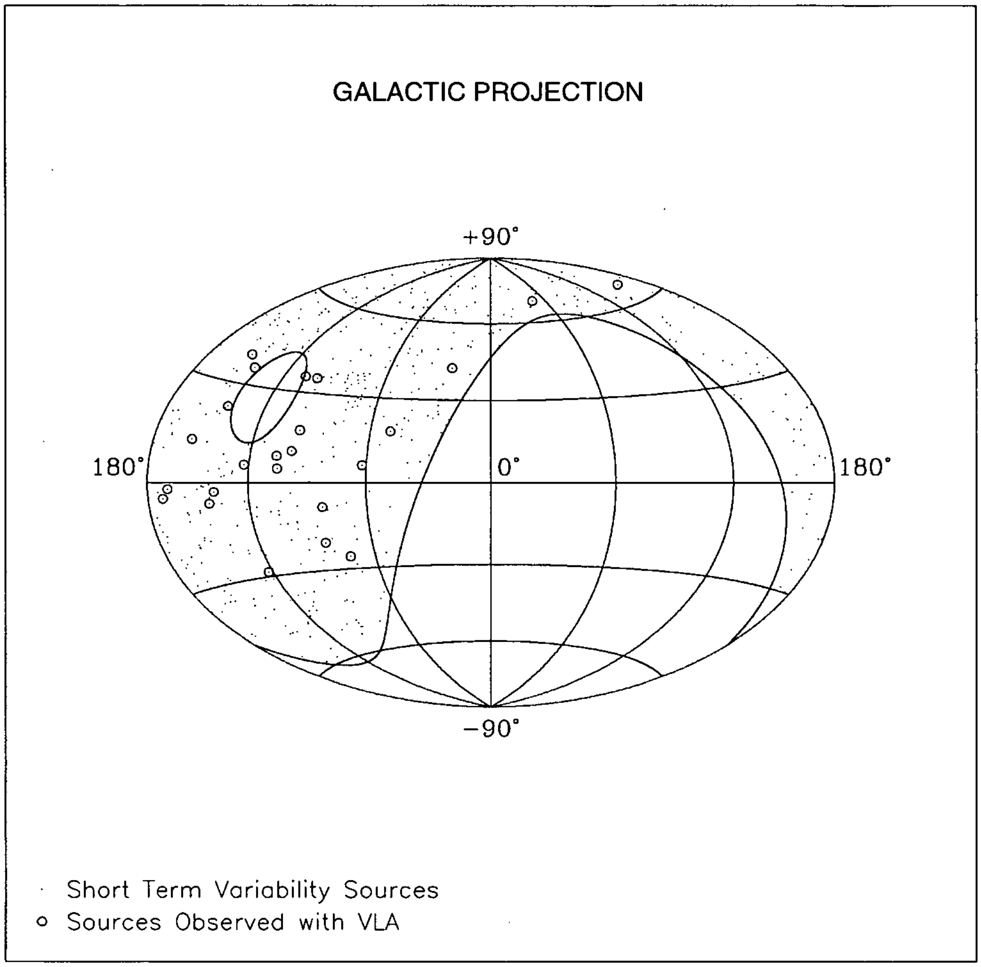

Figure 4.5: Galactic coordinate Aitoff projection of short term variables selected for VLA study along with distribution of all short term variability sources. GB6 survey boundaries are as shown.

Table 4.1: Selected Source Position Information

NAME	J2000 Position		±	Catalog	Galactic	
J0048+684	0:48:35.4	+68:26:29	9	GB6	5.6	122.7
J0049+343	0:49:45.7	+34:22:30	12	GB6	-28.5	122.5
J0251+562	2:51:54.53	+56:16:19.1	0.4	NVSS	-2.8	139.1
J0259+516	2:59:38.23	+51:38:14.5	0.4	NVSS	-6.3	142.3
J0502+388	5: 2:32.46	+38:49:54.9	0.5	NVSS	-1.8	166.8
J0502+346	5: 2:29.88	+34:36:34.7	0.4	NVSS	-4.4	170.2
J0532+562	5:32:59.47	+56:12:24.8	0.4	NVSS	12.3	155.4
J0611+723	6:11: 9.20	+72:18:16.3	0.5	NVSS	22.8	141.9
J0856+717	8:56:54.60	+71:46:24.9	0.4	NVSS	35.3	142.0
J0903+636	9: 3:37.94	+63:38:11.8	0.4	NVSS	38.6	151.4
J1106+282	11: 6: 7.22	+28:12:47.3	0.4	NVSS	66.7	204.1
J1307+064	13: 7: 4.0	+ 6:27:54	13	GB6	69.0	313.8
J1603+110	16: 3:42.7	+11: 5:46	11	GB6	42.2	23.0
J1630+741	16:30:26.52	+74: 9:33.1	0.4	NVSS	35.4	107.1
J1700+685	17: 0: 9.24	+68:30: 6.5	0.4	NVSS	35.2	99.6
J1814+228	18:14: 1.5	+22:49: 3	24	GB6	18.1	49.9
J1924+286	19:24:14.7	+28:38: 0	12	GB6	6.1	62.0
J1956+635	19:56:25.8	+63:32:42	8	GB6	17.3	96.3
J2055+613	20:55:39.4	+61:22: 1	8	GB6	10.4	98.3
J2115+367	21:15:39.5	+36:45:56	11	GB6	-8.4	82.0
J2145+187	21:45:14.35	+18:45:19.8	0.4	NVSS	-25.7	73.2
J2152+653	21:52:28.0	+65:20:35	9	GB6	8.7	105.7
J2202+292	22: 2: 5.3	+29:14:53	12	GB6	-20.6	84.1
J2208+615	22: 8:10.2	+61:32:55	11	GB6	4.6	104.7

radio position and angular separation, in arcseconds, from GB6/NVSS position is included in table 4.3 along with *NED* radio matches, with number of surveys (if > 1) and survey names listed. The most common radio survey catalog (WB92) is based on the Westerbork Northern Sky Survey (WENSS) at 92 centimeters. Other catalogs listed include the 7C and 8C, part of a series of Cambridge University surveys, at 151 MHz and 38 MHz respectively, taken with the Mullard Radio Astronomy Observatory (MRAO).

All radio surveys listed in table 4.3, compared to VLA capabilities, are low resolution and therefore offer no significant insight into possible sub-arcsecond structural variation of our selected sources. Since many of our selected sources have appeared in other surveys it is not unexpected that 13 have also been previously observed with the VLA in A, B, or hybrid configuration (table 4.3). However, according to VLA archive records, all of the previous observation programs are inconsistent with our multi-epoch observing

Table 4.2: Selected Source Flux Related Information

NAME	F_{86}	F_{87}	F_6	F_{20}	α	$-logQ_{86}$	$-logQ_{87}$	V_σ
J0048+684	49 ± 4	102 ± 5	81 ± 8			5.9	3.3	7.5
J0049+343	87 ± 6	141 ± 8	111 ± 10			5.9	1.6	5.4
J0251+562	352 ± 13	252 ± 10	310 ± 27	196 ± 6	-0.4	4.2	2.0	6.1
J0259+516	119 ± 6	61 ± 5	96 ± 9	89 ± 3	-0.1	1.2	11.7	7.1
J0502+388	172 ± 9	289 ± 13	239 ± 21	60 ± 2	-1.1	2.5	8.9	7.5
J0502+346	70 ± 6	114 ± 7	106 ± 10	178 ± 6	0.4	3.3	6.8	4.8
J0532+562	89 ± 5	130 ± 6	113 ± 10	111 ± 4	0.0	7.4	2.5	5.0
J0611+723	44 ± 4	116 ± 6	87 ± 8	60 ± 2	-0.3	6.3	3.3	10.1
J0856+717	144 ± 6	208 ± 7	174 ± 16	64 ± 2	-0.8	2.8	4.6	7.0
J0903+636	17 ± 5	33 ± 5	25 ± 4	50 ± 2	0.6	6.2	7.1	2.3
J1106+282	537 ± 24	274 ± 13	369 ± 33	225 ± 7	-0.4	6.0	1.5	9.6
J1307+064	151 ± 10	263 ± 14	146 ± 14			11.5	0.9	6.5
J1603+110	363 ± 18	831 ± 39	626 ± 55			0.6	16.8	10.9
J1630+741	86 ± 5	139 ± 6	116 ± 10	300 ± 9	0.8	5.7	2.6	6.8
J1700+685	341 ± 11	435 ± 13	380 ± 34	351 ± 12	-0.1	4.7	1.5	5.6
J1814+228	18 ± 7	40 ± 7	29 ± 5			7.0	6.0	2.2
J1924+286	140 ± 8	47 ± 5	92 ± 9			2.8	4.5	9.5
J1956+635	364 ± 12	143 ± 6	136 ± 12			22.2	1.8	16.1
J2055+613	307 ± 11	414 ± 14	385 ± 34			3.7	4.3	5.9
J2115+367	71 ± 6	136 ± 8	110 ± 10			1.6	13.4	6.8
J2145+187	45 ± 6	88 ± 7	71 ± 7	79 ± 2	0.1	2.6	2.2	4.8
J2152+653	76 ± 5	111 ± 6	92 ± 9			8.5	1.2	4.8
J2202+292	71 ± 6	116 ± 7	97 ± 9			3.0	4.6	4.8
J2208+615	47 ± 4	92 ± 5	67 ± 7			3.5	5.7	6.4

strategy, typically consisting of one single-epoch, single-frequency snapshot. Usually, for even higher resolution VLBA or VLBI imaging, VLA imaging is a precursor, and the general lack of attention these sources have been afforded ensure that we avoid duplicating previous structural variability research.

The GB6 short term flux density measurements for the 24 selected sources are plotted in figures 4.6 to 4.11 for both 1986 and 1987 epochs, with the first measurement in each epoch defined as occurring on day one. By selection criteria, all sources exhibit significant short term variability, on time scales from a day to a month, in at least one epoch, preferentially in both, and all sources exhibit long term variability, on a year time scale, by default because of sample list origin. A short term variation amplitude may be defined as the flux density standard deviation, normalized by the average flux density. The variation amplitudes for the selected sources, averaged over both epochs,

Table 4.3: Selected Source Database Information

NAME	SIMBAD			NED		VLA
	Class	Position (J2000)	Distance (″)	Radio	Survey	(A/B)
J0048+684						•
J0049+343				•	WB92	•
J0251+562						•
J0259+516						
J0502+388	Radio	5: 2:32.45 +38:49:52.5	2.40	•	B3	
J0502+346				•	WB92	
J0532+562						•
J0611+723						•
J0856+717				•	WB92	•
J0903+636				•	8C	
J1106+282				•	WB92	•
J1307+064				•	WB92	•
J1603+110				•	WB92	
J1630+741	Radio	16:30:25.83 +74: 9:33.5	2.80	3	WB92,7C,8C	•
J1700+685	Radio	17: 0: 9.02 +68:30: 5.7	1.40	3	WB92,7C,8C	•
J1814+228						
J1924+286				•	WB92	
J1956+635				•	WB92	
J2055+613				•	WB92	•
J2115+367				•	EF	•
J2145+187				•	WB92	
J2152+653				2	WB92,8C	
J2202+292				•	WB92	•
J2208+615						

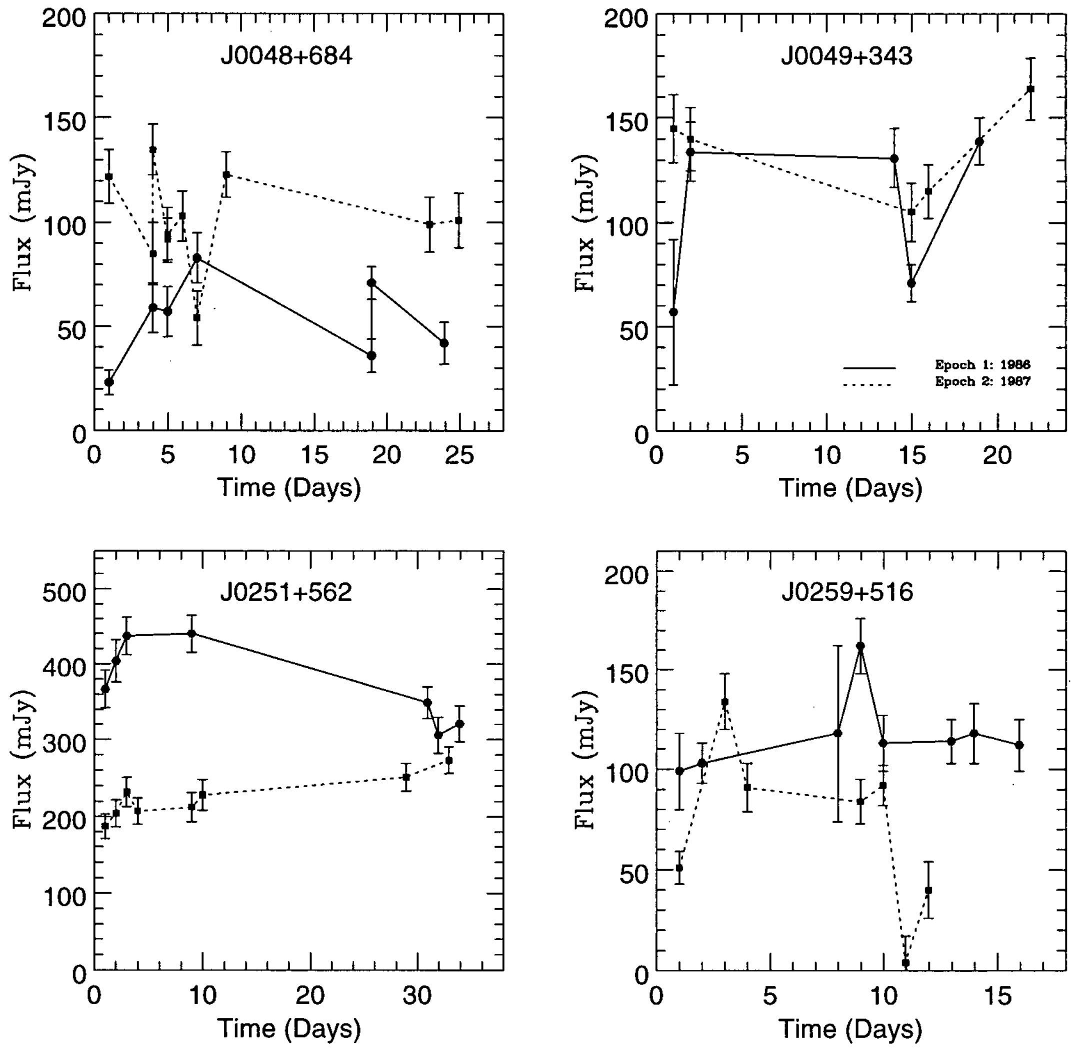

Figure 4.6: Plot of GB6 daily flux density measurements during 1986 (solid line) and 1987 (dashed line) epochs for sources J0048+684, J0049+343, J0251+562, and J0259+516.

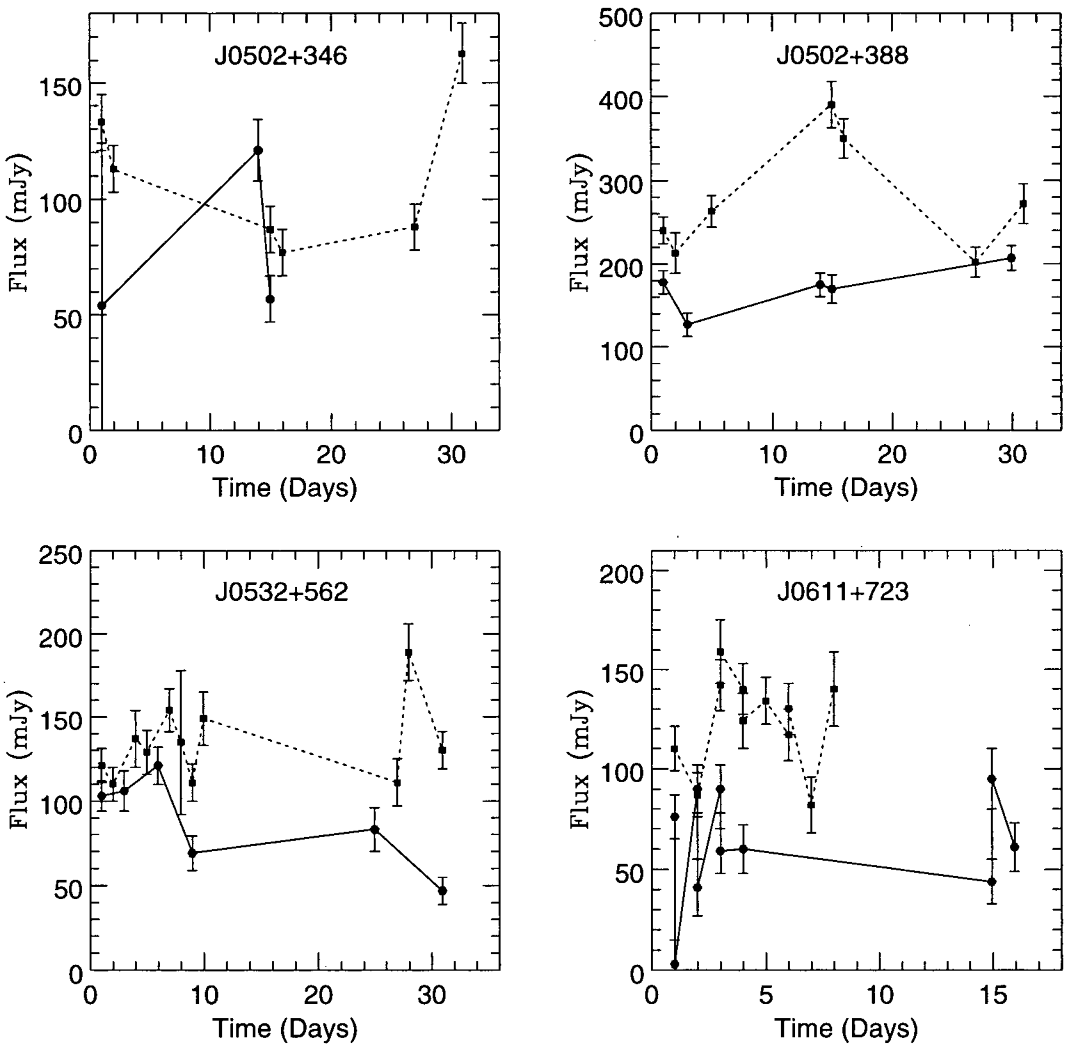

Figure 4.7: Plot of GB6 daily flux density measurements during 1986 (solid line) and 1987 (dashed line) epochs for sources J0502+346, J0502+388, J0532+562, and J0611+723.

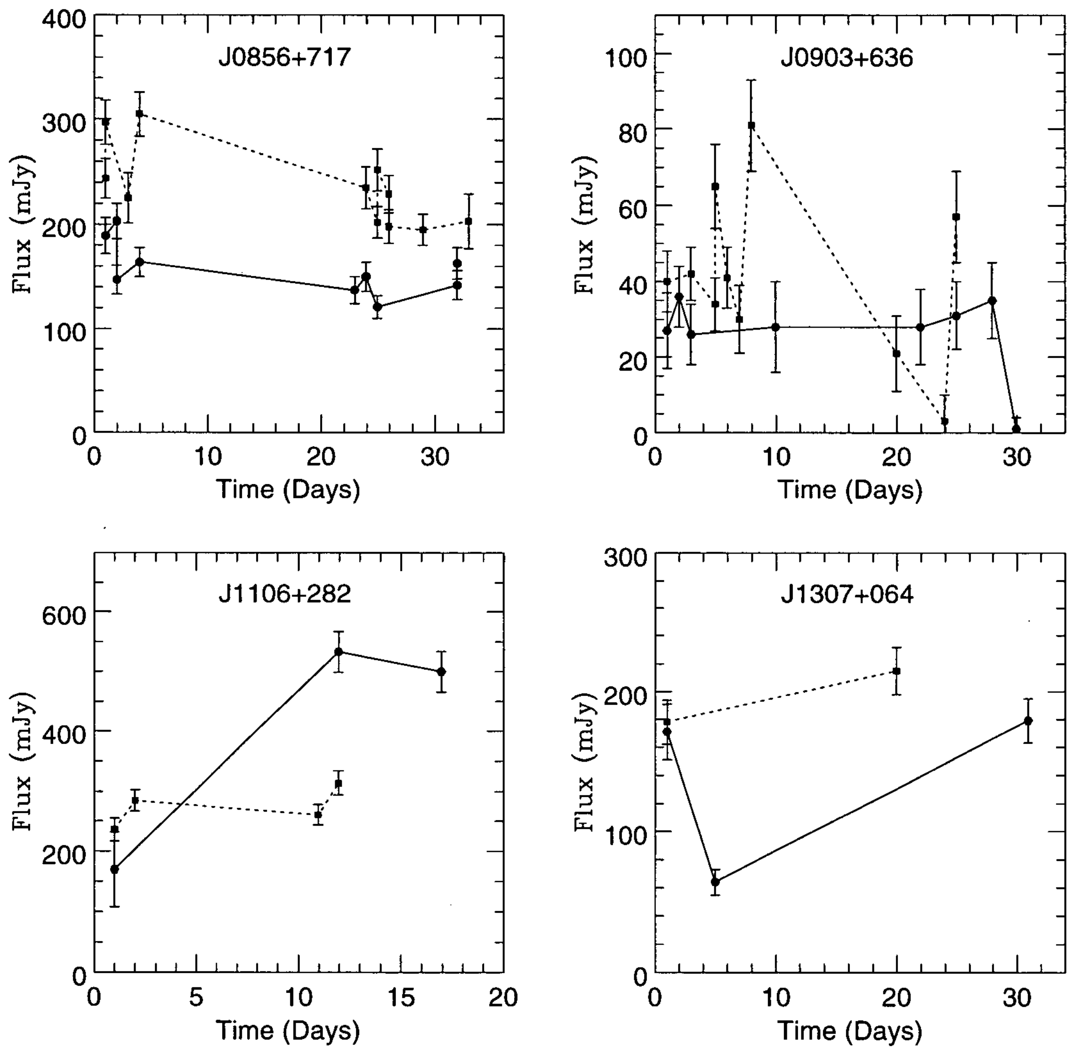

Figure 4.8: Plot of GB6 daily flux density measurements during 1986 (solid line) and 1987 (dashed line) epochs for sources J0856+717, J0903+636, J1106+282, and J1307+064.

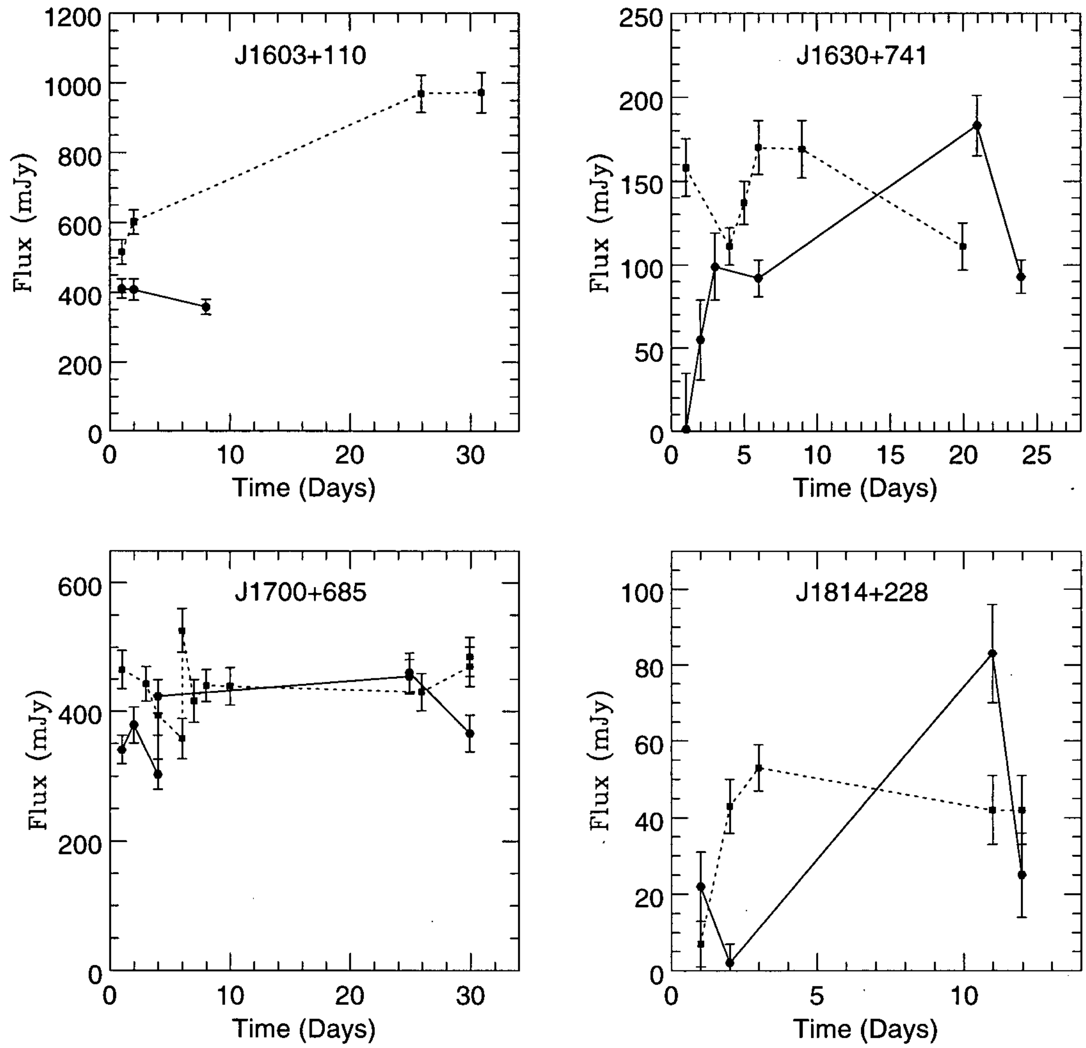

Figure 4.9: Plot of GB6 daily flux density measurements during 1986 (solid line) and 1987 (dashed line) epochs for sources J1603+110, J1630+741, J1700+685, and J1814+228.

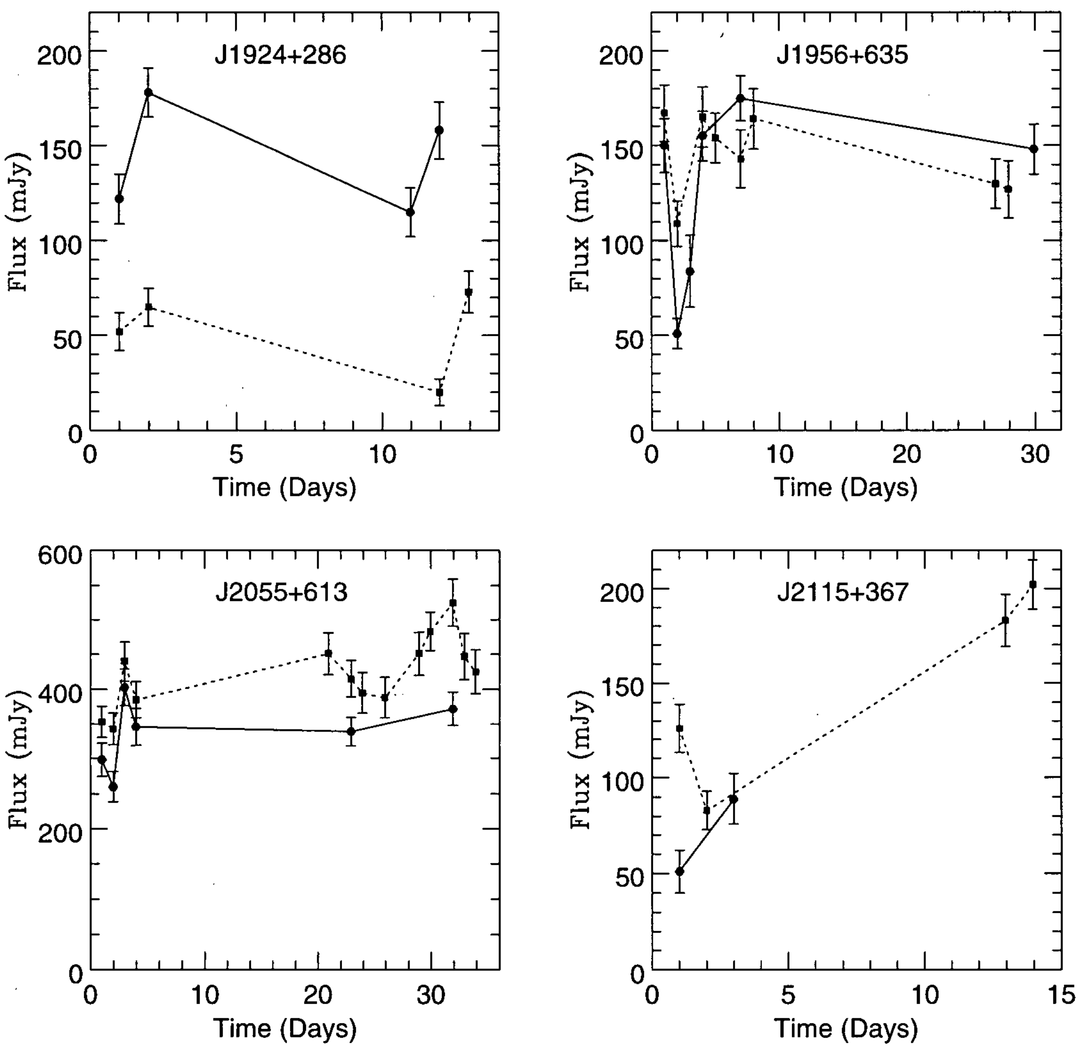

Figure 4.10: Plot of GB6 daily flux density measurements during 1986 (solid line) and 1987 (dashed line) epochs for sources J1924+286, J1956+635, J2055+613, and J2115+367.

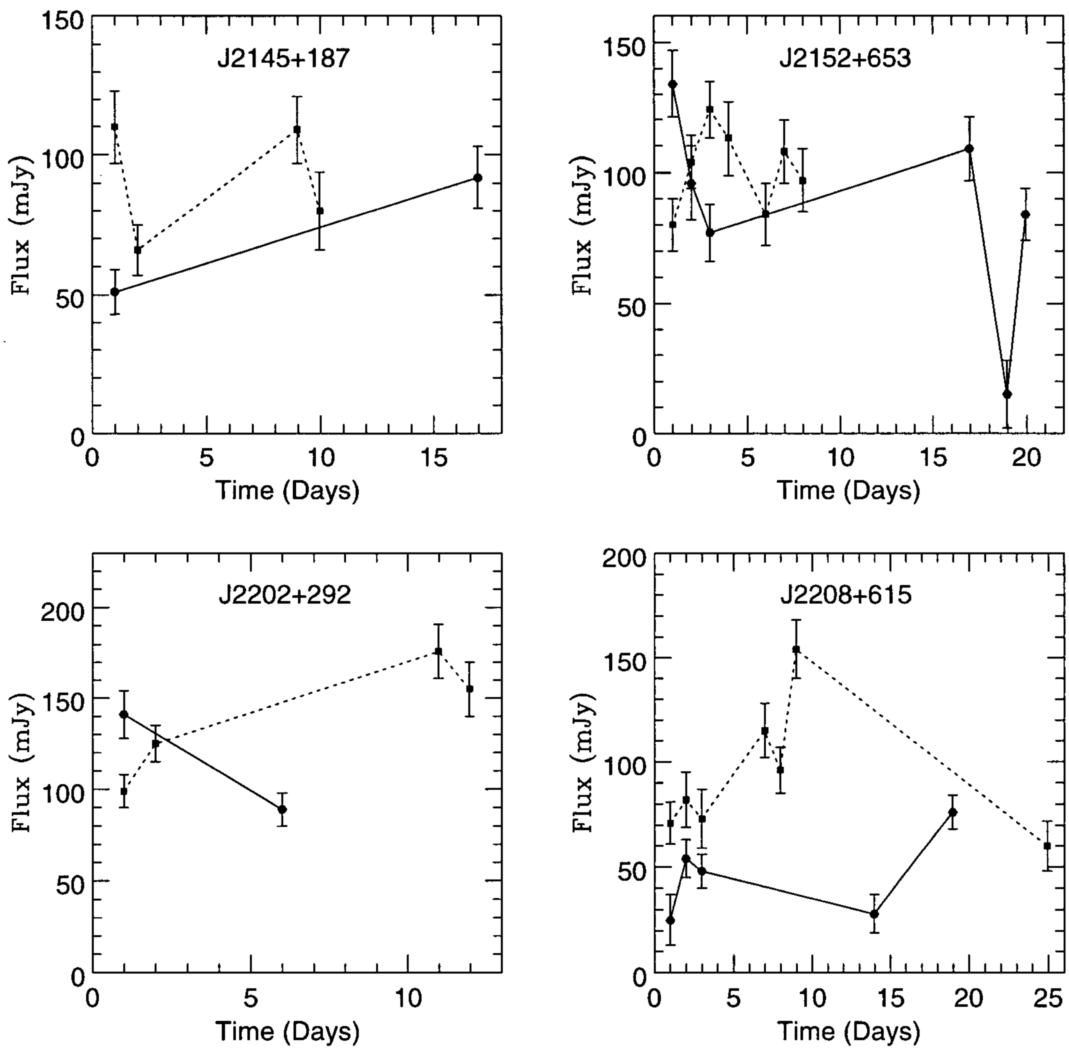

Figure 4.11: Plot of GB6 daily flux density measurements during 1986 (solid line) and 1987 (dashed line) epochs for sources J2145+187, J2152+653, J2202+292, and J2208+615.

range from 13% to 76%, with a mean value of 31%. It is apparent, from the short term flux density graphs, that each individual source varies on a wide range of time scales, perhaps due to different mechanisms, and the selected sample as a whole also includes some different time scale variation patterns. Sources such as J0251+562 and J0502+388 seem to be characterized more strongly by monthly variations where as sources like J0611+723 and J1700+685 appear to be indicative of more rapid daily fluctuations, with the majority of sources varying significantly on both monthly and daily time scales. It is difficult to physically interpret the flux density plots and the derived flux density variations. Random sampling effects and small number statistics tend to obscure the true flux density variations. However, the significant flux density variations, with associated $\hat{Q}$ confidence levels, occurring on such short time scales, warrant further detailed study, specifically with high resolution, multi-epoch, multi-frequency VLA imaging.

Chapter 5

Radio Imaging with the VLA

5.1 Interferometry and Aperture Synthesis

The Very Large Array (VLA[1]) is a radio telescope used for aperture synthesis, and is composed of 27 antennas arranged on a Y-shaped track, located on the San Agustin desert in New Mexico. The antennas are regularly cycled through four main configurations, known as A, B, C, and D as well as various hybrids, with a maximum extent of 36 kilometers in A configuration for high resolution imaging, down to 1 kilometer in D configuration for wide field imaging. The VLA is capable of imaging radio sources in the northern hemisphere with resolution comparable to optical telescopes, at wavelengths between 0.7 and 90 centimeters.

Each of the fully steerable, parabolic reflectors of the VLA is 25 meters in diameter, with an altazimuth mount and a Cassegrain focus. Antennas are equipped with four input channels, and therefore can monitor both left and right circularly polarized radiation components at two different frequencies, within a particular band, simultaneously. The total intensity, or Stokes I parameter, can be determined from the measured polarized intensity components.

$$I = RR^* + LL^* \tag{5.1}$$

[1]The VLA is operated by the National Radio Astronomy Observatory, which is a facility of the National Science Foundation operated under cooperative agreement by Associated Universities, Inc.

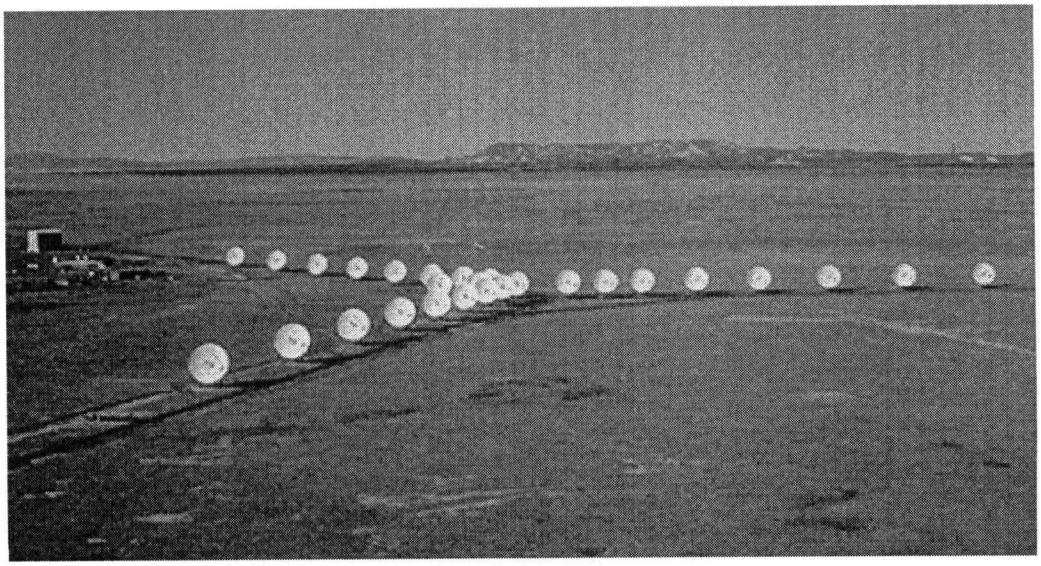

Figure 5.1: Overhead view of VLA in D configuration.

The spatial distribution of radio emission from any source in the sky may be considered a superposition of 2-dimensional Fourier components. Any component of the Fourier integral can be measured interferometrically by correlating the output signal from two antennas separated by an appropriate distance. A radio array with N antennas forms $N(N-1)/2$ interferometric pairs, and the VLA with 27 antennas, consists of 351 interferometers. By measuring a large number of the Fourier components, one can create an approximate reconstruction (aperture synthesis) of a source spatial intensity distribution. The VLA, with a finite number of elements, acts as a spatial filter on the sky intensity distribution, measuring particular Fourier components, determined by the projected antenna separations.

The technique of aperture synthesis can be summarized as a Fourier transform of the measured auto-correlation function, or complex visibility $V_\nu(u, v)$, where u and v are the projected antenna separations, expressed in wavelengths, equivalent to spatial frequencies.

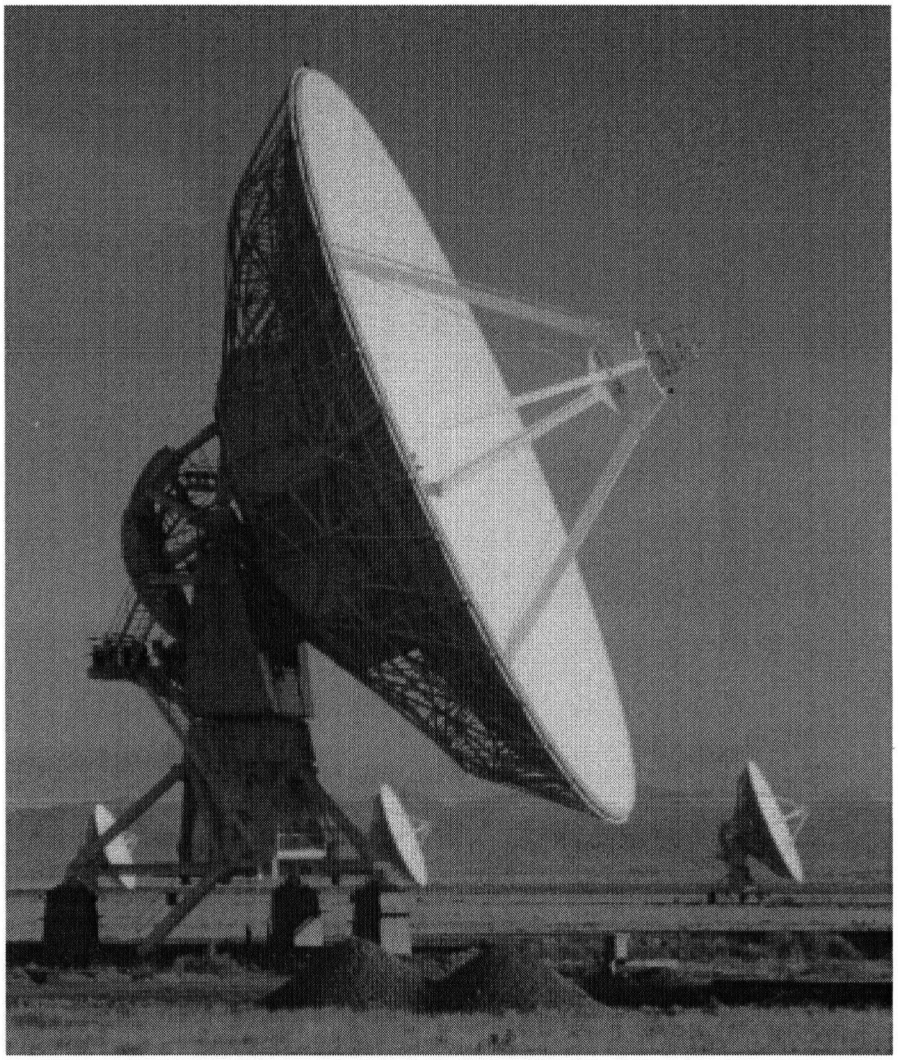

Figure 5.2: Close up view of a VLA antenna.

$$I_\nu^D(l,m) = \int\int V_\nu(u,v)S(u,v)e^{2\pi i(ul+vm)}\,dl\,dm \tag{5.2}$$

In reality, the continuous complex visibility is only sampled, and therefore must be multiplied by a discrete sampling function $S(u,v)$. The quality of the resultant "dirty" image, $I_\nu^D(l,m)$, is limited by the degree of sampling and the noise level in the complex visibility. The coordinates used for the image, l and m, are directional cosines of an angular position on the sky. Complex visibility is measured in units of Jansky (Jy), a flux density, and the image intensity is a surface brightness measured in Jansky per beam area, where

$$1 \;\; Jy = 10^{-26} \;\; \frac{W}{m^2\,Hz}.$$

The "dirty" image derived above is severely degraded by a complicated, spatially variable synthesized point spread function, making direct interpretation difficult. The "dirty" image is a convolution of a "real" image and the synthesized beam point spread function, $B(l,m)$.

$$I_\nu^D(l,m) = I_\nu(l,m) * B(l,m) \tag{5.3}$$

Generally, the "dirty" image is iteratively deconvolved using a 'lq cleaning" algorithm, generating a source model, which is then convolved with a elliptical gaussian approximation to the synthesized beam.

The field of view of the resultant "clean" image is diffraction limited by the primary beam width of the individual antennas. The resolution in the image is determined by the synthesized beam width, and only structure smaller than an angular scale defined by the minimum antenna separation, can be observed.

The above discussion of imaging is a simplification. As mentioned, the image quality is limited by noise, both intrinsic to the equipment, and from external interference.

Equation 5.2 assumes a coplanar array used for monochromatic observations of a planar intensity distribution. These assumption introduce radial image distortions which become increasingly significant further away from the pointing center. Other effects which degrade the image include atmospheric phase errors and sidelobes of the antenna reception pattern, particularly with bright "confusing" sources nearby. A detailed derivation of the aperture synthesis technique, as well as an in depth discussion of distortions and image quality, is given in reference [11].

5.2 VLA parameter selection

The purpose for observing a number of variable sources with the VLA was to obtain high resolution images at two epochs, separated by approximately a month, to elucidate any structural changes and flux variations over this time scale. Observations at two frequency bands allowed spectral index determination, as well as imaging frequency dependent structure. Two 24 hour observations in A configuration (highest resolution) were originally proposed. However only two 12 hour observations in B configuration were granted. The first 12 hour observation session (epoch A) began at 09:30 LST on March 19, 1997 followed by a second session (epoch B) at 09:30 LST on April 17, 1997.

The main observational strategy adopted comprised observing all 24 sources at X band (3.6 cm), a relatively sensitive frequency band, and either at U band (2 cm) for the majority of sources, or K band (1.3 cm) for the strongest sources, to take advantage of the slightly higher resolution. Important considerations for VLA parameter selection include sensitivity, image quality, and dynamic range, all of which are coupled. Clearly, one wishes to minimize the noise level, S_{rms}, which depends on the choice of integration time, Δt, and bandwidth, $\Delta\nu$, band dependent system temperature T_{sys}, and antenna efficiency ϵ, as well as the number of antennas, N, and input channels, n, of the array.

$$S_{rms} \simeq \frac{K}{\sqrt{N\,(N-1)\,n\,\Delta t\,\Delta\nu}} \tag{5.4}$$

$$K \approx \frac{0.12\,T_{sys}}{\epsilon} \tag{5.5}$$

Unfortunately, the minimum noise level achieved is restricted by the allotted time, and the image degrading effect of bandwidth smearing. A standard VLA bandwidth of 50 MHz was utilized for all observations. Approximate values of important VLA B configuration parameters are listed in table 5.1.

VLA Parameters: B configuration			
Band	X	U	K
Wavelength (cm)	3.6	2.0	1.3
Frequency (GHz)	8.0 - 8.8	14.4 - 15.4	22 - 24
Synthesized Beam Width (arcsec)	0.7	0.4	0.3
Primary Beam Size (arcmin)	5.4	3	2
Largest Angular Scale (arcsec)	20	12	7.3
RMS 10 min Sensitivity (mJy)	0.045	0.17	0.31
System Temperature (K)	34	110	160 - 190
Antenna Efficiency (%)	63	52	45

Table 5.1: VLA Parameters in B Configuration

Dynamic range, defined here as the peak surface brightness of an image, normalized by five times the noise level, is one measure of the image quality, and to a large degree determines the accuracy of flux measurements and the ability to discern faint extended emission associated with a source. Time spent per source was allocated such that the achieved dynamic range, based on GB6 flux measurements, for all sources would be ≥ 100 at the shortest wavelength of observation.

Since the VLA is a spatial filter, the detailed structure in a image is limited by the uv plane coverage. By observing each source at two different hour angles, defined by equation 5.6, greater uv sampling is achieved, resulting in improved image quality.

$$\text{Hour Angle} = \text{Local Sidereal Time} - \text{Right Ascension} \tag{5.6}$$

An essential part of VLA observation is absolute flux and phase calibration. The standard VLA flux calibrator 3C286 was chosen for flux amplitude calibration, and one phase calibrator was chosen, from the VLA calibrator manual [10], for each source, with the criterion that the calibrator be relatively strong, at least partially unresolved, with accurate position, and in close proximity to the source. The phase calibrators were only intended for coarse phase adjustments, since self-calibration imaging techniques were to be used. Whenever possible, phase calibrators were shared between sources for more efficient use of time.

In order to observe all 24 sources and calibrators at two different hour angles and at two different frequencies, observation times were restricted to snapshots, of order a few minutes. The source observations were scheduled within the given 12 hour time slot to ensure the sources were visible above the instrumental horizon, to maximize the difference in observed hour angles, and to minimize antenna move and set up time. The actual VLA observation is controlled by a user specified parameter file, created with *OBSERVE*, a computer program distributed by NRAO.

5.3 Imaging with *AIPS*

A software package, Astronomical Image Processing System, *AIPS*, has been designed by NRAO for editing, calibration, imaging and analysis of radio interferometric data, particularly suited for the VLA. Before an image can be made, the raw *uv* data must be edited, by flagging inconsistent baseline visibility amplitudes, and the remaining visibilities modified by gains computed during basic flux and phase calibration.

A fast fourier transform (FFT) is the most computationally efficient method of inverting the calibrated *uv* data. An automated mapping and self-calibration script called *MAPIT*, which coordinates a number of *AIPS* procedures, was used to image the VLA data. To perform the FFT, *MAPIT* must first interpolate the sampled *uv* data onto a regular, rectangular grid, then apply a user specified weighting factor based on data reliability, sample density, and a taper function, controlling synthesized beam shape. For all VLA maps generated, uniform weighting with no taper was used for best resolution. *MAPIT* self-calibrates each VLA image by iteratively solving for antenna gains, and then applying these to the data. Both the maximum number of iterations and image size are controlled by the user to reduce CPU time. The final, calibrated and cleaned, source model is convolved with an elliptical gaussian restoring beam, to produce a high dynamic range, snapshot image.

AIPS includes a number of analysis tasks to fit elliptical gaussians for source flux density and position measurements, to integrate flux densities over specified regions, and for noise and measured parameter error estimation. The process of interpreting and decomposing an image into components involves fitting an increasing number of elliptical gaussians to flux density peaks, until no further peaks are detectable in the image residuals at some confidence level cutoff. A relatively conservative peak detection confidence cutoff at 5σ noise contour level, was adopted with obvious VLA artifacts, if present, subjectively ignored. The fitted elliptical gaussian dimensions, compared to the restoring beam dimensions, are a further check on the quality of the component decomposition. Measured component flux densities, flux density uncertainties, positions and relative positional uncertainties are determined directly from the fitted gaussians and fitting uncertainties. Absolute position uncertainties of the brightest component are based on relative position uncertainty and scatter of a maximum of four independent position measurements, derived from the different epoch and wavelength images, and therefore incorporate random VLA pointing errors. Extended emission flux densities, when appropriate, are integrated over a delimiting box minimally encompassing the extended flux region, with the extent usually defined by the largest contiguous 2σ contour level. Various *AIPS* image display and contouring subroutines were used for the final image presentation.

Chapter 6

Results and Conclusion

The VLA images and data presented in this chapter are the culmination of careful selection of sources from the GB6 catalog believed to exhibit short term variability, and with no previous identification. Of the 24 sources imaged, 11 are at least partially resolved, 12 are unresolved, and one source did not appear in VLA imaged region, most likely due to inaccurate GB6 position. The majority of these sources is expected to be extragalactic. It was hoped that some of these sources will show significant structural variation or further evidence of extreme variability, consistent with either a galactic object, or interesting highly beamed sub-class of extragalactic objects.

6.1 Resolved Sources

The 11 resolved sources show varying levels of detail and are divided into three groups based on general physical appearance. The division, used here for convenience, is somewhat arbitrary, as one expects an underlying continuum in morphology, based on unified beam models for AGN's, and image structure must be interpreted in the context of achieved sensitivity and resolution. Any classification of these objects, without further study is only speculative.

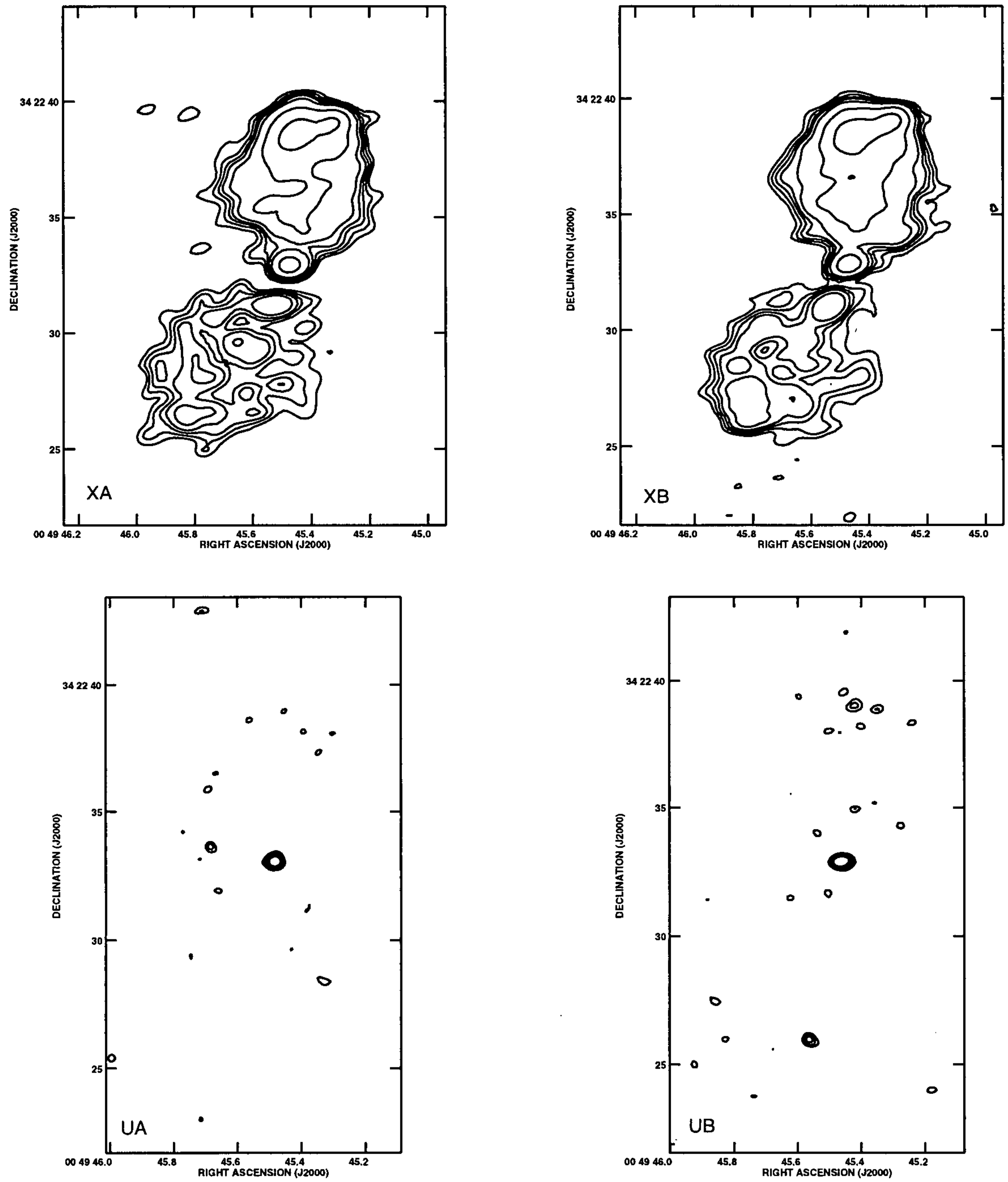

Figure 6.1: VLA images of J0049+343 at X and U band during epoch A and B as labeled. Contour levels are 3, 4, 5, 6, 8, 16, 32 times the noise level.

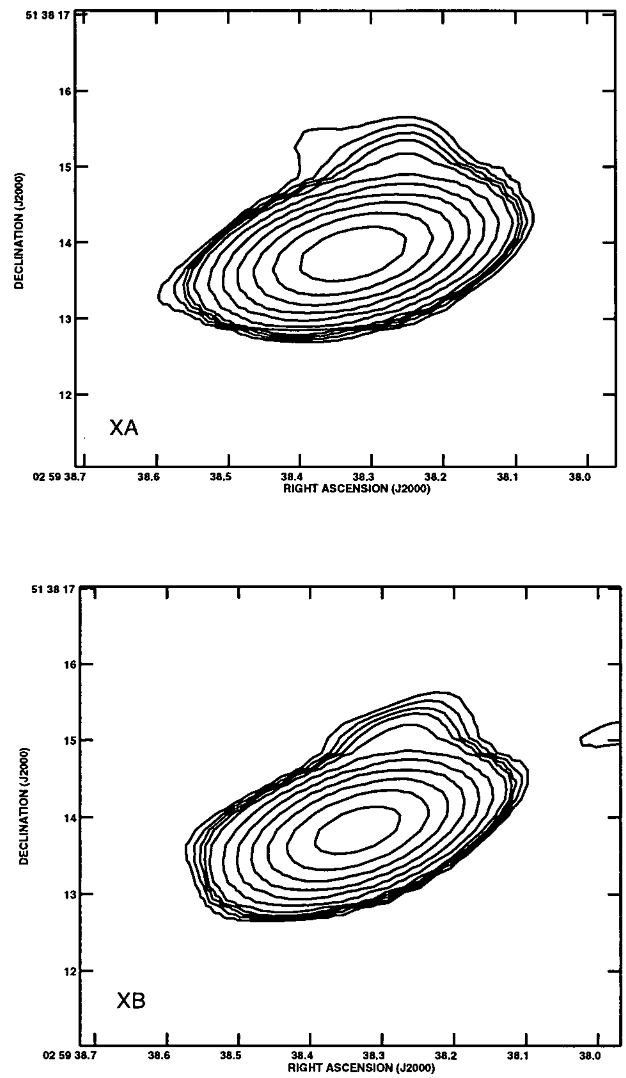

Figure 6.2: VLA images of J0259+516 at X band during epoch A and B as labeled. Contour levels are 3, 4, 5, 6, 8, 16, 32, 64, 128, 256, 512 times the noise level.

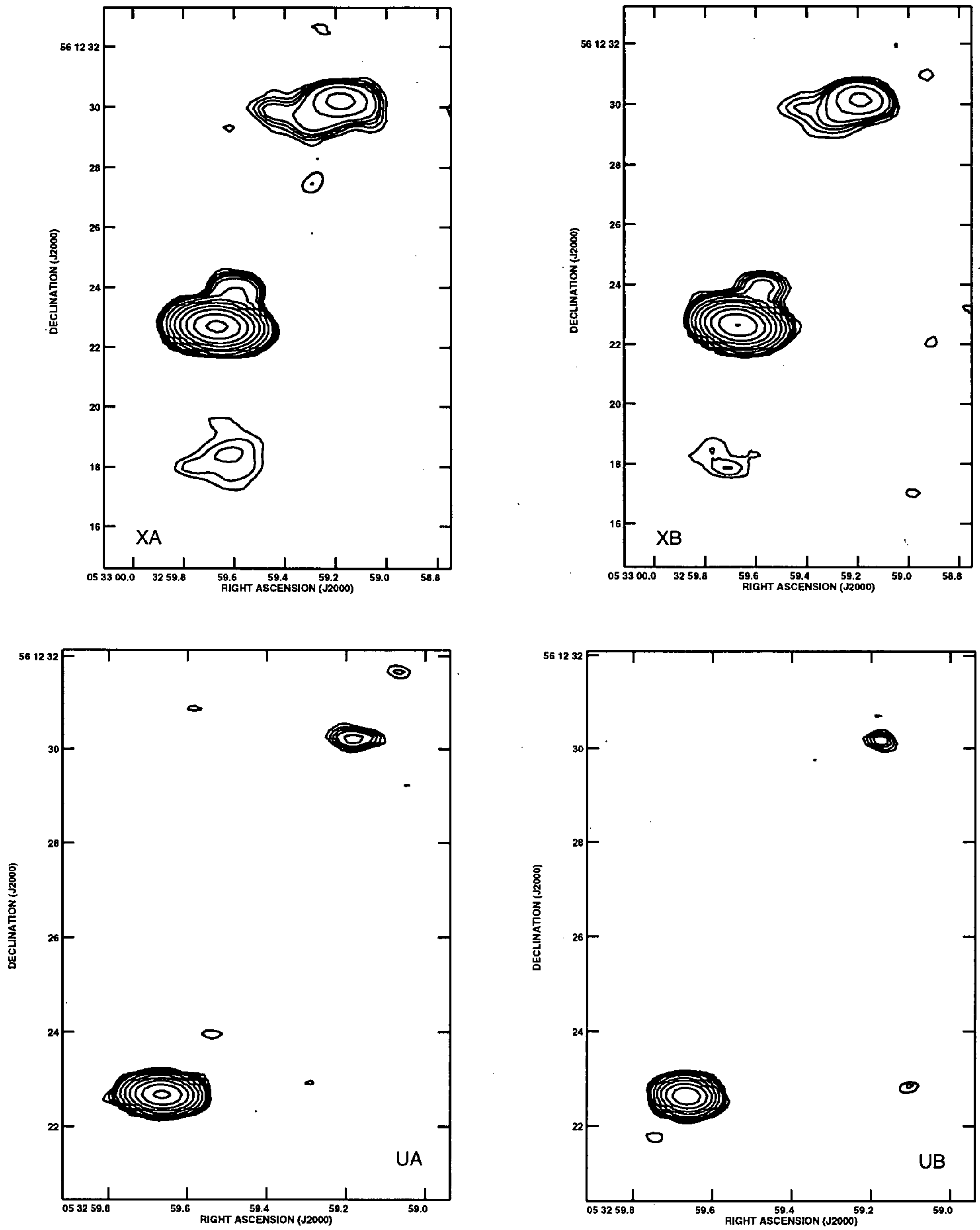

Figure 6.3: VLA images of J0532+562 at X and U band during epoch A and B as labeled. Contour levels are 3, 4, 5, 6, 8, 16, 32, 64, 128, 256, 512, 1024 times the noise level.

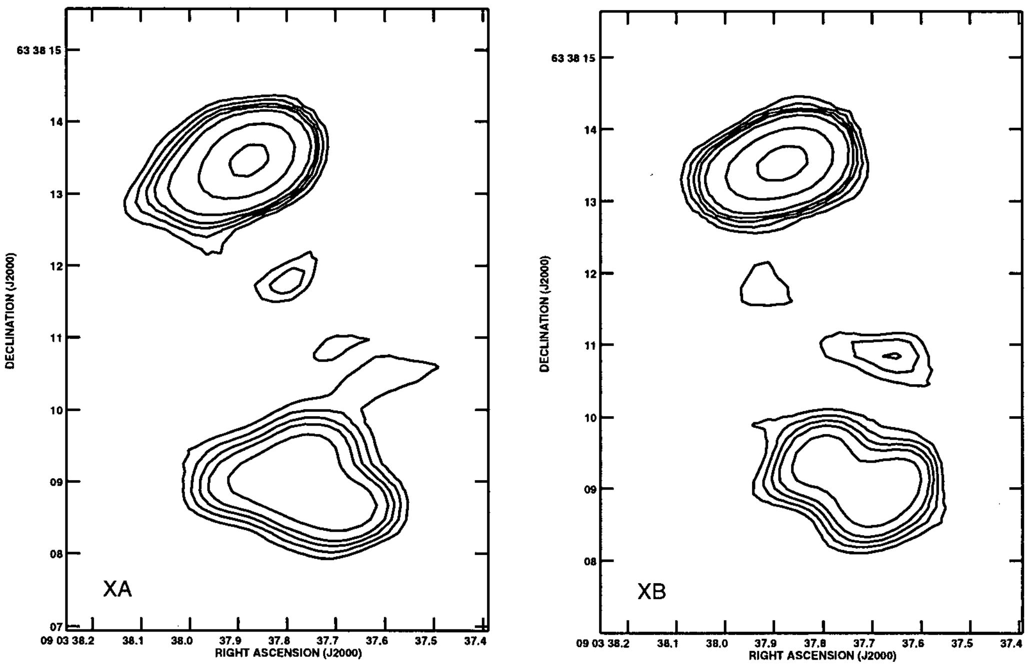

Figure 6.4: VLA images of J0903+636 at X band during epoch A and B as labeled. Contour levels are 3, 4, 5, 6, 8, 16, 32 times the noise level.

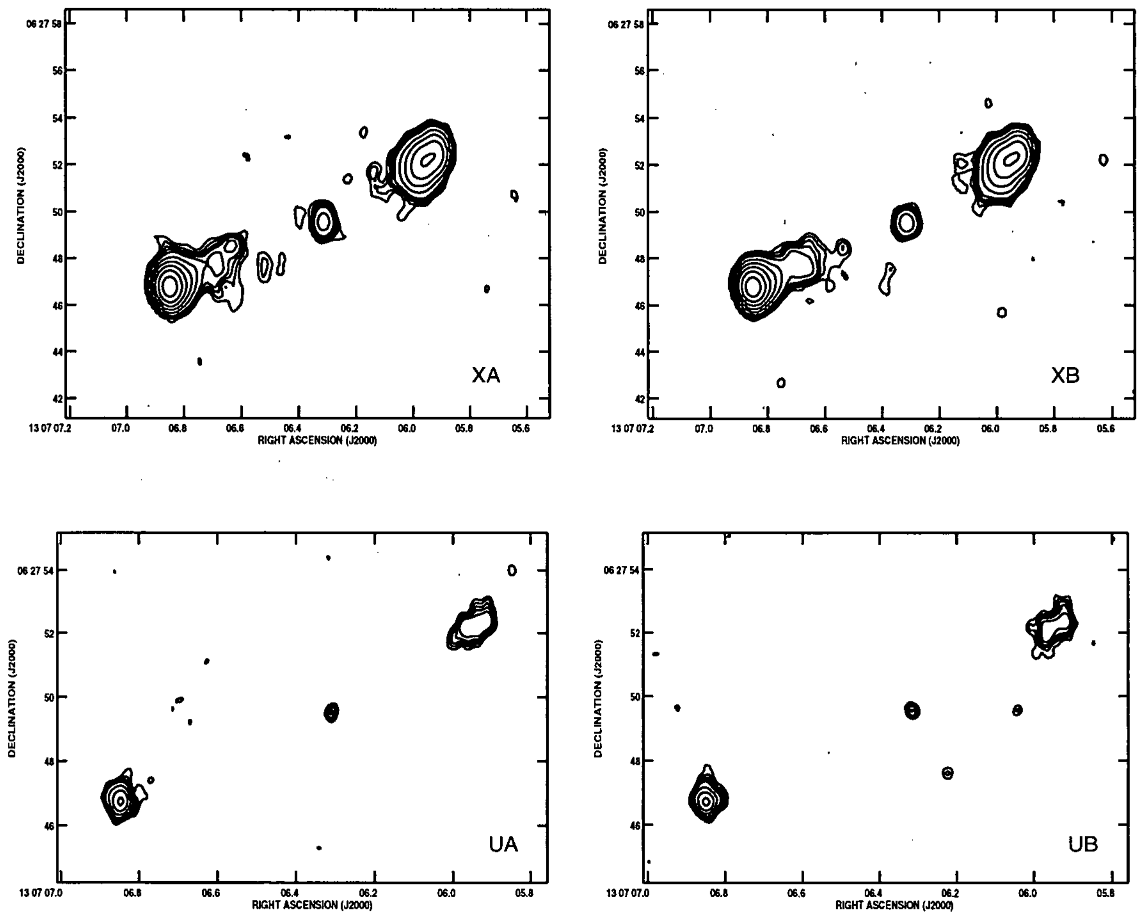

Figure 6.5: VLA images of J1307+064 at X and U band during epoch A and B as labeled. Contour levels are 3, 4, 5, 6, 8, 16, 32, 64, 128, 256 times the noise level.

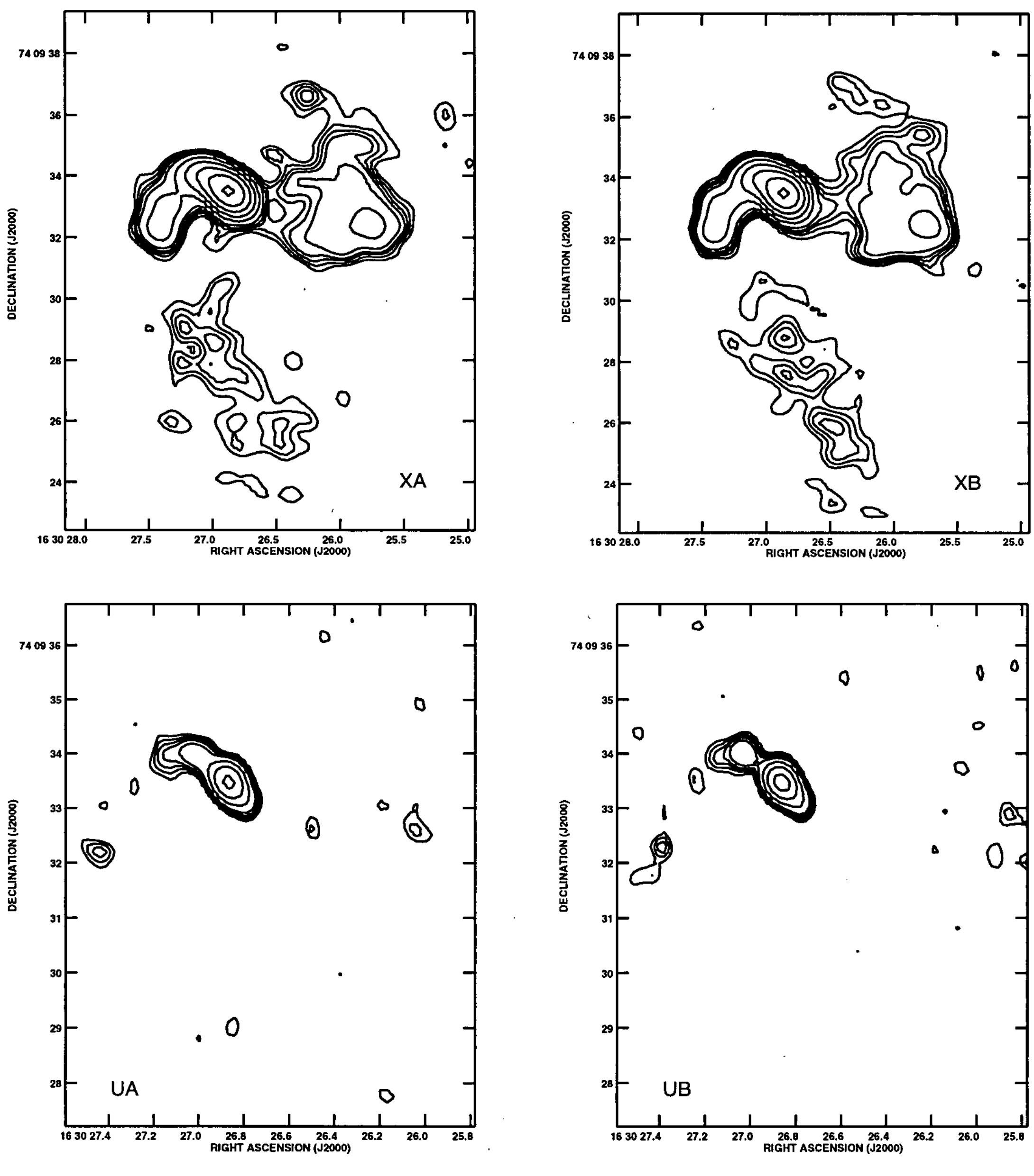

Figure 6.6: VLA images of J1630+741 at X and U band during epoch A and B as labeled. Contour levels are 3, 4, 5, 6, 8, 16, 32, 64, 128, 256 times the noise level.

SOURCE	BAND	Epoch A Noise ($\mu Jy/b$)	Epoch A Dynamic Range	Epoch A Beam Axis ($arcsec$)	Epoch A P.A. (deg)	Epoch B Noise ($\mu Jy/b$)	Epoch B Dynamic Range	Epoch B Beam Axis ($arcsec$)	Epoch B P.A. (deg)
J0048+684	X	205	138	1.24 × 0.70	92	125	239	1.17 × 0.70	96
	U	197	120	0.66 × 0.39	90	196	120	0.61 × 0.38	96
J0049+343	X	114	5	1.13 × 0.79	96	98	6	1.12 × 0.74	104
	U	206	3	0.57 × 0.46	96	192	3	0.57 × 0.39	99
J0251+562	X	125	617	1.60 × 0.69	105	113	628	1.54 × 0.69	109
	K	457	180	0.57 × 0.24	102	506	129	0.52 × 0.26	107
J0259+516	X	78	183	1.56 × 0.70	104	79	157	1.50 × 0.68	108
	U	212	63	0.85 × 0.39	102	197	61	0.80 × 0.36	108
J0502+346	X	115	369	1.41 × 0.77	73	133	239	1.37 × 0.73	70
	U	217	237	0.81 × 0.40	79	276	120	0.73 × 0.38	72
J0502+388	X	356	128	1.35 × 0.74	78	86	493	1.31 × 0.72	73
	U	242	209	0.79 × 0.42	82	308	137	0.70 × 0.39	76
J0532+562	X	82	253	1.35 × 0.71	85	92	210	1.26 × 0.70	81
	U	180	123	0.75 × 0.38	87	221	95	0.64 × 0.37	84
J0611+723	X	92	248	1.24 × 0.70	77	91	224	1.20 × 0.70	73
	U	1201	20	0.67 × 0.36	79	226	82	0.58 × 0.36	80
J0856+717	X	104	232	1.02 × 0.74	111	133	214	0.99 × 0.73	105
	U	216	175	0.59 × 0.40	112	269	140	0.52 × 0.40	113
J0903+636	X	74	7	1.04 × 0.70	116	72	8	0.99 × 0.70	109
	U	182	1	0.56 × 0.36	117	172	1	0.50 × 0.36	115
J1106+282	X	180	325	0.81 × 0.79	167	123	471	0.81 × 0.75	77
	K	341	150	0.31 × 0.25	159	413	130	0.28 × 0.27	133
J1307+064	X	91	82	0.94 × 0.75	3	87	84	0.87 × 0.76	7
	U	202	14	0.50 × 0.40	162	188	15	0.43 × 0.41	174
J1603+110	X	133	674	0.99 × 0.81	150	129	709	0.94 × 0.78	140
	K	554	160	0.36 × 0.29	159	612	145	0.34 × 0.28	132
J1630+741	X	92	55	0.98 × 0.73	53	89	54	0.89 × 0.76	48
	U	206	14	0.51 × 0.40	28	176	17	0.47 × 0.38	36
J1700+685	X	102	430	0.92 × 0.75	54	125	416	0.85 × 0.76	53
	K	675	105	0.32 × 0.25	43	743	102	0.31 × 0.26	53
J1814+228	X	77	53	0.96 × 0.80	129	72	58	1.00 × 0.74	120
	U	168	17	0.55 × 0.44	135	171	17	0.51 × 0.39	118
J1924+286	X	74	108	0.87 × 0.82	99	71	122	0.89 × 0.77	107
	U	195	44	0.48 × 0.46	175	181	51	0.46 × 0.41	99
J1956+635	X	90	158	1.07 × 0.74	117	87	164	1.00 × 0.73	113
	U	192	64	0.53 × 0.42	112	201	60	0.47 × 0.39	109
J2055+613	X	99	740	1.01 × 0.73	81	164	448	0.98 × 0.73	86
	K	512	124	0.35 × 0.26	72	691	97	0.34 × 0.26	84
J2115+367	X	88	238	1.02 × 0.79	93	92	184	1.03 × 0.74	104
	U	211	116	0.52 × 0.46	97	233	104	0.52 × 0.39	101
J2145+187	X	96	173	1.01 × 0.82	126	72	243	0.97 × 0.78	122
	U	182	94	0.53 × 0.45	145	198	84	0.50 × 0.41	118
J2202+292	X	82	122	0.90 × 0.82	95	70	143	0.91 × 0.76	108
	U	175	30	0.47 × 0.46	152	183	28	0.47 × 0.41	98
J2208+615	X	82	121	1.08 × 0.72	94	85	111	1.01 × 0.73	92
	U	188	33	0.55 × 0.42	84	189	32	0.53 × 0.38	95

Table 6.1: Image quality information for sources observed with the VLA. Achieved noise levels, five sigma dynamic range, and restoring beam parameters are listed for both observing bands and epochs.

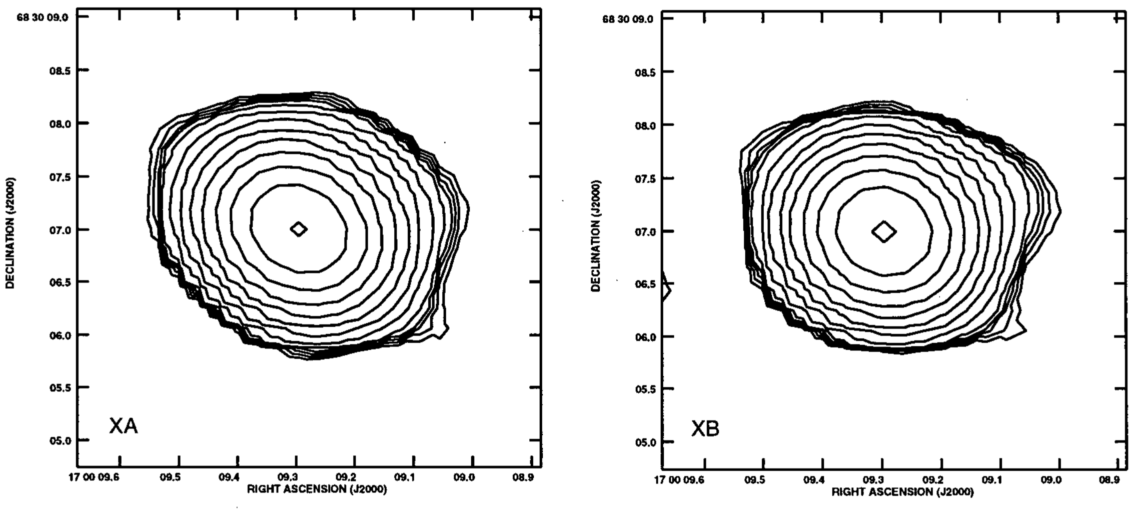

Figure 6.7: VLA images of J1700+685 at X band during epoch A and B as labeled. Contour levels are 3, 4, 5, 6, 8, 16, 32, 64, 128, 256, 512, 1024, 2048 times the noise level.

6.1.1 Two-Sided Sources

There are four sources, J0049+343, J1307+064, J0532+562 and J1630+741, which have distinct, two-sided structure, and appear to be typical radio galaxies. With the exception of J0049+343, all sources posses a strong central region; however only the core of J0532+562 has a self absorbed flat spectrum, possibly indicating that the steep spectrum central regions of J1630+741 and J1307+064 are not sufficiently resolved and contain significant extended emission. The central region of J0049+343, noticeably absent, may be obscured by a parent galaxy.

Two prominent jets are apparent in J0049+343 at X band, with the stronger jet, to the north, also apparent at U band, having a flat spectrum. Both J0532+562 and J1630+741 show evidence for a single jet to the northwest and northeast respectively. The jet of J0532+562 is not visible at U band, whereas the jet of J1630+741 is more clearly resolved at U band, although not fully separated from the steep spectrum extended

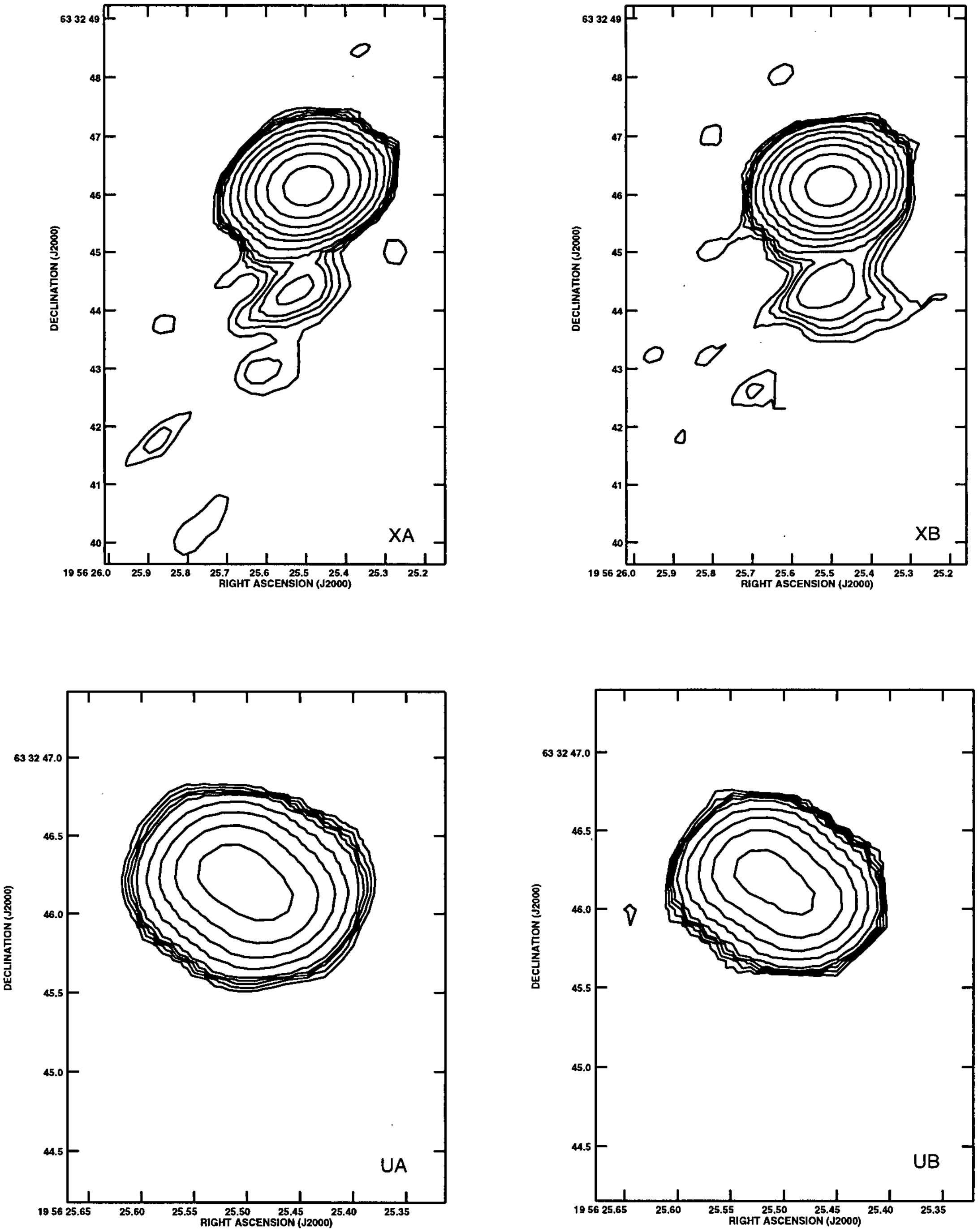

Figure 6.8: VLA images of J1956+635 at X and U band during epoch A and B as labeled. Contour levels are 3, 4, 5, 6, 8, 16, 32, 64, 128, 256, 512 times the noise level.

J0049+343

COMPONENT		F_{XA} (mJy)	F_{XB} (mJy)	F_{UA} (mJy)	F_{UB} (mJy)	α_A	α_B	V_X	V_U	$\delta R.A.$ $(asec)$	$\delta Dec.$ $(asec)$
a		3.0	3.0	2.7	3.2	0.22	-0.13	0.005	0.096	0.000	0.000
	±	0.4	0.3	0.7	0.7	0.52	0.41	0.086	0.164	0.027	0.020
Extended		90.7	88.5	10.1	29.9	3.86	1.91	0.013	0.496		
	±	2.8	3.1	6.1	6.4	1.06	0.38	0.023	0.252		
Total		93.8	91.5	12.8	33.2	3.51	1.78	0.012	0.444		
	±	2.7	3.1	6.1	6.4	0.84	0.34	0.022	0.214		

J0532+562

COMPONENT		F_{XA} (mJy)	F_{XB} (mJy)	F_{UA} (mJy)	F_{UB} (mJy)	α_A	α_B	V_X	V_U	$\delta R.A.$ $(asec)$	$\delta Dec.$ $(asec)$
a		103.3	96.5	110.8	104.2	-0.12	-0.14	0.034	0.030	0.000	0.000
	±	0.3	0.3	0.6	0.8	0.01	0.01	0.002	0.005	0.007	0.006
b		5.2	4.8	2.4	2.3	1.37	1.26	0.042	0.011	-3.990	7.485
	±	0.4	0.4	0.8	1.0	0.57	0.80	0.053	0.273	0.022	0.012
c		2.2	1.8	0.0	0.0			0.099		-0.625	1.064
	±	0.3	0.4	0.9	1.1			0.138		0.044	0.037
Extended		5.8	7.8	0.0	0.0			0.146			
	±	1.4	1.8	3.1	4.2			0.179			
Total		116.4	110.8	113.1	106.6	0.05	0.07	0.025	0.030		
	±	1.3	1.7	1.2	1.3	0.03	0.03	0.009	0.008		

J1307+064

COMPONENT		F_{XA} (mJy)	F_{XB} (mJy)	F_{UA} (mJy)	F_{UB} (mJy)	α_A	α_B	V_X	V_U	$\delta R.A.$ $(asec)$	$\delta Dec.$ $(asec)$
a		52.4	52.2	23.9	23.5	1.38	1.40	0.001	0.008	0.000	0.000
	±	0.4	0.4	0.9	0.9	0.07	0.06	0.005	0.026	0.001	0.008
b		37.9	38.0	19.7	20.5	1.15	1.08	0.001	0.021	-13.383	5.447
	±	0.5	0.5	1.8	1.8	0.16	0.15	0.010	0.063	0.013	0.005
c		2.8	2.7	1.5	1.6	1.14	0.91	0.007	0.058	-8.010	2.793
	±	0.4	0.3	0.6	0.6	0.78	0.72	0.089	0.288	0.016	0.017
Extended		14.2	11.0	9.2	9.6	0.77	0.24	0.129	0.021		
	±	2.5	2.3	6.4	6.8	1.26	1.29	0.137	0.494		
Total		107.3	103.9	54.2	55.3	1.20	1.11	0.016	0.009		
	±	2.4	2.2	6.1	6.4	0.20	0.21	0.015	0.081		

J1630+741

COMPONENT		F_{XA} (mJy)	F_{XB} (mJy)	F_{UA} (mJy)	F_{UB} (mJy)	α_A	α_B	V_X	V_U	$\delta R.A.$ $(asec)$	$\delta Dec.$ $(asec)$
a		35.3	34.7	19.2	18.7	1.07	1.09	0.009	0.016	0.000	0.000
	±	0.4	0.4	0.8	0.7	0.08	0.07	0.008	0.028	0.013	0.010
Extended		45.9	41.3	21.8	20.8	1.31	1.20	0.053	0.022		
	±	2.0	1.9	3.6	3.8	0.30	0.33	0.032	0.123		
Total		81.2	75.9	41.0	39.5	1.20	1.15	0.033	0.019		
	±	1.9	1.9	3.5	3.7	0.16	0.17	0.017	0.064		

Table 6.2: Measured parameters of two-sided resolved sources, including flux density, F_{ij}, spectral index, α_j, and variability index, V_i, at i band during epoch j, as well as relative positions, for source components.

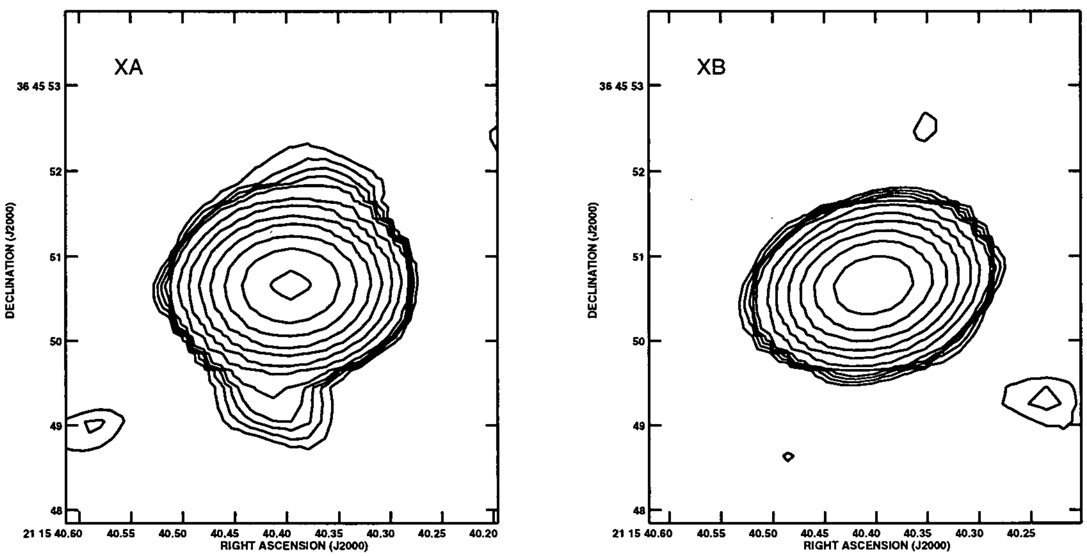

Figure 6.9: VLA images of J2115+367 at X band during epoch A and B as labeled. Contour levels are 3, 4, 5, 6, 8, 16, 32, 64, 128, 256, 512, 1024 times the noise level.

emission. There is no evidence for a jet emanating from the core at either X or U band in J1307+064.

All four sources have two obvious radio lobes at X band, whereas only J1307+064 has both lobes, and J0532+562 has one lobe, apparent at U band. In all cases, these lobes are steep spectrum, with one lobe being noticeably brighter than the other. The X band radio lobes of J1630+741 differ from one another. The inner part of the lobe to the southeast, correlated to the jet like structure obvious at U band, is compact and bright near the core, but the lobe becomes very tenuous as it curves further south. The lobe to the west of the core does not have an analogous compact feature near the core at either X or U band, but the lobe is much larger and brighter than the outer region of the southern lobe, and actually has a peak in the the flux at the western edge of the lobe, far from the core. The radio lobes of J0049+343 and J1630+741 are relatively detailed, compared to the compact lobes of J1307+064 and J0532+562, implying either intrinsically larger

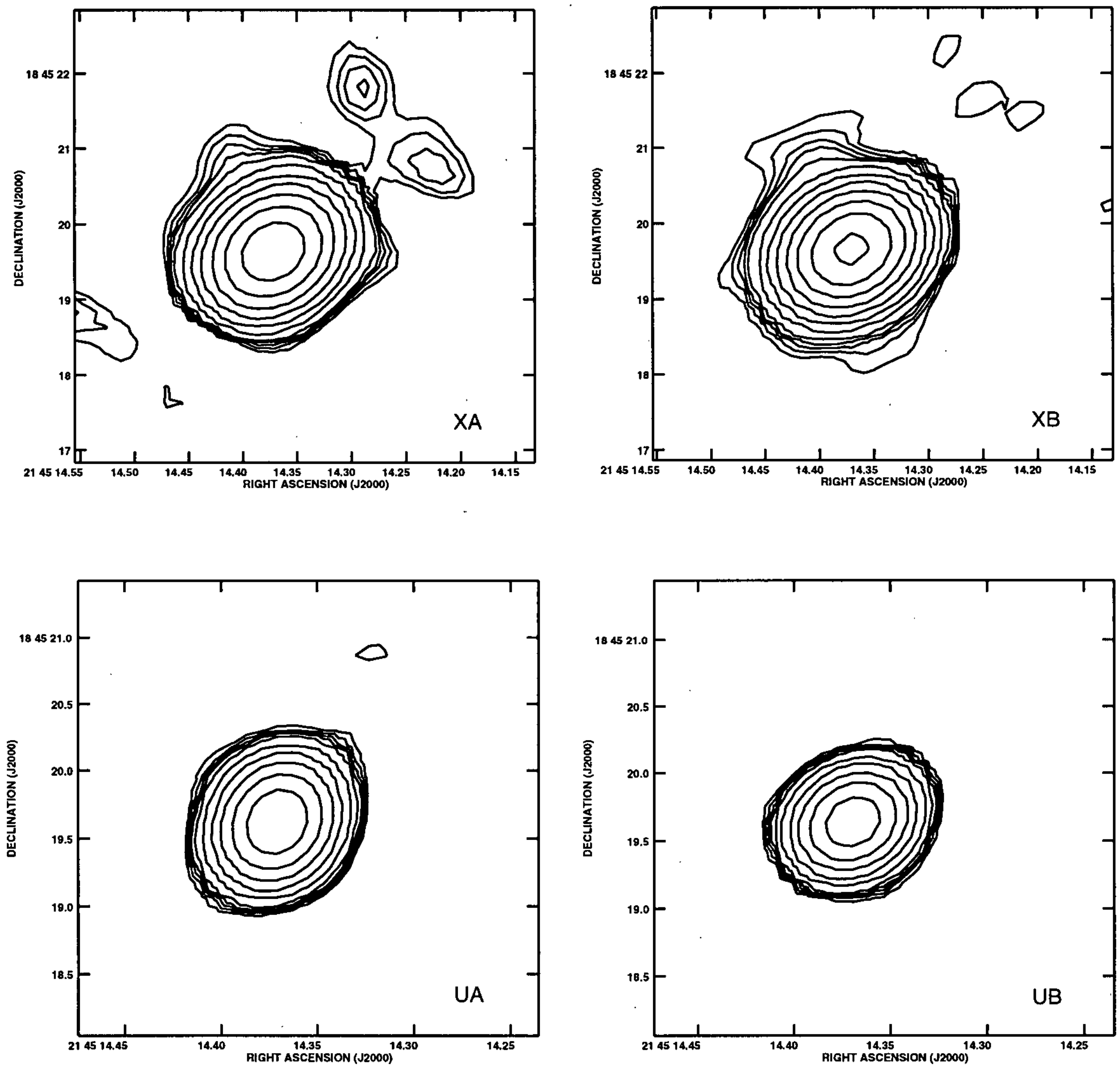

Figure 6.10: VLA images of J2145+187 at X and U band during epoch A and B as labeled. Contour levels are 3, 4; 5, 6, 8, 16, 32, 64, 128, 256, 512, 1024 times the noise level.

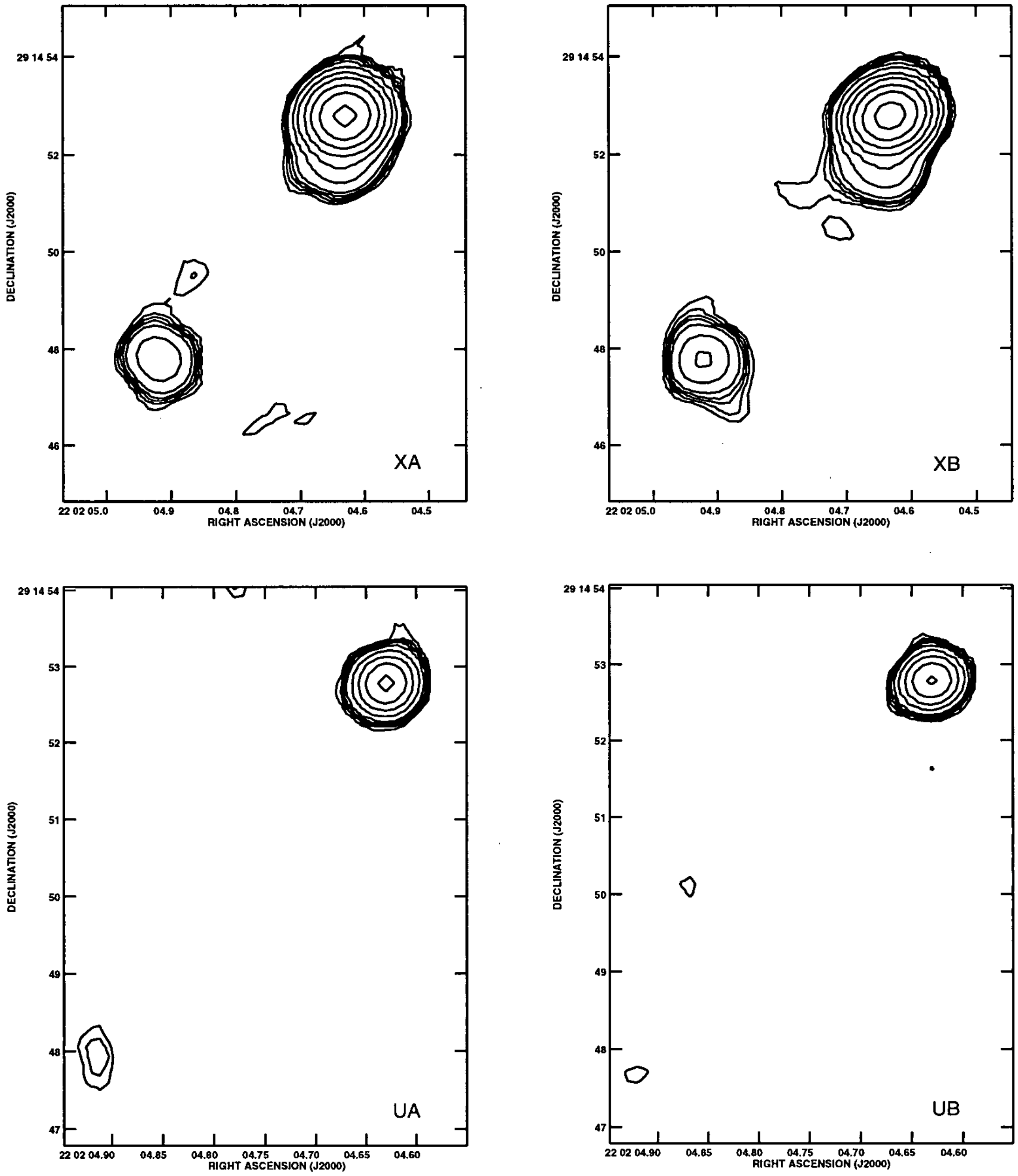

Figure 6.11: VLA images of J2202+292 at X and U band during epoch A and B as labeled. Contour levels are 3, 4, 5, 6, 8, 16, 32, 64, 128, 256, 512 times the noise level.

lobes for the former pair of sources, or greater distance for the latter pair.

The overall structure of J1307+064 is linear, whereas for both J0049+343 and J0532+562 the radio lobes are slightly out of alignment from the central region, and in contrast, the structure of J1630+741 is extremely non-symmetric. These structural asymmetries may be the result of motion of the central galaxy or precession of the jet. In all four cases there is no significant flux density variations or spectral index changes observed. Significant flux density variation is defined here as a variability index, $V > 0.1$ at a ≥ 5 sigma confidence level, a moderate flux density variation is defined by a variability index between 0.10 and 0.05 also at a ≥ 5 sigma confidence level, and a significant spectral index change is one detected at a ≥ 3 sigma level.

6.1.2 One-Sided Sources

Three of the 24 sources imaged with the VLA, at X band, exhibit one-sided structure associated with the central region, including a single radio lobe, and some evidence for a jet. Both J1956+635 and J2202+292 are strongly dominated by the central region, with the lobes representing only a small fraction of the total flux. Both the central region and the lobe of J0903+636 are extremely weak and the lobes of all three sources are of the order of 5 mJy. J2202+292 has an obvious extension from the core towards the lobe, and J0903+636 includes some residuals between the core and the lobe that may represent knots of the jet. The apparent proximity of the lobes to the core in J1956+635 obscures any sign of a jet. At U band, only a central core is visible in J0903+636 and J2202+292, both having a steep spectrum, which again may indicate inclusion of extended emission in the central feature.

Although no radio lobe of J1956+635 is observed at U band, the central region is now clearly resolved into two flat spectrum components, perhaps a true core and an approaching jet, or both an approaching and receding jet. Since the central region is

J0903+636

COMPONENT		F_{XA} (mJy)	F_{XB} (mJy)	F_{UA} (mJy)	F_{UB} (mJy)	α_A	α_B	V_X	V_U	$\delta R.A.$ $(asec)$	$\delta Dec.$ $(asec)$
a		4.3	4.5	1.5	1.1	1.81	2.41	0.018	0.152	0.000	0.000
	±	0.3	0.3	0.9	0.8	1.00	1.27	0.052	0.454	0.019	0.014
Extended		5.1	5.2	0.0	0.0			0.004			
	±	0.7	0.8	1.3	1.6			0.102			
Total		9.5	9.7	1.5	1.1	3.18	3.76	0.010	0.152		
	±	0.6	0.7	0.9	0.8	0.99	1.27	0.049	0.454		

J1956+635

COMPONENT		F_{XA} (mJy)	F_{XB} (mJy)	F_{UA} (mJy)	F_{UB} (mJy)	α_A	α_B	V_X	V_U	$\delta R.A.$ $(asec)$	$\delta Dec.$ $(asec)$
a_U		37.0	37.9	27.7	26.9	0.51	0.60	0.013	0.014	0.000	0.000
	±	0.2	0.2	0.7	0.7	0.05	0.05	0.004	0.018	0.007	0.010
b_U		46.2	47.4	34.3	33.9	0.52	0.59	0.013	0.005	0.291	0.237
	±	0.2	0.2	0.7	0.7	0.04	0.04	0.004	0.014	0.012	0.012
c_X		83.2	85.4	62.0	60.9	0.52	0.59	0.013	0.009	0.123	0.104
	±	0.3	0.3	0.9	1.0	0.03	0.03	0.003	0.011	0.020	0.001
Extended		4.8	5.1	0.0	0.0			0.031			
	±	1.1	1.1	2.2	2.3			0.161			
Total		88.0	90.5	62.0	60.9	0.62	0.70	0.014	0.009		
	±	1.1	1.1	0.9	1.0	0.03	0.04	0.009	0.011		

J2202+292

COMPONENT		F_{XA} (mJy)	F_{XB} (mJy)	F_{UA} (mJy)	F_{UB} (mJy)	α_A	α_B	V_X	V_U	$\delta R.A.$ $(asec)$	$\delta Dec.$ $(asec)$
a		51.2	51.3	26.8	26.5	1.14	1.16	0.001	0.007	0.000	0.000
	±	0.3	0.2	0.6	0.6	0.04	0.04	0.004	0.017	0.006	0.002
b		3.4	3.8	1.5	0.9	1.43	2.51	0.046	0.256	0.152	-0.971
	±	0.3	0.3	0.6	0.7	0.71	1.43	0.067	0.380	0.020	0.016
c		3.1	3.4	0.0	0.0			0.050		3.774	-4.993
	±	0.3	0.3	0.9	0.9			0.068		0.016	0.017
Extended		2.1	1.7	5.7	0.5	-1.79	2.16	0.095	0.839		
	±	1.2	1.1	2.2	2.8	1.21	9.84	0.426	0.668		
Total		59.8	60.1	34.1	27.9	0.99	1.35	0.003	0.100		
	±	1.0	1.0	2.1	2.6	0.11	0.17	0.012	0.053		

Table 6.3: Measured parameters of one-sided resolved sources, including flux density, F_{ij}, spectral index, α_j, and variability index, V_i, at i band during epoch j, as well as relative positions, for source components.

resolved into two components at U band and not at X band, only the components specified by a band subscript in table 6.3 are real. For analysis purposes, the X band central component has been artificially divided, in proportion to the U band component pair, and an artificial U band single component is the sum of the real U band pair.

It is tempting to interpret these three sources as either more distant or intrinsically weaker examples of two-sided sources, owing to the relatively faint observed radio lobe, for which the differential relativistic doppler brightening has conspired to boost only one side of the structure above the sensitivity threshold. Like the previous two-sided objects, the one-sided objects do not show any significant flux density variations or any certain change in spectral index.

6.2 Partially Resolved Sources

Four of the resolved sources, J0259+516, J2145+187, J2115+367 and J1700+685, do not clearly fall into either of the preceding categories, and elude interpretation. All of these sources exhibit some structure, which appears to be different in both epochs, and all show approximately at least a three sigma change in spectral index. Both J1700+685 and J2115+367 are significantly variable at X band, J0259+516 is moderately variable at X band, and J2145+187 does not show significant flux density variation at either band. Of the four sources, the most intriguing is J1700+685[1], which consists of a bright core and a second component to the west-northwest of the core. Both components brighten during epoch B, but since the second component is within the central beam of the core, interpretation is difficult. Due to the ambiguous and changing structure, observed flux density variations, and interesting spectral index changes, all four of these sources deserve to be imaged by the VLA in A configuration and perhaps require higher resolution

[1] An optical spectrum taken in August, 1997 with the CHFT places J1700+685 at a redshift of $z \sim 0.3$, with prominent emission lines and absorption features commensurate with a quasar.

VLBA/VLBI imaging and optical wavelength study.

6.3 Unresolved Sources

Half of the sources imaged with the VLA were unresolved at both observed bands. The flux density measurements, as well as the spectral index and variability information for these sources is summarized in table 6.5.

The majority of the 12 sources shows no significant flux density variation, and only J0502+346 shows significant variation at both bands, while both J0251+562 and J0611+723 show significant variation only at K and U bands respectively. Moderate variation at X band occurs in J0856+717 and J0611+723, while moderate variation occurs at U band for J0502+388.

The spectra of most of the sources is flat ($-0.5 \leq \alpha \leq 0.5$) but J2208+615 and J1814+228 have steep spectra ($\alpha > 0.5$) whereas J0856+717 has an inverted spectrum ($\alpha < -0.5$). Eight of the twelve sources exhibit a change in spectral index at the three sigma level or higher.

6.4 *APS* and *DSS* Optical Counterparts

With substantially more accurate positions for all VLA imaged sources, it is possible to convincingly associate optical counterparts. The digitized *DSS* POSS I plates were checked for optical counterparts within five arcseconds of the VLA derived radio positions. The matching of sources is limited by the positional accuracy of the plates, which have not been calibrated. Table 6.6 contains an approximate separation between radio and optical positions and qualitative description of optical counterpart quality and *DSS* image noise level.

J0259+516

COMPONENT		F_{XA} (mJy)	F_{XB} (mJy)	F_{UA} (mJy)	F_{UB} (mJy)	α_A	α_B	V_X	V_U	$\delta R.A.$ $(asec)$	$\delta Dec.$ $(asec)$
a		71.2	61.7	66.5	61.0	0.12	0.02	0.071	0.043	0.000	0.000
	±	0.3	0.3	0.7	0.7	0.02	0.02	0.003	0.008	0.009	0.003
b		1.5	2.0	0.0	0.0			0.128		-0.375	0.854
	±	0.4	0.5	1.0	1.0			0.193		0.179	0.105
Total		72.7	63.7	66.5	61.0	0.16	0.08	0.066	0.043		
	±	0.5	0.6	0.7	0.7	0.02	0.03	0.006	0.008		

J1700+685

COMPONENT		F_{XA} (mJy)	F_{XB} (mJy)	F_{KA} (mJy)	F_{KB} (mJy)	α_A	α_B	V_X	V_K	$\delta R.A.$ $(asec)$	$\delta Dec.$ $(asec)$
a		223.6	269.1	361.8	386.5	-0.49	-0.37	0.092	0.033	0.000	0.000
	±	0.4	0.4	2.4	2.6	0.01	0.01	0.001	0.005	0.002	0.004
b		3.9	17.0	0.0	0.0			0.624		-0.263	0.210
	±	0.3	0.6	3.3	3.7			0.043		0.146	0.066
Total		227.5	286.0	361.8	386.5	-0.47	-0.31	0.114	0.033		
	±	0.7	0.8	5.3	5.8	0.02	0.02	0.002	0.011		

J2115+367

COMPONENT		F_{XA} (mJy)	F_{XB} (mJy)	F_{UA} (mJy)	F_{UB} (mJy)	α_A	α_B	V_X	V_U	$\delta R.A.$ $(asec)$	$\delta Dec.$ $(asec)$
a		105.4	83.8	121.5	119.2	-0.25	-0.62	0.114	0.009	0.000	0.000
	±	0.3	0.3	0.7	0.8	0.01	0.01	0.002	0.004	0.009	0.001
Extended		1.2	0.9	0.0	0.0			0.124			
	±	1.0	1.0	2.0	2.1			0.686			
Total		106.6	84.8	121.5	119.2	-0.23	-0.60	0.114	0.009		
	±	0.9	1.0	0.7	0.8	0.02	0.02	0.007	0.004		

J2145+187

COMPONENT		F_{XA} (mJy)	F_{XB} (mJy)	F_{UA} (mJy)	F_{UB} (mJy)	α_A	α_B	V_X	V_U	$\delta R.A.$ $(asec)$	$\delta Dec.$ $(asec)$
a		85.1	88.2	86.5	82.9	-0.03	0.11	0.017	0.021	0.000	0.000
	±	0.3	0.2	0.6	0.7	0.01	0.02	0.002	0.006	0.002	0.004
Extended		3.2	3.8	1.4	1.2	1.44	1.98	0.091	0.061		
	±	0.7	0.5	1.5	1.7	1.96	2.41	0.125	0.860		
Total		88.3	92.0	87.9	84.1	0.01	0.16	0.020	0.022		
	±	0.6	0.5	1.4	1.5	0.03	0.03	0.004	0.012		

Table 6.4: Measured parameters of partially resolved sources, including flux density, F_{ij}, spectral index, α_j, and variability index, V_i, at i band during epoch j, as well as relative positions, for source components.

SOURCE	BANDS		F_{1A} (mJy)	F_{1B} (mJy)	F_{2A} (mJy)	F_{2B} (mJy)	α_A	α_B	V_1	V_2
J0048+684	XU		143.9	150.2	118.3	117.4	0.34	0.43	0.022	0.003
		±	0.7	0.4	0.7	0.7	0.01	0.01	0.003	0.004
J0251+562	XK		384.5	355.0	411.2	329.0	-0.07	0.08	0.040	0.111
		±	0.4	0.4	1.6	1.8	0.00	0.01	0.001	0.003
J0502+346	XU		211.9	159.4	256.9	165.2	-0.34	-0.06	0.141	0.217
		±	0.4	0.5	0.8	0.9	0.01	0.01	0.002	0.003
J0502+388	XU		229.1	213.2	252.8	211.8	-0.17	0.01	0.036	0.088
		±	1.2	0.3	0.8	1.1	0.01	0.01	0.003	0.003
J0611+723	XU		114.1	100.8	121.8	93.6	-0.12	0.13	0.062	0.131
		±	0.3	0.3	4.2	0.8	0.06	0.02	0.002	0.022
J0856+717	XU		120.0	141.1	188.7	188.5	-0.80	-0.51	0.081	0.001
		±	0.4	0.5	0.8	0.9	0.01	0.01	0.002	0.003
J1106+282	XK		293.2	289.0	256.0	269.6	0.14	0.07	0.007	0.026
		±	0.6	0.4	1.2	1.4	0.01	0.01	0.001	0.004
J1603+110	XK		448.3	458.0	446.0	449.4	0.01	0.02	0.011	0.004
		±	0.5	0.4	1.9	2.1	0.00	0.00	0.001	0.003
J1814+228	XU		20.8	20.7	14.4	15.0	0.65	0.56	0.002	0.022
		±	0.3	0.2	0.6	0.6	0.07	0.07	0.009	0.028
J1924+286	XU		40.3	43.2	42.5	46.9	-0.09	-0.14	0.035	0.049
		±	0.3	0.2	0.7	0.6	0.03	0.03	0.004	0.010
J2055+613	XK		364.6	367.8	317.2	336.7	0.14	0.09	0.004	0.030
		±	0.3	0.6	1.8	2.4	0.01	0.01	0.001	0.005
J2208+615	XU		49.6	47.5	31.2	30.4	0.81	0.79	0.021	0.014
		±	0.3	0.3	0.6	0.6	0.04	0.04	0.004	0.015

Table 6.5: Measured parameters of unresolved sources, including flux density F_{ij}, spectral index α_j, and variability index V_i, at the i^{th} band listed in the second column of the table, during epoch j.

The automated plate scanner (*APS*) is a project undertaken by the University of Minnesota to catalog objects on the digitized POSS I plates, and the current data has been made available. The *APS* project is attempting to classify, provide calibrated positions, and measure magnitude and colour for every object on the POSS I plates. To date, only a fraction of the work has been completed, but three of the VLA imaged radio sources have *APS* optical counterparts within three arcseconds. The *APS* derived parameters for these three radio sources are given in table 6.7. A more complete description of the *APS* project and the *DSS* plates can be found in section 4.2.3.

6.5 Conclusion

The project goal of taking high resolution multi-epoch, multi-frequency VLA images of the 24 selected GB6 short term radio variables was achieved, with no major problems occurring during observations and resulting image quality parameter values (table 6.1)

SOURCE NAME	ΔPosition (*arcsec*)	Object Quality	Noise Level
J0048+684	1.8	faint	high
J0049+343	4.0	bright	low
J0251+562	2.2	bright	high
J0259+516		empty	low
J0502+346		empty	low
J0502+388		empty	low
J0532+562	1.4	faint	low
J0611+723		empty	medium
J0856+717	2.4	bright	medium
J0903+636		empty	high
J1106+282	1.4	faint	low
J1307+064		empty	medium
J1603+100	1.0	bright	low
J1630+741	3.4	moderate	medium
J1700+685	0.5	bright	low
J1814+228		empty	low
J1924+286	3.8	bright	medium
J1956+635	2.2	bright	low
J2055+613		empty	low
J2115+367		empty	low
J2145+187		empty	low
J2202+292		empty	medium
J2208+615	3.1	moderate	medium

Table 6.6: *DSS* optical counterparts of imaged radio sources. An approximate separation of measured radio and optical positions, as well as a qualitative description of object quality and noise level on the POSS I images is listed

SOURCE NAME	Class	Probability %	ΔPosition (*arcsec*)	APS Position (J2000)		Magnitude (O)	Color (O-E)
J0049+343	Galaxy	92	2.942	0:49:45.47	+34:22:35.90	21.42	3.20
J0856+717	Star	93	1.386	8:56:54.83	+71:46:22.52	19.65	0.52
J1700+685	Galaxy	80	0.540	17:00:09.36	+68:30:06.59	20.44	1.40

Table 6.7: *APS* determined parameter of *DSS* POSS I optical counterparts of imaged radio sources. Listed is the *APS* classification with associated probability, separation of radio and optical objects, calibrated position, magnitude, and colour.

SOURCE	BANDS		Position (J2000)		F_1 (mJy)	F_2 (mJy)	$\bar{\alpha}$	$\Delta\alpha$	$V_{\%}$	V_{σ}
J0048+684	XU		0:48:35.9811	+68:26:27.101	147.8	117.9	0.39	0.09	2.81	4.2
		±	0.0005	0.004	2.0	0.5	0.03	0.02	1.21	
J0049+343	XU		0:49:45.4711	+34:22:32.958	92.7	22.7	2.28	1.72	10.72	1.4
		±	0.0022	0.020	2.0	7.2	0.46	0.90	8.20	
J0251+562	XK		2:51:54.6283	+56:16:19.524	369.0	372.3	-0.01	0.15	10.80	42.9
		±	0.0019	0.001	10.4	28.9	0.05	0.01	2.70	
J0259+516	XU		2:59:38.3293	+51:38:13.831	68.6	63.7	0.12	0.08	11.27	8.7
		±	0.0010	0.003	3.2	1.9	0.03	0.03	1.56	
J0502+346	XU		5: 2:29.9397	+34:36:34.594	187.5	216.4	-0.24	0.28	33.24	80.9
		±	0.0007	0.008	18.4	31.8	0.09	0.01	4.56	
J0502+388	XU		5: 2:32.4871	+38:49:54.956	216.3	234.8	-0.07	0.18	12.43	21.3
		±	0.0009	0.007	3.0	14.2	0.06	0.01	3.56	
J0532+562	XU		5:32:59.6662	+56:12:22.661	114.0	109.9	0.06	0.02	5.46	3.1
		±	0.0009	0.006	1.9	2.3	0.02	0.04	1.23	
J0611+723	XU		6:11: 9.1686	+72:18:15.619	107.4	98.1	0.08	0.25	13.80	18.2
		±	0.0028	0.002	4.7	4.4	0.05	0.06	1.42	
J0856+717	XU		8:56:54.8691	+71:46:23.894	129.3	188.7	-0.67	0.29	9.56	18.1
		±	0.0007	0.003	7.3	0.6	0.10	0.01	5.50	
J0903+636	XU		9: 3:37.8855	+63:38:13.486	9.5	1.3	3.43	0.58	4.88	0.3
		±	0.0028	0.014	0.5	0.6	0.79	1.61	12.48	
J1106+282	XK		11: 6: 7.2549	+28:12:46.878	290.7	262.1	0.11	0.07	2.44	6.4
		±	0.0009	0.006	1.4	4.8	0.02	0.01	0.95	
J1307+064	XU		13: 7: 6.8510	+ 6:27:46.754	105.5	54.7	1.15	0.09	3.02	0.6
		±	0.0001	0.008	1.6	4.4	0.14	0.29	3.65	
J1603+110	XK		16: 3:41.9311	+11: 5:48.652	453.2	447.6	0.01	0.01	1.88	8.1
		±	0.0008	0.003	3.4	1.4	0.00	0.01	0.24	
J1630+741	XU		16:30:26.8746	+74: 9:33.509	78.5	40.3	1.18	0.05	6.07	1.1
		±	0.0031	0.010	1.9	2.6	0.12	0.23	3.81	
J1700+685	XK		17: 0: 9.2950	+68:30: 6.992	255.2	373.6	-0.39	0.17	20.21	29.1
		±	0.0003	0.004	20.6	8.7	0.06	0.02	2.66	
J1814+228	XU		18:14: 3.0625	+22:48:54.105	20.7	14.7	0.60	0.09	1.36	0.5
		±	0.0001	0.013	0.2	0.4	0.05	0.10	1.91	
J1924+286	XU		19:24:15.6283	+28:37:52.576	41.8	44.8	-0.12	0.05	7.90	6.5
		±	0.0001	0.001	1.0	1.6	0.02	0.04	0.86	
J1956+635	XU		19:56:25.4795	+63:32:46.044	89.2	61.4	0.66	0.08	2.38	1.2
		±	0.0010	0.010	0.9	0.7	0.03	0.05	1.37	
J2055+613	XK		20:55:38.8354	+61:22: 0.616	365.8	325.5	0.12	0.05	1.72	5.7
		±	0.0005	0.004	1.0	6.7	0.02	0.01	0.83	
J2115+367	XU		21:15:40.3978	+36:45:50.658	95.9	120.4	-0.39	0.37	9.95	9.1
		±	0.0008	0.001	7.7	0.8	0.13	0.03	6.84	
J2145+187	XU		21:45:14.3708	+18:45:19.643	90.4	86.1	0.08	0.15	4.13	3.2
		±	0.0001	0.004	1.3	1.3	0.05	0.05	0.90	
J2202+292	XU		22: 2: 4.6331	+29:14:52.794	60.0	31.3	1.13	0.37	4.10	1.1
		±	0.0005	0.002	0.7	2.2	0.12	0.20	3.40	
J2208+615	XU		22: 8:11.9139	+61:32:56.441	48.6	30.8	0.80	0.02	3.93	3.0
		±	0.0011	0.008	0.7	0.5	0.03	0.05	0.93	

Table 6.8: Summary of characteristic parameters for VLA imaged radio sources. Weighted average of brightest source component position is listed, along with weighted average of total flux, F_i, at the i^{th} band. Also listed are the characteristic spectral index, change in spectral index, variability expressed as a percentage (eqn. 1.2), and variability confidence level (eqn. 1.4).

obtained as planned. In particular, a resolution of the order of $1''$ at X band and $< 1''$ for U or K band, slightly larger than the ideal values in table 5.1, were achieved as expected. Although U or K band observations were necessary to derive spectral indices, they were not as useful as originally hoped in elucidating source structure, compared to X band. It was thought that the improved resolution at U or K band would offset the loss of sensitivity and increase in VLA system noise at U or K band with respect to X band, and maintain importance for structure determination. Generally, this was not the case, especially for steep spectrum extended structure, and it is suggested that future similar VLA based variability studies rely primarily on X band observations, and use U or K band observations only for sources for which it is necessary.

Of the 24 radio sources imaged at X band four had distinct two-sided structure and three had one-sided structure, none of which exhibited significant variability in structure, flux density variation, or change in spectral index, and all of which are almost certainly regular radio-loud AGN. Four sources were partially resolved, showing some level of variability in both structure and flux density as well as changes in spectral index. The evidence for short term structural changes suggests these may be galactic jet sources. It would be desirable to confirm the structural variations with higher resolution observations. Twelve sources were completely unresolved, five of which exhibit some variability and eight of which exhibit a notable change in spectral index. From the *APS* results one of these unresolved sources appears likely to be stellar. The moderate to low levels of flux density variation seen in the partially resolved and specifically the unresolved sources may be attributable, at least in part, to RISS. Although the unresolved sources are most likely to be extremely distant blazars, with the intrinsic core variability enhanced by relativistic doppler effects, if they are indeed extragalactic point-like sources, as opposed to flaring radio stars, they will be susceptible to RISS, and RISS may account for a fraction of the observed variability. One of the 24 short term variable sources studied did not appear at all in the observed VLA image field.

To interpret the correlation of variability results from this VLA study with the measured GB6 short term variability, one must consider effects of statistical sampling. Random time sampling of a flux density distribution will usually result in an underestimation of the true variability level, especially for small samples, as in the VLA study. However, due to the selection process, the observed GB6 variability levels, of the 24 chosen sources, are biased towards true variability levels and levels artificially enhanced by chance as a consequence of flux density uncertainties. Even in the context of statistical sampling, the VLA determined low variability level may still perhaps be inconsistent with the higher GB6 short term variability, particularly for the one-sided and two-sided AGN; a Monte Carlo simulation could settle this question. It is difficult to speculate as to the reason for the discrepancy, if in fact it exists, but the high $\hat{Q}$ values, especially for the mentioned sources, may be indicative of rare core flaring events, or perhaps the uncertainties in the daily flux density measurements provided [2] are underestimated and may be affected by sporadic, unaccounted noise.

A summary of averaged VLA measured parameters for observed sources is given in table 6.8. The VLA measured source flux densities, as projected to longer wavelengths using VLA spectral indices, for the majority of sources, are consistent with GB6 long term epoch flux density measurements. Both epoch VLA flux density measurements, for three sources, J0048+684, J0049+343, and J0502+346, fall just above maximum GB6 daily flux data, and two sources, J0856+717 and J1700+685 lie just below GB6 daily flux minima. The observed GB6 daily flux variation levels in all five of these sources convincingly suggest the above VLA flux density data are plausible, and are not considered a discrepancy.

The structural ambiguity of the partially and unresolved sources may be removed with

VLA A configuration snapshots, with the slightly higher resolution perhaps making identification possible. Of the unresolved sources, three are intriguing based on observed variability, with J0251+562 being significantly variable at K band, J0611+723 significantly variable at U band and moderately variable at X band, and J0502+346 being significantly variable at both X and U band. The observed level of variability in these sources is most likely dominantly intrinsic and should be monitored with multi-epoch VLA flux density measurements, particularly J0502+346, which is the most interesting unresolved source. Three partially resolved sources J1700+865, J2145+187 and J2115+367 exhibit some structural variation with both J1700+685 and J2115+367 also varying in flux density at X band. All three of these partially resolved sources warrant further attention with high resolution multi-epoch observations using the VLA in A configuration or VLBA/VLBI. After further high resolution radio imaging, perhaps optical wavelength observations and spectral analysis may be useful to provide distance estimates and assist classification.

As a whole the adopted source selection process and observation strategies are believed to be a success, but with the benefit of hindsight and daily flux data currently being extracted for the entire GB6 catalog, some improvements are possible for future short term variability studies. From the complete set of GB6 daily flux measurements one may be able to determine, for each source, not only a characteristic short term variability index, but also a characteristic, or most significant time scale, from the time scale distribution of variability indices. Due to time constraints, including those imposed by the VLA proposal deadlines, and a limited subset of short term variability information, improved source selection criteria, based on statistical analysis of above characteristic parameters, were not explored. An augmented sample of short term variables would allow concentrated focus on sources exhibiting significant short term variability index, at a high confidence level, during both epochs. Furthermore, with the eventual completion of the *NVSS*, *FIRST*, *APS*, and other databases, the information provided should be incorporated into the short term variable selection process.

Bibliography

[1] Gregory, P.C., Scott, W.K., Douglas, K.,& Condon, J.J., "The GB6 Catalog of Radio Sources", *Astrophysical Journal Supplement* **103**: 427 (1996)

[2] Scott, William K., *"Compact Radio Source Variability at Centimeter Wavelengths"*, Ph.D. Thesis, University of British Columbia (1996)

[3] Mirabel, I.F, &, Rodriguez, L.F "Superluminal Motions in our Galaxy", *Invited Review at the 17th Texas Symposium on Relativistic Astrophysics*; Münich, Germany (Decenber 1994)

[4] Hjellming, R.M., & Rupen, M.P. "Episodic ejection of relativistic jets by the X-ray transient GRO J1655-40", *Nature* **375**: 464-468 (June 1995)

[5] Vermeulen, R.C., Schlizzi, R.T., Spencer, R.E, Romney, J.D., & Fejes, I. "A series of VLBI images of SS433 during the outbursts in May/June 1987", *Astronomy and Astrophysics* **207**: 177-188 (1993)

[6] Rickett, B.J. "Refractive Interstelar Scintillation of Radio Sources", *The Astrophysical Journal* **307**: 564-574 (1986)

[7] Rickett, B.J., Quirrenbach, A., Wegner, R., Krichbaum, T.P., & Witzel, A. "Interstellar Scintillation of Radio Source 0917+624", *Astronomy and Astrophysics* **293**: 479-492(1995)

[8] Perley, R.A. *"Very Large Array Observational Status Summary"*, NRAO Publication (1996)

[9] Staff of NRAO; Hjellming R.M. (ed.) *"An introduction to the NRAO Very Large Array, Edition 2.0"*, NRAO Publication (1992)

[10] Perley, R.A. & Taylor, G.B. *"The VLA Calibrator Manual"*, NRAO Publication (1996)

[11] Perley, R.A., Schwab, F.R. & Bridle, A.H. (eds.) *"Synthesis Imaging"* Course Notes from an NRAO Summer School Held in Socorro, New Mexico, Aug 5-9, 1985; NRAO Publication (1986)

[12a] Verschuur, G.L. & Kellermann, K.I. (eds.) *"Galactic and Extragalactic Radio Astronomy"*, Springer-Verlag (1974) Hjellming, R.M. *"Chapter 7: Radio Stars"* (159-178)

[12b] Verschuur, G.L. & Kellermann, K.I. (eds.) *"Galactic and Extragalactic Radio Astronomy"*, Springer-Verlag (1974) Kellermann, K.I. *"Chapter 12: Radio Galaxies and Quasars"* (320-352)

[13] Roland, H.S. & Pelletier, G. (eds.) *"Extragalactic Radio Sources - From Beams to Jets"*, Cambridge University Press (1991)

[14] Zensus, J.A. & Pearson, T.J. (eds.) *"Superluminal Radio Sources"*, Cambridge University Press (1986)

[15] Hey, J.S. *"The Radio Universe, 3rd Edition"*, Pergamon Press (1983)

[16] Davis, R.J., & Booth, R.S. (eds.) *"Sub-arcsecond Radio Astronomy"*, Cambridge University Press (1992)

[17] Urry, C.M. & Padovani, P. "Unification Schemes for Radio-Loud Active Galactic Nuclei", *Publications of the Astronomical Society of the Pacific*, Invited Review Paper, **107**: 803-845, (1995)

[18] Bridle, A.H., Clarke, D.A., Burns, J.O., Perley, R.A., & Norman, M.L. "Origin of the structures and polarization in the classical double 3C219", *The Astronomical Journal*, **385**: 173-187 (1992)

[19] Zeilik, M., & Gaustad, J., *"Astronomy: The Cosmic Perspective, 2nd Edition"*, John Wiley & Sons Publishers (1983)

[20] Kaufmann, William J. III, & Comins, Neil F., *"Discovering the Universe, 4th Edition"*, W. H. Freeman and Company Publishers (1996)

Appendix A

Short Term Variable Tables

A.1 Short Term Variable Positions

NAME	J2000 Position		±	Catalog	Galactic	
J0003+249	0: 3:18.4	+24:59:40	12	GB6	-36.6	109.3
J0005+544	0: 5: 5.8	+54:28:36	9	GB6	-7.8	116.2
J0019+734	0:19:45.2	+73:27:27	6	GB6	10.7	120.6
J0036+185	0:36:59.34	+18:32: 3.3	0.4	NVSS	-44.2	118.2
J0039+411	0:39:54.9	+41:11:41	19	GB6	-21.6	120.6
J0042+544	0:42: 5.5	+54:25:48	11	GB6	-8.4	121.6
J0047+569	0:47: 0.0	+56:57:51	8	GB6	-5.9	122.3
J0048+684	0:48:35.4	+68:26:29	9	GB6	5.6	122.7
J0049+343	0:49:45.7	+34:22:30	12	GB6	-28.5	122.5
J0120+265	1:20:57.3	+26:31:49	18	GB6	-35.9	131.1
J0121+118	1:21:40.7	+11:49:42	11	GB6	-50.4	134.6
J0128+490	1:28: 8.1	+49: 1:13	9	GB6	-13.4	129.1
J0202+397	2: 2: 1.6	+39:43:16	11	GB6	-21.2	137.4
J0228+673	2:28:50.2	+67:20:57	7	GB6	6.2	132.1
J0235+622	2:35:21.7	+62:16:17	11	GB6	1.8	134.7
J0249+511	2:49:22.7	+51: 8:16	10	GB6	-7.5	141.1
J0249+221	2:49: 9.41	+22: 8:12.3	0.4	NVSS	-33.1	155.8
J0251+562	2:51:54.53	+56:16:19.1	0.4	NVSS	-2.8	139.1
J0259+516	2:59:38.23	+51:38:14.5	0.4	NVSS	-6.3	142.3
J0258+056	2:58:50.51	+ 5:41: 7.3	0.4	NVSS	-45.0	170.9
J0302+535	3: 2:23.4	+53:31:52	9	GB6	-4.5	141.7
J0304+683	3: 4:22.4	+68:21:46	7	GB6	8.6	134.7
J0310+391	3:10:25.0	+39:10:50	12	GB6	-16.2	150.3
J0310+382	3:10:49.6	+38:14:51	11	GB6	-16.9	150.9
J0323+462	3:23:57.2	+46:14:20	11	GB6	-8.9	148.5
J0325+349	3:25:20.3	+34:57:18	15	GB6	-18.0	155.4

NAME	J2000 Position		±	Catalog	Galactic	
J0325+224	3:25:36.81	+22:24: 1.0	0.4	NVSS	-28.0	163.7
J0326+287	3:26:34.9	+28:42:51	12	GB6	-22.9	159.5
J0332+545	3:32:59.25	+54:34:44.1	0.5	NVSS	-1.2	145.0
J0340+540	3:40: 6.53	+54: 5:37.7	0.5	NVSS	-1.0	146.1
J0350+516	3:50:24.98	+51:38:38.9	0.4	NVSS	-2.0	148.8
J0357+418	3:57:41.41	+41:48:46.1	0.4	NVSS	-8.7	156.1
J0411+087	4:11:33.84	+ 8:43:12.0	0.4	NVSS	-29.7	183.7
J0424+006	4:24:46.80	+ 0:36: 6.6	0.4	NVSS	-31.8	193.6
J0430+169	4:30:22.30	+16:55: 5.3	0.6	NVSS	-21.0	179.8
J0431+206	4:31: 3.75	+20:37:34.0	0.4	NVSS	-18.6	176.8
J0440+146	4:40:21.09	+14:37:57.1	0.4	NVSS	-20.5	183.2
J0444+251	4:44:58.12	+25: 9:36.2	0.5	NVSS	-13.2	175.3
J0445+072	4:45: 1.40	+ 7:15:53.5	0.4	NVSS	-23.9	190.5
J0449+635	4:49:23.34	+63:32: 8.8	0.4	NVSS	11.9	146.0
J0502+388	5: 2:32.46	+38:49:54.9	0.5	NVSS	-1.8	166.8
J0502+346	5: 2:29.88	+34:36:34.7	0.4	NVSS	-4.4	170.2
J0518+331	5:18: 5.23	+33: 6:12.5	0.4	NVSS	-2.7	173.3
J0530+550	5:30:16.73	+55: 2:48.5	0.4	NVSS	11.4	156.2
J0532+562	5:32:59.47	+56:12:24.8	0.4	NVSS	12.3	155.4
J0534+089	5:34: 8.40	+ 8:54:49.9	0.6	NVSS	-12.7	195.8
J0547+111	5:47:46.66	+11: 7:36.2	0.4	NVSS	-8.7	195.6
J0607+712	6: 7:19.2	+71:16: 7	7	GB6	22.2	142.8
J0606+146	6: 6:21.07	+14:36:17.3	0.4	NVSS	-3.1	194.8
J0611+723	6:11: 9.20	+72:18:16.3	0.5	NVSS	22.8	141.9
J0615+450	6:15:18.04	+45: 1:59.5	0.4	NVSS	12.9	168.7
J0629+044	6:29:56.23	+ 4:26:32.8	0.4	NVSS	-2.7	206.5
J0658+193	6:58:36.94	+19:19:15.9	0.7	NVSS	10.2	196.3
J0714+146	7:14: 4.67	+14:36:20.8	0.4	NVSS	11.5	202.3
J0716+367	7:16:37.10	+36:42:18.0	0.5	NVSS	20.5	181.2
J0722+181	7:22: 5.60	+18:11:17.8	0.6	NVSS	14.8	199.8
J0731+673	7:31:25.52	+67:18:47.3	0.5	NVSS	28.7	148.6

NAME	J2000 Position		±	Catalog	Galactic	
J0737+645	7:37:58.95	+64:30:43.3	0.4	NVSS	29.3	151.8
J0738+177	7:38: 7.35	+17:42:19.5	0.4	NVSS	18.1	201.8
J0751+272	7:51:41.46	+27:16:31.7	0.4	NVSS	24.5	193.5
J0815+619	8:15:39.26	+61:54:27.9	0.4	NVSS	33.6	154.8
J0839+033	8:39:49.16	+ 3:19:54.2	0.4	NVSS	25.5	222.9
J0849+098	8:49:41.11	+ 9:49:27.0	0.4	NVSS	30.7	217.6
J0856+717	8:56:54.60	+71:46:24.9	0.4	NVSS	35.3	142.0
J0903+636	9: 3:37.94	+63:38:11.8	0.4	NVSS	38.6	151.4
J0921+569	9:21: 7.43	+56:56:58.8	0.6	NVSS	42.6	159.0
J0927+572	9:27: 6.10	+57:17:44.7	0.4	NVSS	43.3	158.2
J0939+421	9:39: 6.69	+42: 7:18.3	0.4	NVSS	48.3	179.0
J0943+435	9:43: 9.05	+43:35:20.3	0.4	NVSS	48.9	176.7
J0944+520	9:44:52.13	+52: 2:33.8	0.4	NVSS	47.3	164.2
J0957+553	9:57:38.14	+55:22:57.3	0.4	NVSS	47.9	158.6
J0958+655	9:58:47.18	+65:33:54.2	0.4	NVSS	43.1	145.7
J1001+139	10: 1:40.1	+13:59:11	23	GB6	48.4	222.6
J1015+558	10:15:44.22	+55:51: 0.2	0.4	NVSS	50.0	156.2
J1016+052	10:16: 2.6	+ 5:13: 4	12	GB6	47.0	236.5
J1019+633	10:19:50.86	+63:20: 2.3	0.4	NVSS	46.3	146.4
J1031+746	10:31:22.31	+74:41:58.3	0.4	NVSS	39.2	134.2
J1030+515	10:30:35.15	+51:32:32.8	0.4	NVSS	54.0	160.6
J1037+571	10:37:44.24	+57:11:56.3	0.4	NVSS	51.8	151.8
J1048+717	10:48:27.55	+71:43:35.1	0.4	NVSS	42.3	135.4
J1103+720	11: 3:48.35	+72: 2:24.1	0.6	NVSS	42.7	133.9
J1106+282	11: 6: 7.22	+28:12:47.3	0.4	NVSS	66.7	204.1
J1106+172	11: 6:26.3	+17:13:30	12	GB6	63.8	229.7
J1112+350	11:12:33.18	+35: 3:39.6	0.5	NVSS	67.5	186.2
J1115+649	11:15:39.16	+64:59:31.6	0.4	NVSS	49.2	138.1
J1120+126	11:20:31.5	+12:41: 9	12	GB6	64.3	242.6
J1125+399	11:25:25.52	+39:59: 4.6	0.5	NVSS	68.0	171.6
J1127+568	11:27:40.16	+56:50:15.5	0.4	NVSS	56.8	143.8

NAME	J2000 Position		±	Catalog	Galactic	
J1153+251	11:53:18.09	+25: 9: 4.8	0.4	NVSS	76.8	218.3
J1157+077	11:57:12.9	+ 7:43:35	23	GB6	66.7	266.9
J1205+008	12: 5:47.9	+ 0:53:26	15	GB6	61.6	278.4
J1206+527	12: 6:23.5	+52:42:45	11	GB6	63.1	138.1
J1221+083	12:21:31.1	+ 8:21:30	28	GB6	69.9	280.9
J1222+042	12:22:21.4	+ 4:13:16	12	GB6	66.1	284.8
J1229+553	12:29: 9.22	+55:22:30.4	0.4	NVSS	61.5	129.6
J1236+393	12:36:51.52	+39:20:27.0	0.5	NVSS	77.4	136.0
J1238+212	12:38:17.3	+21:14:31	16	GB6	83.4	275.2
J1239+342	12:39:54.08	+34:15:29.4	0.5	NVSS	82.5	141.4
J1243+398	12:43:18.81	+39:51:17.1	0.5	NVSS	77.2	129.9
J1243+732	12:43:10.28	+73:16: 0.8	0.4	NVSS	43.9	123.8
J1248+154	12:48:38.8	+15:29:40	21	GB6	78.3	299.6
J1250+110	12:50:59.6	+11: 4: 9	18	GB6	73.9	302.5
J1256+350	12:56:11.25	+35: 2:18.8	0.4	NVSS	82.0	116.0
J1300+234	13: 0:17.9	+23:28:26	12	GB6	85.8	332.1
J1303+513	13: 3: 1.29	+51:19:47.7	0.5	NVSS	65.7	118.5
J1307+064	13: 7: 4.0	+ 6:27:54	13	GB6	69.0	313.8
J1309+524	13: 9: 7.87	+52:24:36.8	0.5	NVSS	64.5	116.6
J1318+044	13:18:29.2	+ 4:29:55	13	GB6	66.5	320.0
J1325+350	13:25:44.42	+35: 4:46.8	0.5	NVSS	79.2	82.4
J1326+445	13:26:36.95	+44:34:58.9	0.4	NVSS	71.2	103.2
J1350+320	13:50:44.3	+32: 5: 9	23	GB6	76.2	57.5
J1355+304	13:55:41.05	+30:24:11.4	0.4	NVSS	75.6	49.8
J1356+405	13:56:43.50	+40:35: 4.5	0.4	NVSS	71.0	82.1
J1403+637	14: 3:31.41	+63:42:53.0	0.4	NVSS	51.6	110.2
J1419+383	14:19:46.53	+38:21:48.7	0.5	NVSS	68.4	69.8
J1428+043	14:28:16.3	+ 4:19:41	16	GB6	57.5	352.6
J1434+420	14:34: 5.62	+42: 3:15.9	0.4	NVSS	64.3	75.1
J1437+381	14:37:33.36	+38: 7:44.9	0.5	NVSS	65.2	66.0
J1437+300	14:37:58.63	+30: 2: 6.8	0.5	NVSS	66.5	46.3

NAME	J2000 Position		±	Catalog	Galactic	
J1438+367	14:38:13.64	+36:44:50.6	0.5	NVSS	65.5	62.7
J1442+287	14:42:43.18	+28:46:38.7	0.5	NVSS	65.4	43.3
J1508+414	15: 8:46.57	+41:27:57.1	0.4	NVSS	58.5	68.9
J1520+745	15:20:43.8	+74:35:43	14	GB6	38.9	111.0
J1549+214	15:49:48.2	+21:25:44	11	GB6	49.2	34.9
J1554+028	15:54:48.6	+ 2:52:19	23	GB6	39.9	12.1
J1603+110	16: 3:42.7	+11: 5:46	11	GB6	42.2	23.0
J1606+133	16: 6:54.5	+13:19:33	13	GB6	42.4	26.2
J1608+104	16: 8:46.3	+10:29: 5	11	GB6	40.8	23.0
J1609+284	16: 9:40.20	+28:28:45.3	0.6	NVSS	46.5	46.8
J1612+204	16:12:59.7	+20:28:34	17	GB6	43.7	36.0
J1618+489	16:18:26.47	+48:59:39.3	0.5	NVSS	44.9	76.3
J1624+568	16:24:33.0	+56:52:38	9	GB6	42.3	86.6
J1631+108	16:31:19.1	+10:52: 3	13	GB6	36.0	26.6
J1630+741	16:30:26.52	+74: 9:33.1	0.4	NVSS	35.4	107.1
J1649+681	16:49:36.7	+68: 6:47	16	GB6	36.2	99.5
J1656+533	16:56:41.2	+53:21:51	9	GB6	38.4	81.0
J1657+481	16:57:46.91	+48: 8:32.6	0.4	NVSS	38.5	74.4
J1702+079	17: 2:28.7	+ 7:57: 4	12	GB6	27.8	27.5
J1700+685	17: 0: 9.24	+68:30: 6.5	0.4	NVSS	35.2	99.6
J1711+541	17:11:41.2	+54:11:50	9	GB6	36.1	81.9
J1716+689	17:16: 8.2	+68:56:10	7	GB6	33.7	99.7
J1716+686	17:16:13.91	+68:36:38.2	0.4	NVSS	33.8	99.3
J1717+743	17:17:38.68	+74:18:39.2	0.4	NVSS	32.3	105.9
J1722+610	17:22:40.02	+61: 5:59.9	0.4	NVSS	34.2	90.2
J1732+009	17:32:24.4	+ 0:59:43	16	GB6	18.0	24.5
J1740+438	17:40:48.0	+43:48:25	10	GB6	30.7	69.8
J1740+521	17:40:36.5	+52:11:47	9	GB6	31.7	79.6
J1745+670	17:45:54.38	+67: 3:49.0	0.4	NVSS	31.2	97.0
J1756+453	17:56:24.9	+45:23:28	13	GB6	28.2	72.2
J1759+287	17:59:15.2	+28:47:50	12	GB6	23.3	54.6

NAME	J2000 Position		±	Catalog	Galactic	
J1803+431	18: 3:14.1	+43: 6:20	21	GB6	26.6	70.0
J1808+451	18: 8: 2.1	+45:11:42	36	GB6	26.2	72.5
J1810+016	18:10: 2.2	+ 1:36:48	14	GB6	9.9	29.6
J1814+228	18:14: 1.5	+22:49: 3	24	GB6	18.1	49.9
J1849+670	18:49:15.87	+67: 5:40.8	0.4	NVSS	25.0	97.5
J1851+499	18:51:21.0	+49:59:14	14	GB6	20.5	79.6
J1852+489	18:52:29.4	+48:55:49	9	GB6	19.9	78.6
J1856+061	18:56:31.4	+ 6:10:13	12	GB6	1.7	39.0
J1924+286	19:24:14.7	+28:38: 0	12	GB6	6.1	62.0
J1956+635	19:56:25.8	+63:32:42	8	GB6	17.3	96.3
J2053+530	20:53:12.6	+53: 1:38	9	GB6	5.3	91.5
J2055+613	20:55:39.4	+61:22: 1	8	GB6	10.4	98.3
J2102+470	21: 2:17.7	+47: 2: 6	9	GB6	0.3	87.9
J2115+367	21:15:39.5	+36:45:56	11	GB6	-8.4	82.0
J2140+107	21:40: 5.3	+10:47:35	18	GB6	-30.1	65.6
J2145+187	21:45:14.35	+18:45:19.8	0.4	NVSS	-25.7	73.2
J2147+153	21:47:24.9	+15:20:52	11	GB6	-28.4	70.9
J2152+653	21:52:28.0	+65:20:35	9	GB6	8.7	105.7
J2201+248	22: 1:12.9	+24:51:17	15	GB6	-23.8	80.8
J2201+508	22: 1:43.4	+50:48:51	9	GB6	-3.5	97.6
J2202+292	22: 2: 5.3	+29:14:53	12	GB6	-20.6	84.1
J2208+615	22: 8:10.2	+61:32:55	11	GB6	4.6	104.7
J2240+515	22:40:19.1	+51:33: 8	10	GB6	-6.2	103.1
J2251+440	22:51:58.4	+44: 3:38	11	GB6	-13.7	101.3
J2258+496	22:58:26.0	+49:37:55	11	GB6	-9.2	104.8
J2327+096	23:27:33.7	+ 9:40: 9	11	GB6	-48.0	91.1
J2350+111	23:50: 1.8	+11: 6:28	12	GB6	-49.0	99.6
J0002+749	0: 2:33.4	+74:59:45	8	GB6	12.4	119.7

A.2 Short Term Variable Flux Related Information

NAME	F_{86}	F_{87}	F_6	F_{20}	α	$-logQ_{86}$	$-logQ_{87}$	V_σ
J0003+249	140 ± 8	59 ± 6	98 ± 9			1.2	3.8	8.0
J0005+544	184 ± 8	259 ± 10	231 ± 21			2.1	0.3	5.7
J0019+734	1377 ± 35	1712 ± 44	1583 ±141			2.7	4.2	6.0
J0036+185	52 ± 6	147 ± 9	126 ± 12	123 ± 4	0.0	0.3	3.6	9.0
J0039+411	36 ± 10	38 ± 12	34 ± 5			4.0	0.8	
J0042+544	58 ± 5	98 ± 6	82 ± 8			0.7	2.3	5.3
J0047+569	212 ± 9	302 ± 11	273 ± 24			3.0	2.1	6.3
J0048+684	49 ± 4	102 ± 5	81 ± 8			5.9	3.3	7.5
J0049+343	87 ± 6	141 ± 8	111 ± 10			5.9	1.6	5.4
J0120+265	54 ± 11	44 ± 17	41 ± 5			0.1	3.0	
J0121+118	1462 ± 68	967 ± 45	1126 ±100			4.7	2.2	6.0
J0128+490	594 ± 23	288 ± 12	408 ± 36			1.0	4.1	11.7
J0202+397	79 ± 6	131 ± 7	107 ± 10			2.5	0.9	5.5
J0228+673	1120 ± 33	1767 ± 52	1511 ±134			0.2	3.7	10.5
J0235+622	48 ± 4	87 ± 5	68 ± 7			0.4	4.0	5.6
J0249+511	130 ± 7	82 ± 6	104 ± 10			0.4	3.8	5.5
J0249+221	115 ± 7	173 ± 9	149 ± 14	421 ± 14	0.9	8.2	0.4	4.8
J0251+562	352 ± 13	252 ± 10	310 ± 27	196 ± 6	-0.4	4.2	2.0	6.1
J0259+516	119 ± 6	61 ± 5	96 ± 9	89 ± 3	-0.1	1.2	11.7	7.1
J0258+056	139 ± 10	241 ± 13	213 ± 19	150 ± 5	-0.3	3.7	0.4	6.2
J0302+535	220 ± 9	358 ± 14	280 ± 25			2.4	1.4	8.3
J0304+683	942 ± 27	1491 ± 43	1242 ±110			1.2	3.1	10.8
J0310+391	64 ± 6	109 ± 7	90 ± 9			0.3	2.9	5.2
J0310+382	356 ± 16	760 ± 32	628 ± 56			20.5	1.6	11.3
J0323+462	72 ± 5	133 ± 7	98 ± 9			3.2	0.2	6.8
J0325+349	35 ± 5	79 ± 6	55 ± 6			3.8	0.4	5.5
J0325+224	995 ± 45	711 ± 33	817 ± 72	532 ± 17	-0.4	3.3	7.9	5.1
J0326+287	192 ± 10	41 ± 5	116 ± 11			50.5	8.1	13.4
J0332+545	50 ± 5	4 ± 5	26 ± 4	151 ± 5	1.5	4.4	3.7	7.0
J0340+540	67 ± 5	110 ± 6	90 ± 8	126 ± 4	0.3	2.3	1.4	5.4
J0350+516	146 ± 7	204 ± 9	175 ± 16	123 ± 4	-0.3	0.6	2.0	5.1
J0357+418	71 ± 6	131 ± 7	118 ± 11	430 ± 14	1.1	5.7	1.7	6.6
J0411+087	56 ± 7	198 ± 11	137 ± 13	112 ± 4	-0.2	2.2	3.3	10.6
J0424+006	712 ± 34	1118 ± 53	879 ± 78	512 ± 17	-0.4	0.2	2.1	6.4
J0430+169	85 ± 7	143 ± 9	108 ± 10	42 ± 1	-0.8	13.5	1.7	5.2

NAME	F_{86}	F_{87}	F_6	F_{20}	α	$-logQ_{86}$	$-logQ_{87}$	V_σ
J0431+206	1971 ± 90	2811 ±128	2414 ±215	3822 ±120	0.4	0.1	10.5	5.4
J0440+146	175 ± 10	347 ± 17	264 ± 24	222 ± 7	-0.1	0.1	2.1	8.7
J0444+251	22 ± 19	37 ± 10	29 ± 4	56 ± 2	0.5	0.2	6.2	
J0445+072	505 ± 25	271 ± 14	371 ± 33	365 ± 12	0.0	5.3	0.7	8.2
J0449+635	399 ± 13	606 ± 20	519 ± 46	434 ± 14	-0.1	2.7	0.1	8.8
J0502+388	172 ± 9	289 ± 13	239 ± 21	60 ± 2	-1.1	2.5	8.9	7.5
J0502+346	70 ± 6	114 ± 7	106 ± 10	178 ± 6	0.4	3.3	6.8	4.8
J0518+331	203 ± 10	292 ± 14	256 ± 23	353 ± 12	0.3	3.4	0.6	5.3
J0530+550	183 ± 8	244 ± 10	220 ± 20	520 ± 16	0.7	2.3	1.5	4.9
J0532+562	89 ± 5	130 ± 6	113 ± 10	111 ± 4	0.0	7.4	2.5	5.0
J0534+089	37 ± 7	97 ± 8	74 ± 8	32 ± 1	-0.7	0.2	2.4	5.8
J0547+111	37 ± 10	39 ± 12	38 ± 6	80 ± 3	0.6	0.2	2.3	
J0607+712	175 ± 6	228 ± 8	203 ± 18			5.5	1.2	5.4
J0606+146	20 ± 9	45 ± 9	45 ± 6	111 ± 4	0.7	2.1	3.9	
J0611+723	44 ± 4	116 ± 6	87 ± 8	60 ± 2	-0.3	6.3	3.3	10.1
J0615+450	59 ± 5	18 ± 5	20 ± 4	62 ± 2	0.9	0.0	5.6	5.8
J0629+044	58 ± 14	114 ± 17	89 ± 9	92 ± 3	0.0	0.1	2.0	
J0658+193	32 ± 11	53 ± 11	34 ± 5	30 ± 1	-0.1	1.1	2.1	
J0714+146	520 ± 25	790 ± 37	679 ± 60	1999 ± 66	0.9	0.6	2.0	6.1
J0716+367	92 ± 6	150 ± 8	140 ± 13	304 ± 10	0.6	3.2	0.4	5.7
J0722+181	24 ± 6	39 ± 13	41 ± 5	44 ± 1	0.1	6.0	0.5	
J0731+673	292 ± 9	171 ± 7	226 ± 20	58 ± 2	-1.1	3.4	0.2	10.4
J0737+645	301 ± 10	229 ± 8	251 ± 22	418 ± 13	0.4	2.5	1.4	5.4
J0738+177	1530 ± 70	2166 ±100	1812 ±161	2289 ± 72	0.2	31.4	1.9	5.2
J0751+272	148 ± 8	214 ± 11	193 ± 17	605 ± 19	0.9	0.5	2.6	4.9
J0815+619	47 ± 4	81 ± 5	61 ± 6	108 ± 3	0.5	1.4	2.6	4.9
J0839+033	776 ± 37	510 ± 25	673 ± 60	669 ± 20	0.0	1.2	2.0	5.9
J0849+098	252 ± 13	157 ± 10	204 ± 18	295 ± 10	0.3	0.3	2.2	5.8
J0856+717	144 ± 6	208 ± 7	174 ± 16	64 ± 2	-0.8	2.8	4.6	7.0
J0903+636	17 ± 5	33 ± 5	25 ± 4	50 ± 2	0.6	6.2	7.1	
J0921+569	39 ± 5	72 ± 5	53 ± 6	37 ± 1	-0.3	0.4	5.5	4.8
J0927+572	98 ± 5	147 ± 7	123 ± 11	91 ± 3	-0.3	0.8	2.5	5.7
J0939+421	32 ± 10	32 ± 11	24 ± 4	90 ± 3	1.1	0.5	3.6	
J0943+435	20 ± 8	25 ± 9	34 ± 5	76 ± 3	0.7	0.6	3.5	
J0944+520	463 ± 18	345 ± 13	391 ± 35	624 ± 20	0.4	0.3	31.6	5.3
J0957+553	1704 ± 60	2270 ± 80	2015 ±179	3123 ± 98	0.4	9.0	5.4	5.6

NAME	F_{86}	F_{87}	F_6	F_{20}	α	$-logQ_{86}$	$-logQ_{87}$	V_σ
J0958+655	908 ± 28	1417 ± 43	1125 ±100	740 ± 23	-0.3	14.6	0.5	10.0
J1001+139	34 ± 11	59 ± 11	34 ± 5			4.0	0.3	
J1015+558	49 ± 5	89 ± 6	62 ± 6	138 ± 5	0.7	0.3	4.9	5.5
J1016+052	496 ± 24	745 ± 36	593 ± 53			2.6	0.1	5.8
J1019+633	205 ± 8	271 ± 10	237 ± 21	109 ± 3	-0.6	3.3	0.1	5.3
J1031+746	273 ± 8	202 ± 7	250 ± 22	199 ± 6	-0.2	4.1	0.7	6.8
J1030+515	106 ± 6	150 ± 7	128 ± 12	186 ± 6	0.3	3.1	0.5	4.7
J1037+571	180 ± 8	88 ± 5	126 ± 11	72 ± 2	-0.5	0.4	2.0	9.9
J1048+717	1460 ± 38	2410 ± 63	1900 ±169	751 ± 24	-0.8	0.2	4.6	12.8
J1103+720	31 ± 4	64 ± 5	44 ± 5	37 ± 1	-0.1	1.1	3.7	4.9
J1106+282	537 ± 24	274 ± 13	369 ± 33	225 ± 7	-0.4	6.0	1.5	9.6
J1106+172	123 ± 8	207 ± 11	152 ± 14			1.4	3.0	6.2
J1112+350	76 ± 6	122 ± 7	101 ± 9	135 ± 4	0.2	1.8	3.1	4.9
J1115+649	19 ± 10	57 ± 10	31 ± 4	101 ± 3	1.0	1.6	3.1	
J1120+126	113 ± 8	176 ± 10	151 ± 14			2.5	0.1	4.9
J1125+399	56 ± 5	99 ± 6	70 ± 7	182 ± 6	0.8	3.5	0.3	5.2
J1127+568	370 ± 14	597 ± 21	448 ± 40	484 ± 16	0.1	0.1	2.4	9.0
J1153+251	91 ± 7	38 ± 5	65 ± 7	72 ± 2	0.1	0.4	3.0	6.2
J1157+077	17 ± 8	67 ± 11	40 ± 6			2.6	2.3	
J1205+008	135 ± 10	218 ± 13	141 ± 15			4.5	0.0	5.0
J1206+527	114 ± 6	70 ± 5	85 ± 8			0.3	5.0	5.4
J1221+083	51 ± 7	120 ± 9	58 ± 8			0.9	3.4	6.2
J1222+042	1328 ± 63	934 ± 44	1351 ±120			15.9	8.7	5.1
J1229+553	68 ± 5	127 ± 6	106 ± 10	54 ± 2	-0.6	1.5	4.3	7.2
J1236+393	284 ± 13	193 ± 9	246 ± 22	352 ± 11	0.3	0.1	4.2	5.8
J1238+212	19 ± 5	60 ± 6	48 ± 6			3.1	1.4	5.0
J1239+342	38 ± 5	81 ± 6	59 ± 6	85 ± 3	0.3	3.8	1.1	5.4
J1243+398	36 ± 5	71 ± 6	58 ± 6	52 ± 2	-0.1	0.1	6.9	4.7
J1243+732	276 ± 8	345 ± 10	312 ± 27	299 ± 10	0.0	2.5	6.1	5.4
J1248+154	15 ± 8	31 ± 13	38 ± 5			1.5	3.3	
J1250+110	88 ± 7	32 ± 6	73 ± 9			0.1	3.2	5.8
J1256+350	61 ± 6	117 ± 7	92 ± 9	300 ± 10	1.0	1.1	2.0	6.2
J1300+234	67 ± 21	107 ±100	103 ± 10			0.5	4.6	
J1303+513	77 ± 5	125 ± 7	90 ± 8	169 ± 5	0.5	7.3	0.5	5.6
J1307+064	151 ± 10	263 ± 14	146 ± 14			11.5	0.9	6.5
J1309+524	17 ± 8	26 ± 10	27 ± 4	62 ± 2	0.7	2.0	1.5	

NAME	F_{86}	F_{87}	F_6	F_{20}	α	$-logQ_{86}$	$-logQ_{87}$	V_σ
J1318+044	238 ± 13	122 ± 9	222 ± 21			0.0	3.8	7.2
J1325+350	48 ± 11	29 ± 9	29 ± 4	42 ± 1	0.3	0.5	5.1	
J1326+445	105 ± 6	162 ± 8	140 ± 13	182 ± 6	0.2	0.6	3.5	5.7
J1350+320	2 ± 5	44 ± 5	29 ± 4			0.1	5.9	5.7
J1355+304	84 ± 6	135 ± 8	103 ± 10	143 ± 5	0.3	14.5	0.7	5.1
J1356+405	28 ± 10	54 ± 12	24 ± 4	74 ± 2	0.9	0.2	4.2	
J1403+637	373 ± 12	491 ± 16	433 ± 38	916 ± 28	0.6	0.4	2.4	5.9
J1419+383	381 ± 17	871 ± 37	651 ± 58	621 ± 20	0.0	2.4	1.9	12.2
J1428+043	115 ± 9	190 ± 11	115 ± 12			1.3	2.3	5.2
J1434+420	177 ± 9	353 ± 15	280 ± 25	313 ± 10	0.1	1.6	2.3	10.2
J1437+381	55 ± 5	100 ± 6	83 ± 8	218 ± 7	0.8	2.1	0.4	5.4
J1437+300	73 ± 6	132 ± 8	99 ± 9	60 ± 2	-0.4	2.4	0.2	6.0
J1438+367	62 ± 6	102 ± 6	75 ± 7	58 ± 2	-0.2	1.4	2.5	4.7
J1442+287	3 ± 8	30 ± 10	32 ± 5	69 ± 2	0.6	0.1	2.3	
J1508+414	78 ± 6	130 ± 7	117 ± 11	415 ± 14	1.1	1.9	2.1	5.6
J1520+745	56 ± 11	69 ± 13	47 ± 5			5.2	0.6	
J1549+214	546 ± 25	765 ± 35	636 ± 56			0.6	4.2	5.1
J1554+028	37 ± 10	48 ± 13	47 ± 8			4.9	0.8	
J1603+110	363 ± 18	831 ± 39	626 ± 55			0.6	16.8	10.9
J1606+133	95 ± 7	161 ± 9	137 ± 13			0.0	2.4	5.5
J1608+104	1196 ± 56	1686 ± 79	1412 ±125			0.1	17.4	5.1
J1609+284	31 ± 11	37 ± 12	27 ± 5	37 ± 1	0.3	0.5	3.8	
J1612+204	36 ± 17	31 ± 9	46 ± 6			0.4	2.0	
J1618+489	19 ± 12	44 ± 10	21 ± 4	66 ± 2	0.9	1.8	2.8	
J1624+568	159 ± 7	213 ± 9	183 ± 16			2.0	0.1	4.8
J1631+108	126 ± 9	209 ± 11	145 ± 13			0.1	2.1	5.8
J1630+741	86 ± 5	139 ± 6	116 ± 10	300 ± 9	0.8	5.7	2.6	6.8
J1649+681	16 ± 4	50 ± 5	39 ± 5			3.1	1.4	5.3
J1656+533	105 ± 6	174 ± 8	145 ± 13			2.7	2.0	7.1
J1657+481	604 ± 24	847 ± 33	738 ± 65	1064 ± 35	0.3	0.3	2.8	6.0
J1702+079	254 ± 14	117 ± 9	172 ± 16			1.2	2.3	8.5
J1700+685	341 ± 11	435 ± 13	380 ± 34	351 ± 12	-0.1	4.7	1.5	5.6
J1711+541	203 ± 9	123 ± 6	172 ± 15			3.0	0.1	7.5
J1716+689	251 ± 8	314 ± 10	286 ± 25			2.6	2.1	4.9
J1716+686	732 ± 21	988 ± 28	838 ± 74	508 ± 17	-0.4	3.1	4.2	7.2
J1717+743	103 ± 5	139 ± 6	125 ± 11	432 ± 14	1.0	0.7	2.3	4.7

NAME	F_{86}	F_{87}	F_{6}	F_{20}	α	$-logQ_{86}$	$-logQ_{87}$	V_{σ}
J1722+610	151 ± 6	321 ± 11	245 ± 22	157 ± 5	-0.4	4.6	0.9	12.9
J1732+009	155 ± 11	78 ± 9	98 ± 10			1.4	2.2	5.5
J1740+438	146 ± 8	234 ± 10	196 ± 17			2.0	0.0	6.8
J1740+521	2316 ± 85	1133 ± 42	1699 ±151			4.0	1.2	12.4
J1745+670	248 ± 8	321 ± 10	288 ± 25	713 ± 23	0.8	2.0	0.7	5.5
J1756+453	88 ± 6	34 ± 5	59 ± 6			2.1	1.8	7.1
J1759+287	72 ± 6	169 ± 9	134 ± 12			2.7	0.6	8.9
J1803+431	19 ± 12	38 ± 9	30 ± 4			0.1	2.7	
J1808+451	20 ± 10	33 ± 15	24 ± 5			0.1	2.1	
J1810+016	175 ± 11	84 ± 9	118 ± 12			0.2	3.0	6.3
J1814+228	18 ± 7	40 ± 7	29 ± 5			7.0	6.0	
J1849+670	608 ± 18	992 ± 29	845 ± 75	529 ± 17	-0.4	2.8	4.0	11.1
J1851+499	5 ± 5	97 ± 6	53 ± 6			0.3	2.2	12.3
J1852+489	219 ± 10	351 ± 14	311 ± 28			3.6	4.9	7.7
J1856+061	267 ± 14	149 ± 10	193 ± 18			0.1	4.5	6.8
J1924+286	140 ± 8	47 ± 5	92 ± 9			2.8	4.5	9.5
J1956+635	364 ± 12	143 ± 6	136 ± 12			22.2	1.8	16.1
J2053+530	170 ± 8	106 ± 6	139 ± 13			3.0	0.8	6.6
J2055+613	307 ± 11	414 ± 14	385 ± 34			3.7	4.3	5.9
J2102+470	229 ± 10	137 ± 7	170 ± 15			0.6	2.7	7.5
J2115+367	71 ± 6	136 ± 8	110 ± 10			1.6	13.4	6.8
J2140+107	32 ± 6	92 ± 8	57 ± 7			2.6	0.3	6.1
J2145+187	45 ± 6	88 ± 7	71 ± 7	79 ± 2	0.1	2.6	2.2	4.8
J2147+153	763 ± 36	1080 ± 50	927 ± 82			2.1	0.6	5.1
J2152+653	76 ± 5	111 ± 6	92 ± 9			8.5	1.2	4.8
J2201+248	31 ± 5	72 ± 6	62 ± 7			2.1	0.4	5.0
J2201+508	649 ± 25	916 ± 35	820 ± 73			0.3	4.0	6.3
J2202+292	71 ± 6	116 ± 7	97 ± 9			3.0	4.6	4.8
J2208+615	47 ± 4	92 ± 5	67 ± 7			3.5	5.7	6.4
J2240+515	141 ± 7	193 ± 9	169 ± 15			0.3	2.7	4.8
J2251+440	79 ± 6	127 ± 7	104 ± 10			5.0	0.6	5.3
J2258+496	63 ± 5	103 ± 6	87 ± 8			5.6	0.5	5.0
J2327+096	508 ± 25	738 ± 35	643 ± 57			4.8	0.8	5.4
J2350+111	291 ± 15	192 ± 11	247 ± 22			2.1	0.1	5.4
J0002+749	77 ± 5	113 ± 6	96 ± 9			2.1	1.5	4.8

A.3 Short Term Variable *SIMBAD* Matches

NAME	Class	Position (J2000)	Distance
J0019+734	Radio	0:19:45.70 +73:27:30.2	3.70
J0121+118	QSO	1:21:41.52 +11:49:50.6	14.90
J0202+397	Radio	2: 2: 1.63 +39:43:20.6	4.80
J0228+673	QSO	2:28:50.05 +67:21: 3.0	6.30
J0310+382	Radio	3:10:49.88 +38:14:53.9	4.60
J0326+287	RSCVn	3:26:35.09 +28:42:59.3	8.70
J0332+545	Pulsar	3:32:59.31 +54:34:44.0	0.50
J0431+206	RadioG	4:31: 3.69 +20:37:34.2	0.90
J0449+635	QSO	4:49:23.25 +63:32: 9.5	1.00
J0502+388	Radio	5: 2:32.45 +38:49:52.5	2.40
J0714+146	RadioG	7:14: 4.64 +14:36:22.6	1.90
J0738+177	BLLac	7:38: 7.39 +17:42:19.0	0.80
J0957+553	QSO	9:57:38.67 +55:22:58.9	4.80
J0958+655	BLLac	9:58:47.24 +65:33:54.8	0.70
J1031+746	Radio	10:31:22.16 +74:41:57.9	0.70
J1037+571	BLLac	10:37:44.50 +57:11:54.0	3.10
J1048+717	AGN	10:48:27.58 +71:43:35.6	0.50
J1112+350	Radio	11:12:33.25 +35: 3:38.6	1.30
J1127+568	QSO	11:27:40.16 +56:50:14.8	0.70
J1236+393	Radio	12:36:51.36 +39:20:28.1	2.20
J1243+732	Galaxy	12:43:11.16 +73:15:59.2	4.10

NAME	Class	Position (J2000)	Distance
J1256+350	Radio	12:56:11.19 +35: 2:17.6	1.40
J1355+304	QSO	13:55:40.81 +30:24: 8.6	4.20
J1419+383	Radio	14:19:46.47 +38:21:48.1	0.90
J1434+420	Radio	14:34: 5.70 +42: 3:16.0	0.90
J1437+381	Radio	14:37:33.36 +38: 7:44.8	0.10
J1520+745	Radio	15:20:42.85 +74:35:42.2	4.00
J1549+214	RadioG	15:49:48.94 +21:25:38.8	11.40
J1608+104	QSO	16: 8:46.20 +10:29: 7.8	3.70
J1630+741	Radio	16:30:25.83 +74: 9:33.5	2.80
J1657+481	Galaxy	16:57:46.81 +48: 8:33.1	1.10
J1700+685	Radio	17: 0: 9.02 +68:30: 5.7	1.40
J1716+689	Radio	17:16: 9.14 +68:56:14.1	6.30
J1716+686	QSO	17:16:13.81 +68:36:38.3	0.60
J1717+743	Radio	17:17:38.37 +74:18:41.7	2.80
J1740+521	QSO	17:40:36.98 +52:11:43.4	5.70
J1849+670	QSO	18:49:15.94 +67: 5:42.8	2.00
J1852+489	QSO	18:52:28.39 +48:55:47.5	9.80
J2102+470	Radio	21: 2:17.01 +47: 2:16.4	12.40
J2147+153	RadioG	21:47:25.07 +15:20:32.1	20.30
J2201+508	Radio	22: 1:42.62 +50:49: 1.4	12.80
J2240+515	Star	22:40:17.65 +51:32:51.2	21.50

A.4 Short Term Variable *NED* Matches

NAME	Radio	X-ray	QSO	Galaxy	Other
J0005+544	•				
J0019+734	2		•		
J0042+544	•				
J0047+569	•				
J0049+343	•				
J0120+265	•				
J0121+118	4			•	
J0128+490	•			•	
J0202+397	•				VisS
J0228+673	4				Blue
J0249+221	•				
J0258+056	•				
J0302+535	•				
J0304+683	2				
J0310+391	•				
J0310+382	•		•		
J0323+462	•				
J0325+224	•				
J0332+545	•				
J0340+540	2				
J0357+418	3				
J0411+087	2				
J0424+006	4	•	•		
J0431+206	5			•	
J0440+146	•				
J0445+072	2				
J0449+635	2		•		
J0502+388	•				

NAME	Radio	X-ray	QSO	Galaxy	Other
J0502+346	•				
J0518+331	•				
J0530+550	•				
J0607+712	2				
J0606+146	2				
J0714+146	4			•	
J0716+367	2				
J0737+645	•				
J0738+177	8	2	•		AbLS GammaS IrS
J0751+272	2				
J0839+033	3		•		
J0849+098	6				
J0856+717	•				
J0903+636	•				
J0939+421	•				
J0943+435	•				
J0944+520	2		•		
J0957+553	7	•	•		
J0958+655	3	•	•		GammaS
J1015+558	•				
J1016+052	4				VisS(2)
J1031+746	2	•			
J1030+515	•				
J1048+717	2		•		
J1106+282	•				
J1106+172	•				
J1112+350	•				
J1120+126	•				
J1125+399	2				

NAME	Radio	X-ray	QSO	Galaxy	Other
J1127+568	3		•		
J1205+008	3		•		
J1206+527	•			•	SN IrS
J1221+083	•				
J1222+042	6	2	•		
J1236+393	3				
J1243+398	•				
J1243+732	2			•	
J1256+350	2				
J1300+234	3				
J1303+513	•			•	
J1307+064	•				
J1318+044	2				
J1355+304	•		•		
J1356+405	2				
J1403+637	3				
J1419+383	2		•		
J1434+420	2		•		
J1437+381	2		•		EmLS
J1508+414	2				
J1520+745	2				
J1549+214				•	GLens
J1603+110	•				
J1608+104	7	•	•		
J1618+489	•				
J1624+568	2				
J1630+741	3				
J1656+533	•				
J1657+481	3				

NAME	Radio	X-ray	QSO	Galaxy	Other
J1702+079	•				
J1700+685	3				
J1711+541	•				
J1716+689	5				
J1716+686	4	•	•		
J1717+743	4				
J1722+610	•				
J1732+009	5				
J1740+521	5	•	•		GammaS
J1745+670	3				
J1803+431	•				
J1810+016	•				
J1849+670					AbLS
J1852+489	2		•		
J1924+286	•				
J1956+635	•				
J2055+613	•				
J2102+470	•				VisS
J2115+367	•				
J2145+187	•				
J2147+153	7			•	
J2152+653	2				
J2201+248	•				
J2201+508	•				
J2202+292	•				
J2240+515	•				
J2251+440	3				
J2327+096	5	•	•		
J2350+111	•				

A.5 Short Term Variable *APS* Counterparts

NAME	Class	Position (J2000)	Distance	Magnitude	Colour
J0258+056	Star	2:58:50.54 + 5:41:08.12	0.92	20.26	-0.38
J0430+169	Star	4:30:22.28 +16:55:04.30	1.08	20.62	2.48
J0445+072	Galaxy	4:45:01.45 + 7:15:53.64	0.74	20.84	0.94
J0449+635	Star	4:49:23.16 +63:32:10.28	1.93	20.36	1.42
J0716+367	Galaxy	7:16:37.10 +36:42:19.22	1.25	16.53	1.94
J0737+645	Star	7:37:58.96 +64:30:43.16	0.18	20.84	4.32
J0856+717	Star	8:56:54.83 +71:46:23.52	1.77	19.65	0.52
J0958+655	Star	9:58:47.27 +65:33:54.43	0.58	16.82	0.78
J1031+746	Galaxy	10:31:22.78 +74:41:56.26	2.76	17.53	1.50
J1048+717	Star	10:48:27.58 +71:43:35.40	0.31	19.08	0.66
J1106+282	Star	11:06:07.26 +28:12:46.33	1.09	19.42	0.36
J1153+251	Galaxy	11:53:18.12 +25:09:04.39	0.53	22.41	1.86
J1309+524	Star	13.09:07.98 +52:24:37.30	1.11	18.38	0.52
J1355+304	Star	13:55:41.11 +30:24:11.23	0.82	18.73	0.50
J1609+284	Star	16:09:40.27 +28:28:47.24	2.12	19.77	0.12
J1722+610	Star	17:22:40.01 +61:05:59.24	0.69	19.41	0.02